“Design Strategies for Optimized Mechanical Performance of Bainitic Steels”

Von der Fakultät für Georesourcen und Materialtechnik der

Rheinisch-Westfälischen Technischen Hochschule Aachen

zur Erlangung des akademischen Grades eines

Doktors der Ingenieurwissenschaften

genehmigte Dissertation

vorgelegt von

Oğuz Gülbay, M. Sc.

Berichter: Univ.-Prof. Dr.-Ing. habil. Ulrich Krupp

Prof. Adam Grajcar, DS.c Ph.D Eng.

Tag der mündlichen Prüfung: 10.02.2026

Acknowledgements

First of all, I would like to thank the Bundesministerium für Bildung und Forschung (BMBF, German Federal Ministry of Education and Research) and MaterialDigital platform for enabling this scientific work as part of the project *iBain - Intelligent-datengeführtes Prozessdesign für ermüdungsresistente Stahlbauteile am Beispiel bainitischer Mikrostruktur* (Grant numbers: 13XP5118A, 13XP5118B and 13XP5118C) as well as all the project partners.

My sincere gratitude to Prof. Dr.-Ing. Ulrich Krupp for supervising this dissertation, for the freedom given within the research project, and for the opportunity to work with the state-of-the-art equipment at the Steel Institute, RWTH Aachen University. Additionally, I would like to thank Prof. Dr. Adam Grajcar for his willingness to act as an examiner of this work.

I deeply thank my dear friends and former colleagues, Ahmet Turnalı and Dilay Kibaroğlu, with whom I shared this journey from the very beginning. Their unwavering support, encouragement, and the countless professional and personal moments we shared have made this experience truly meaningful and unforgettable. I would also like to thank Deniz Güler and Ecem Gözde Arıkan for their friendship and support beyond the academic environment.

Special thanks go to my current and former colleagues at the Steel Institute, whose collaboration made this work possible. In particular, I would like to thank my group leader, Alexander Gramlich, for his motivating support, supervision, and the scientifically valuable and constructive discussions. I would also like to thank my office mates, Marion Kreins and Lars Bähren, for creating such a positive and lively atmosphere, where working together became both productive and genuinely enjoyable. Additionally, I would like to thank Can Akkus for sharing countless great moments at work and beyond. Further, I would like to thank my dear colleagues, Marc Ackermann, Robin Emmrich, Charline Blankart, Felix Oppermann, Jing Wang, Marco Hippe, Nima Babaei, Buğra Köksal, Sindokht Shayan, Aleksei Seregin, and Ekatarina Evsiutkina. The successful completion of numerous experimental investigations would not have been possible without the support of our skilled technicians, in particular Jürgen Dartenne, Michael Schillheim, Jens Ludwig, and Robert Gier.

Finally, I would like to express my heartfelt thanks to my parents, Murat Gülbay and Esma Çevik, who made my studies possible and whose support and encouragement I could always rely on; to my brother, Onur Gülbay, for his motivating and ‘whipping’ pep talks, his boundless support, and his constant belief in me; and to Sarah Roth for her patience, understanding, and constant support.

Abstract

Developing steel products with enhanced properties is crucial for extending the lifespan and reliability of engineering components. Beyond engineering performance, this additionally contributes to environmental sustainability by improving the circularity of the steel industry. To fulfill these requirements, bainitic steels have attracted considerable research attention due to their promising mechanical properties achieved with cost-effective alloying strategies. Modifications in chemical composition and processing parameters result in significant changes to the resulting bainitic microstructure, which in turn impacts the mechanical performance. Although quasi-static tensile properties are commonly used to evaluate the bainitic steels, they do not fully reflect the mechanical performance under service-relevant conditions. Therefore, it is essential to assess the mechanical behavior under different loading conditions. However, due to the complex and multiphase nature of the bainitic microstructure, which may include carbides, retained austenite (γ_R), and potential martensitic regions as secondary phases, establishing clear correlations remains a major challenge.

To address these challenges, the bainitic phase transformation and microstructure evolution were investigated in a Fe–0.2C–2.5Mn base-alloy as a function of heat treatment parameters and Si and Al alloying, which are key alloying elements in suppressing carbide formation to generate carbide-free bainite (CFB). The overall phase transformation behavior was characterized through continuous-cooling-transformation (CCT) and time-temperature-transformation (TTT) diagrams, determined using dilatometry. The effect of isothermal transformation temperature on the quasi-static tensile properties and high-cycle fatigue (HCF) performance of CFB and carbide-bearing bainite (CBB) was comparatively evaluated. Furthermore, the mechanical response under different loading scenarios was investigated. The complex role of microstructural constituents, particularly γ_R and martensite-austenite (MA) islands, in governing fatigue crack resistance, impact toughness, and fracture mechanisms was analyzed. Throughout the study, the relationship between the resulting microstructures and mechanical performance was established using a wide range of characterization methods, including scanning electron microscopy (SEM), electron backscatter diffraction (EBSD), and Synchrotron X-Ray diffraction (SYXRD).

The results show that Al substantially increases the martensite start temperature (M_s) and strongly promotes the ferritic constituents compared to Si. With Al alloying, Widmanstätten ferrite forms during continuous cooling induced by high cooling rates and large prior austenite grain (PAG) size. Si addition slows bainite transformation by stabilizing austenite through

carbon enrichment and solid solution strengthening. While Al exhibits similar effects, it shortens the incubation time during isothermal heat treatment due to increased driving force for bainite transformation, overcompensating for the retardation effects. Al alloying results in achieving a finer CFB microstructure with pronounced film-like γ_R with enhanced carbon enrichment, leading to improved γ_R stability and suppressed MA island formation.

CFB demonstrates superior quasi-static tensile properties compared to CBB, mainly due to the gradual transformation of γ_R to martensite under uniaxial tension. Lowering the transformation temperature leads to a finer distribution of carbides in CBB and a more refined CFB microstructure, characterized by pronounced film-like γ_R morphology and reduced MA island fraction. These microstructural modifications obtained at lower temperatures contribute to improved mechanical performance in both bainite groups. On the other hand, the fracture behavior of CFB is significantly affected by the presence of MA islands and unstable γ_R at PAG boundaries, particularly under localized deformation, as observed in Charpy impact and bending fatigue tests. While CBB exhibits substantially higher impact toughness with clear ductile characteristics in the fracture surface, CFB shows a tendency for brittle failure. This is primarily due to the abrupt transformation of unstable γ_R and the brittle nature of MA islands, which either lead to intergranular fracture through the formation of a brittle network along the PAG boundaries or to cleavage fracture initiated by rapid debonding at high deformation rates. Moreover, despite a significantly higher fatigue limit of CFB, which is consistent with its enhanced quasi-static tensile properties, it shows a higher fatigue crack propagation rate and lower threshold of stress intensity range (ΔK_{th}) than CBB. While PAGBs in CBB successfully deflect the fatigue cracks, MA islands, and unstable austenitic constituents in CFB weaken these boundaries, resulting in intergranular fractures through the brittle network or cracks that cut PAGBs without deflection. However, ductile fracture behavior is observed when the crack goes through a PAG instead of cleavage fracture, highlighting the influence of a lower deformation rate compared to Charpy impact tests.

Zusammenfassung

Die Entwicklung von Stählen mit verbesserten Eigenschaften ist entscheidend für die Verlängerung der Lebensdauer und Zuverlässigkeit von Bauteilen im Maschinenbau. Neben der technischen Leistungsfähigkeit trägt dies auch zur ökologischen Nachhaltigkeit bei, indem die Zirkularität der Stahlindustrie verbessert wird. Um diese Anforderungen zu erfüllen, haben bainitische Stähle aufgrund ihrer vielversprechenden mechanischen Eigenschaften bei gleichzeitig kosteneffizienten Legierungsstrategien große Forschungsaufmerksamkeit erlangt. Änderungen in der chemischen Zusammensetzung und den Prozessparametern führen zu signifikanten Veränderungen der bainitischen Mikrostruktur, die wiederum die mechanischen Eigenschaften beeinflussen. Obwohl die quasi-statischen Zugversuchseigenschaften häufig zur Bewertung bainitischer Stähle herangezogen werden, spiegeln sie das mechanische Verhalten unter realitätsnahen Einsatzbedingungen nicht vollständig wider. Daher ist es wesentlich, das Werkstoffverhalten unter unterschiedlichen Belastungsbedingungen zu untersuchen. Aufgrund der komplexen und mehrphasigen Natur der bainitischen Mikrostruktur, die Karbide, Restaustenit (γ_R) und potenziell martensitische Bereiche als Sekundärphasen enthalten kann, bleibt die Herstellung eindeutiger Korrelationen jedoch eine große Herausforderung.

Zur Bewältigung dieser Herausforderung wurden die bainitische Phasenumwandlung und die Mikrostrukturentwicklung in einer Fe–0,2C–2,5Mn-Basislegierung in Abhängigkeit von Wärmebehandlungsparametern sowie der Si- und Al-Legierung, welche entscheidende Elemente zur Unterdrückung der Karbidbildung und zur Erzeugung von karbidfreiem Bainit (CFB) darstellen, untersucht. Das gesamte Phasenumwandlungsverhalten wurde anhand von kontinuierlichen sowie isothermen Zeit-Temperatur-Umwandlungsschaubildern (ZTU) Dilatometrie charakterisiert. Der Einfluss der isothermen Umwandlungstemperatur auf die quasi-statischen Zugversuchseigenschaften und die Hochzyklusermüdungsfestigkeit (HCF) von CFB und karbidführendem Bainit (CBB) wurde vergleichend bewertet. Die komplexe Rolle der mikrostrukturellen Bestandteile, insbesondere von γ_R und Martensit-Austenit-(MA)-Inseln, bei der Steuerung der Ermüdungsrissbeständigkeit, der Kerbschlagzähigkeit und der Bruchmechanismen wurde analysiert. Der Zusammenhang zwischen den resultierenden Mikrostrukturen und der mechanischen Leistungsfähigkeit wurde mittels einer breiten Palette von Charakterisierungsmethoden, einschließlich Rasterelektronenmikroskopie (REM), Elektronenrückstreubeugung (EBSD) und Synchrotron-Röntgendiffraktion (SYXRD), hergestellt.

Die Ergebnisse zeigen, dass Al die Martensitstarttemperatur (M_s) deutlich erhöht und im Vergleich zu Si die Bildung ferritischer Bestandteile stark begünstigt. Bei Al-Legierung bildet sich während des kontinuierlichen Abkühlens bei hohen Abkühlraten und großer ehemaliger Austenitkorngröße (eng.: prior austenite grain size PAG) Widmanstätten-Ferrit. Si verlangsamt die Bainitumwandlung durch Stabilisierung des Austenits infolge von Kohlenstoffanreicherung und Mischkristallhärtung. Al zeigt zwar ähnliche Effekte, verkürzt jedoch die Inkubationszeit während der isothermen Wärmebehandlung aufgrund der erhöhten Triebkraft für die Bainitumwandlung und kompensiert so die retardierenden Effekte. Durch Al wird eine feinere CFB-Mikrostruktur mit ausgeprägtem, lamellaren γ_R und erhöhter Kohlenstoffanreicherung erzielt, was zu verbesserter γ_R-Stabilität und unterdrückter MA-Insel-Bildung führt.

CFB weist im Vergleich zu CBB überlegene quasi-statische Zugversuchseigenschaften auf, was hauptsächlich auf die graduelle Umwandlung von γ_R zu Martensit unter uniaxialer Zugbelastung zurückzuführen ist. Eine Absenkung der Umwandlungstemperatur führt zu einer feineren Karbidverteilung in CBB und einer stärker verfeinerten CFB-Mikrostruktur, die durch eine ausgeprägte lamellare γ_R-Morphologie und einen reduzierten MA-Insel-Anteil gekennzeichnet ist. Diese mikrostrukturellen Veränderungen bei niedrigeren Temperaturen tragen zu verbesserten mechanischen Eigenschaften in beiden Bainitgruppen bei. Das Bruchverhalten von CFB wird hingegen stark durch die Anwesenheit von MA-Inseln und instabilem γ_R an PAG-Grenzen beeinflusst, insbesondere unter lokalisierter Deformation, wie in Kerbschlag- und Biegeversuchen beobachtet. Während CBB eine deutlich höhere Kerbschlagzähigkeit mit klaren duktilen Merkmalen an der Bruchfläche zeigt, neigt CFB zu sprödem Versagen. Dies ist in erster Linie auf die abrupte Umwandlung von instabilem γ_R und die spröde Natur der MA-Inseln zurückzuführen, die entweder zu intergranularem Bruch durch die Bildung eines spröden Netzwerks entlang der PAG-Grenzen oder zu Spaltbruch führen, ausgelöst durch schnelles Ablösen bei hohen Deformationsraten. Trotz einer signifikant höheren Ermüdungsgrenze von CFB, die mit seinen verbesserten quasi-statischen Zugversuchseigenschaften übereinstimmt, zeigt es eine höhere Rissfortschrittsgeschwindigkeit und eine niedrigere Schwelle der Spannungsintensität (ΔK_{th}) als CBB. Während PAG-Grenzen in CBB die Ermüdungsrisse erfolgreich ablenken, schwächen MA-Inseln und instabile austenitische Bestandteile in CFB diese Grenzen, was zu intergranularen Brüchen durch das spröde Netzwerk oder zu Rissen führt, die PAG-Grenzen ohne Ablenkung durchschneiden. Duktile Bruchcharakteristik wird hingegen beobachtet, wenn der Riss durch ein PAG läuft, anstatt einen Spaltbruch zu initiieren, was den Einfluss einer niedrigeren Deformationsrate im Vergleich zu Kerbschlagversuchen verdeutlicht.

Özet

Yüksek mekanik özelliklere sahip çelik parçaların geliştirilmesi mühendislikte kullanılan bileşenlerin ömrünü ve güvenirliğini artırmak açısından önem arz etmektedir. Mühendislik performansının ötesinde bu durum, çelik endüstrisinin döngüselliğini iyileştirerek çevresel sürdürülebilirliğe de katkıda bulunmaktadır. Bu gereklilikleri karşılamak amacıyla, düşük maliyetli alaşım stratejileriyle ve umut verici mekanik özelliklerinden dolayı beynitik çelikler önemli derecede araştırma ilgisi görmektedir. Kimyasal bileşim ve proses parametrelerindeki değişiklikler, beynitik mikroyapıda önemli farklılıklara yol açmakta ve bu da mekanik performansı etkilemektedir. Beynitik çeliklerin değerlendirilmesinde çoğunlukla yarı-statik çekme özellikleri kullanılmaktadır. Ancak, bu yöntem hizmet koşullarına uygun mekanik davranışı tam olarak yansıtmamaktadır. Bu nedenle, farklı yükleme koşullarında malzeme davranışının incelenmesi gereklidir. Bununla birlikte, karbürler, kalıntı östenit (γ_R) ve ikincil faz olarak potansiyel martenzitik bölgeleri içerebilen beynitik mikroyapının karmaşık ve çok fazlı doğası nedeniyle net ilişki kurulması büyük bir zorluk teşkil etmektedir.

Bu problemin çözümü amacıyla Fe–0,2C–2,5Mn bazlı bir alaşımda beynitik faz dönüşümü ve mikroyapı evrimi araştırılmıştır. Karbür oluşumunun baskılanması ve karbürsüz beynit (CFB) elde etmek açısından kritik öneme sahip Si ve Al ilaveleri ile ısıl işlem parametrelerine etkisi incelenmiştir. Genel faz dönüşüm davranışı, dilatometri kullanılarak elde edilen sürekli soğuma dönüşüm (CCT) ve zaman-sıcaklık dönüşüm (TTT) diyagramları aracılığıyla karakterize edilmiştir. İzotermal dönüşüm sıcaklığının, CFB ve karbür içeren beynit (CBB) için yarı-statik çekme özellikleri ve yüksek çevrimli yorulma (HCF) performansı üzerindeki etkisi karşılaştırmalı olarak değerlendirilmiştir. Ayrıca, farklı yükleme senaryoları altındaki mekanik tepki incelenmiştir. Mikroyapısal bileşenlerin, özellikle γ_R ve martenzit-östenit (MA) adacıklarının yorulma çatlağı direncini, darbe tokluğunu ve kırılma mekanizmalarını yönlendirmedeki karmaşık rolleri analiz edilmiştir. Elde edilen mikroyapılar ile mekanik performans arasındaki ilişki, taramalı elektron mikroskobu (SEM), elektron geri saçılma difraksiyonu (EBSD) ve Sinkrotron X-ışını difraksiyonu (SYXRD) gibi geniş bir karakterizasyon yöntemleri yelpazesi ile ortaya konmuştur.

Sonuçlar, Al ilavesinin martenzit başlangıç sıcaklığını (M_s) önemli ölçüde artırdığını ve Si ilavesine kıyasla ferritik bileşenlerin oluşumunu güçlü biçimde teşvik ettiğini göstermektedir. Al alaşımlaması , yüksek soğuma hızları ve önceki östenit tane (PAG) boyutunun kabalaşmasının da etkisiyle sürekli soğuma sırasında Widmanstätten ferriti oluşmaktadır. Si ilavesi, karbon zenginleşmesi ve katı çözelti sertleşmesi yoluyla östeniti stabilize ederek beynit

dönüşümünü yavaşlatmaktadır. Al ise benzer etkiler göstermekte, ancak dönüşüm için gerekli itici kuvveti artırması nedeniyle izotermal ısıl işlem sırasında kuluçka süresini kısaltmakta ve böylece geciktirici etkileri dengelemektedir. Al alaşımlaması sonucunda film benzeri γ_R içeren daha ince ve karbonca zenginleşmiş bir CFB mikroyapı elde edilmektedir. Bu sayede, γ_R kararlılığı artmakta ve MA adacığı oluşumu baskılanmaktadır.

CFB, CBB'ye kıyasla üstün yarı-statik çekme özellikleri göstermektedir. Bunun nedeni temelde, γ_R'in tek eksenli çekme altında kademeli olarak martenzite dönüşmesinden kaynaklanmaktadır. Dönüşüm sıcaklığının düşürülmesi, CBB'de daha ince karbür dağılımına ve CFB'de film-vari γ_R morfolojisi ve düşük miktarda MA adacığı ile karakterize edilen daha ince bir mikroyapıya yol açmaktadır. Bu mikroyapısal değişiklikler, her iki beynit grubunda da geliştirilmiş mekanik performansa katkı sağlamaktadır. Öte yandan, CFB'nin kırılma davranışı, özellikle lokalize deformasyon altında (Charpy darbe ve yorulma eğilme testlerinde olduğu gıbı), MA adacıklarının ve PAG sınırlarında kararsız γ_R'in varlığından güçlü bir şekilde etkilenmektedir. CBB, kırılma yüzeyinde belirgin sünek özelliklerle birlikte çok daha yüksek darbe tokluğu gösterirken, CFB gevrek bir hasar eğilimi sergilemektedir. Bu durum esas olarak, kararsız γ_R'in ani dönüşümü ve MA adacıklarının kırılgan doğasından kaynaklanmaktadır. Sonuç olarak, ya PAG sınırları boyunca kırılgan bir ağ oluşumuna yol açarak tane sınırı kırılmasına ya da yüksek deformasyon hızlarında hızlı ayrışma ile tetiklenen klivaj kırılmasına neden olmaktadır. CFB, geliştirilmiş yarı-statik çekme özellikleriyle uyumlu olarak önemli ölçüde daha yüksek bir yorulma limitine sahip olmasına rağmen, CBB'ye kıyasla daha yüksek bir çatlak ilerleme hızı ve daha düşük bir gerilme şiddeti eşiği (ΔK_{th}) göstermektedir. CBB'de PAG sınırları yorulma çatlaklarını başarıyla saptırırken, CFB'de MA adacıkları ve kararsız östenitik bileşenler bu sınırları zayıflatmaktadır. Bunun sonucunda kırılgan ağ boyunca tane sınırı kırılması veya saptırma olmaksızın PAG sınırlarını kesen çatlaklar oluşmaktadır. Ancak çatlak bir PAG boyunca ilerlediğinde klivaj kırılması yerine sünek kırılma gözlemlenmekte ve bu durum, darbe testlerine kıyasla daha düşük deformasyon hızının etkisini ortaya koymaktadır.

Declaration on Publications

This dissertation includes the following articles, which have been published in international peer-reviewed journals in the field of materials science and engineering.

Publication I [1] – **O. Gulbay**, A. Gramlich, U. Krupp:

Effects of Silicon and Aluminum Alloying on Phase Transformation and Microstructure Evolution in Fe–0.2C–2.5Mn Steel: Insights from Continuous–Cooling–Transformation and Time–Temperature–Transformation Diagrams

Steel Research International (2024)

DOI: 10.1002/srin.202400159

Publication II [2] – **O. Gulbay**, M. Ackermann, A. Gramlich, A. R. Durmaz, I. Steinbach and U. Krupp:

Influence of Transformation Temperature on the High-Cycle Fatigue Performance of Carbide-Bearing and Carbide-Free Bainite

Steel Research International (2023)

DOI: 10.1002/srin.202300238

Publication III [3] – **O. Gulbay**, A. Gramlich, U. Krupp:

Impact Toughness and Fatigue Crack Propagation in Carbide-Free Bainite: The Adverse Role of Retained Austenite and Martensite-Austenite Islands

Fatigue & Fracture of Engineering Materials & Structures (2025)

DOI: 10.1111/ffe.70025

Additionally, the following supplementary international peer-reviewed journal article has been published with a contribution from the candidate.

Appendix I [4] – D. K. Nerella, M. A. Ali, H. Salama, **O. Gulbay**, M. Ackermann, O. Shchyglo, U. Krupp, I. Steinbach:

Automated Workflow for Phase-Field Simulations: Unveiling the Impact of Heat-Treatment Parameters on Bainitic Microstructure in Steel

Advanced Engineering Materials (2025)

DOI: 10.1002/adem.202400905

Table of Contents

List of Abbreviations

BCC	Body-centered cubic
BCT	Body-centered tetragonal
B_s	Bainite start temperature
CBB	Carbide-bearing bainite
CCT	continuous-cooling-transformation
CFB	Carbide-free bainite
EBSD	Electron backscatter diffraction
FCC	Face-centered cubic
HCF	High-cycle fatigue
K-S	Kurdjumov–Sachs
LCF	Low-cycle fatigue
LIT	Load increase test
LOM	Light optical microscopy
MA	Martensite-austenite
M_s	Martensite start temperature
N-W	Nishiyama-Wassermann
OPS	Oxide Polishing Suspension
OR	Orientation relationship
PAG	Prior austenite grain
PAGB	Prior austenite grain boundaries
PICC	Plasticity-induced crack closure
SDLE	Solute drag-like effect
SEM	Scanning electron microscope
SIF	Stress intensity factor
SYXRD	Synchrotron X-ray diffraction

TRIP	Transformation-induced plasticity
TTT	time-temperature-transformation
UTS	Ultimate tensile strength
VHCF	Very high-cycle fatigue
XRD	X-ray diffraction
YS	Yield strength
α_B	Bainitic ferrite
γ_R	Retained austenite
ΔK_{th}	Threshold of stress intensity factor range

List of Figures

1. Introduction

1.1. Motivation

Steel remains one of the most essential engineering materials in modern industry, offering a versatile range of mechanical properties that can be tailored to meet the demands of diverse and challenging engineering requirements, while maintaining cost-effectiveness that few other materials can match. Its adaptability for different applications makes it a cornerstone of structural and functional components worldwide. Moreover, giving research attention to developing enhanced steel grades with improved mechanical properties is crucial to increasing the longevity and reliability of engineering components. This is very important not only to improve engineering performance but also to contribute to environmental sustainability by promoting circularity in the steel industry [5]. Among the various microstructural forms of steel, bainitic steels (particularly carbide-free bainite) drew a notable amount of research interest due to their promising properties and lean alloying concepts [6,7]. Their exceptional balance of mechanical properties makes them attractive for demanding applications such as automotive components and railway infrastructure [8,9].

Despite these advantages, the design and optimization of bainitic steels remain challenging [10]. The hierarchical microstructure of bainite exhibits structural features down to the nanoscale. The microstructure consists of bainitic ferrite (α_B) as the primary phase and a carbon-enriched secondary phase, such as cementite or retained austenite (γ_R), and martensite-austenite (MA) islands, depending on the chemical composition and processing. The stability, morphology, and distribution of these constituents are sensitive to both alloying elements and processing conditions. Small variations in chemical composition and processing parameters can cause pronounced changes in the final microstructure, leading to substantial differences in mechanical performance, particularly in terms of fatigue life and impact toughness. Consequently, experimental characterization of bainitic steels becomes rather complex, and this complexity has hindered the development of predictive, systematic approaches to tailoring bainitic steels for specific service conditions. By focusing on systematic exploration of alloying effects, processing parameters, phase fractions, and their contributions, it becomes possible to move beyond isolated case studies and toward a coherent, data-driven framework for designing bainitic steels with tailored, high-performance service-relevant property profiles.

While quasi-static tensile properties are widely used to describe the mechanical properties of bainitic steels, they offer only a limited representation of mechanical performance under service-relevant conditions. Thus, mechanical performance must also be evaluated under

different loading scenarios, particularly in terms of fatigue resistance and impact toughness, for industrial relevance and a broader understanding of mechanical performance. This is especially important for complex and multi-component microstructures like bainite, where multiple interacting and codependent structural factors have an influence.

To achieve this, a comprehensive and integrated experimental approach is necessary to understand the impact of each microstructural feature on deformation behavior. Detailed microstructural characterization must be conducted, combining advanced techniques with quantitative image analysis, along with mechanical testing under service-relevant loading conditions. Only a well-structured experimental foundation can generate reliable and high-resolution datasets to isolate the influence of individual phases, validate multiscale simulations, and train data-driven predictive tools. By systematically investigating the role of alloying elements and processing parameters, a robust process-microstructure-property relationship for bainitic microstructure groups can be established. Such knowledge not only uncovers the correlations between individual microstructural constituents and mechanical performance but also guides the development of optimized alloying and processing strategies, enables predictive modelling of service behavior, and supports the design of bainitic steels with tailored property profiles for specific industrial applications. Therefore, addressing these challenges is essential for scientific curiosity and understanding, as well as for enabling intelligent, data-driven process design. In practice, this knowledge can be employed to:

- Develop systematic, reproducible approaches to bainitic microstructure characterization.
- Reduce reliance on subjective interpretation in microstructural assessment.
- Reveal correlations beyond conventional metallurgical design concepts.
- Provide a validated framework on the impact of individual phases on performance under varying service conditions.
- Lay the groundwork for automated, intelligent, and predictive workflow systems.

To conclude, the objective of this work is to find design strategies to optimize the overall mechanical performance of bainitic steels through tailored alloying and processing. The microstructure of various bainite groups, generated by different combinations of alloying elements and processing parameters, is characterized in detail using data-driven methods. Mechanical performance is evaluated under quasi-static tensile, cyclic, and dynamic loadings to describe the influence of individual phases on different service scenarios.

1.2. Material science of bainite

1.2.1. Origin and history of classification

During the early studies of Davenport and Bain [11] on the isothermal transformation of austenite at temperatures above the martensite start temperature but below the pearlite formation range, a new microstructure was found, appearing neither lamellar like pearlite nor acicular like martensite of the same material. Additionally, its transformation region formed a characteristic 'bay' in the time-temperature-transformation (TTT) diagrams, further distinguishing it as a separate transformation product. This microstructure exhibited a unique, sheaf-like appearance and displayed unusual but promising properties by having higher toughness than a martensitic structure of the same material, while exhibiting the same hardness. At first, the terms used for this microstructure in literature were based on its morphology and appearance, such as 'dark etching' and 'acicular aggregates'. Eventually, in the 1930s, the microstructure was named 'bainite' by E.C. Bain's colleagues in recognition of his significant contributions, as well as inspiring the studies [12]. In subsequent investigations, the term 'bainite' became well established with the further classification into 'upper bainite' and 'lower bainite', describing the distinct morphologies and transformation mechanisms depending on the transformation temperature, which are still being used up until today [13]. With the development of advanced high-resolution techniques over the years, the complexity of bainite has been revealed even further. Its definition and classification became increasingly miscellaneous and diversified.

1.2.2. Formation of bainitic microstructures

As a transformation product between pearlitic (diffusive) and martensitic transformations (displacive), bainite inherits complex phase transformation mechanisms and microstructures, which are strongly dependent on chemical composition, transformation temperature, and degree of deformation. This complexity has caused extensive debate in the field, particularly regarding the nature of bainitic transformation, whether it is diffusive or displacive [10,14]. Despite the strong controversies, microstructurally, all sides agree on a carbon-depleted bainitic ferrite (α_B) as the primary (dominant) phase and a carbon-enriched secondary phase in the microstructure, such as cementite or retained austenite (γ_R) [15].

The properties of bainitic steels are strongly influenced by the crystallographic texture, which develops as a result of the transformation from austenite. As in martensitic transformation, α_B exhibits an orientation relationship (OR) with its parent austenite grain [16]. It is generally described through different ORs, ranging from Nishiyama-Wassermann (N-W) to Kurdjumov–

Sachs (K-S) relationship. At higher transformation temperatures, this OR tends to align more closely to the N-W relationship, typically resulting in a maximum of three variants per packet. At lower temperatures, the OR shifts towards the K-S relationship, leading to six variants per packet [17,18]. However, it has become evident that the OR between parent austenite and α_B can never be exactly KS or NW [12]. On the other hand, it has also been shown that this OR aligns well within the Bain region, which includes both KS and NW relationships. The Bain strain is a pure lattice deformation that describes how the face-centered cubic (FCC) structure of austenite transforms into the body-centered cubic (BCC) or body-centered tetragonal (BCT) structure of ferrite or martensite, without encountering the rotation and accommodation of strains, which defines the Bain region [12]. Therefore, it is important to point out that α_B always exhibits an OR, which is close to KS or NW and well within the Bain region. In any consequence, the final microstructure consists of a significant amount of inter-variant boundaries, including phase-, block-, packet-, and prior austenite grain boundaries (PAGB) [16,19]. An illustration of this hierarchical organization is displayed in **Figure 1**.

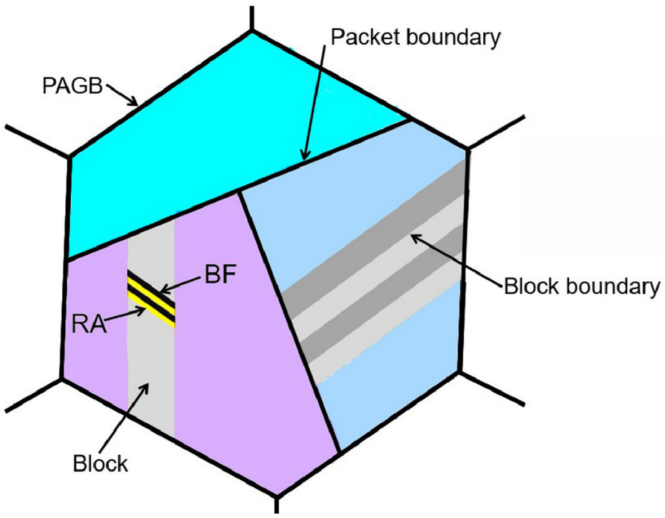

Figure 1. Schematic representation of an austenite grain displaying the hierarchy of carbide-free bainitic microstructure [19].

Classification of bainite morphologies

The performance of bainitic steels is closely linked to the features of their microstructural constituents, which can be strongly adjusted through chemical composition and processing parameters [15,20–22]. Over the years since the 1920s, the complexity of bainitic microstructures has been revealed, especially with the development of advanced characterization techniques. Along with this, several classification schemes evolved to describe the bainitic microstructures based on a variety of aspects, such as morphology, secondary phases, formation temperature, and composition [13,23–25].

One of the first classifications was introduced by Mehl in 1939 [13]. He defined upper and lower bainite in **carbide-bearing bainite (CBB)**, based on how carbides form at different isothermal transformation temperatures. This definition is still used today. When there is no kinetic hindrance, cementite can precipitate as a secondary phase. During bainitic transformation, carbon is partitioned from the α_B into the surrounding austenite. In other words, austenite is enriched with carbon, and carbide precipitation becomes possible when the solubility limit is exceeded. The formation of carbides reduces the carbon concentration in austenite and induces the further formation of α_B [12]. An illustration of this mechanism is displayed in **Figure 2**. At elevated temperatures, carbide precipitation occurs predominantly between α_B plates, forming upper bainite. Conversely, at lower temperatures, the limited carbon diffusivity can result in carbon being trapped or precipitated within supersaturated ferrite. This restricted diffusion inhibits efficient carbon partitioning into the surrounding austenite, leading to a finer distribution of carbides, both intergranularly between and intragranularly within the α_B plates, forming lower bainite [12,26]. The intergranular carbides within the α_B plates tend to form at an angle of approximately 60° to the long dimension of the α_B plates (**Figure 2**).

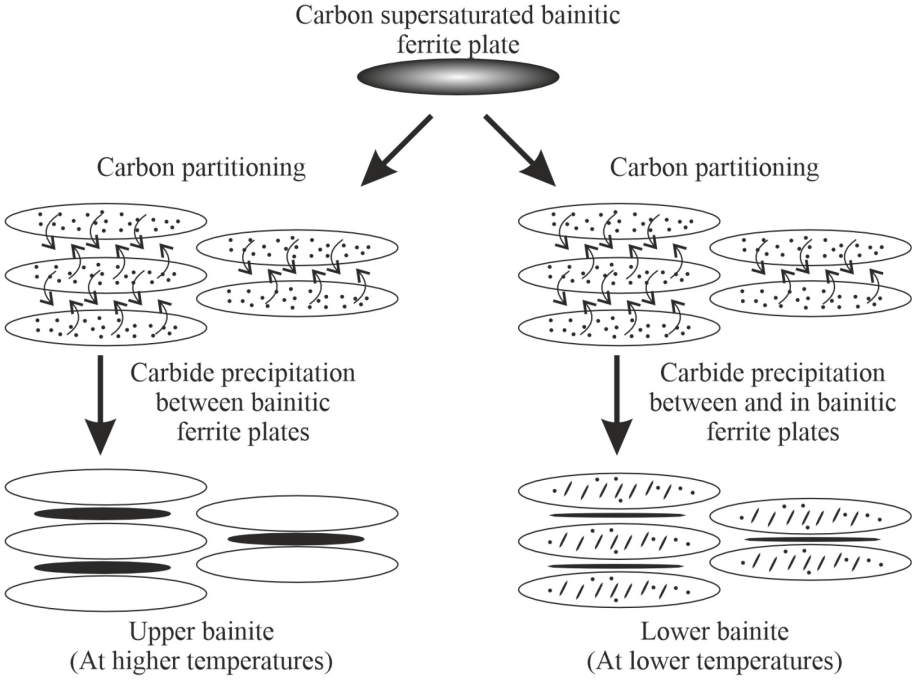

Figure 2. Schematic representation of bainitic transformation, illustrating the different formation mechanisms of upper and lower bainite (reconstructed from [27]).

With the introduction of considerably large concentrations of Si and Al to steel [28–32], cementite precipitation is prevented during bainitic transformation, making it possible to generate **carbide-free bainite (CFB)** consisting of α_B and γ_R. This effect arises from the inherently low solubility of these elements in cementite, which impedes carbide precipitation

[9,33]. Consequently, carbon is enriched in the surrounding austenite and acts as a stabilizer. As a result, γ_R can be introduced at room temperature as a secondary phase [33,34].

The introduction of CFB has introduced additional microstructural complexity, thereby necessitating a more detailed and nuanced definition and classification of bainite. Zajac et al. [24] published a uniform terminology to describe bainitic microstructures, which identified bainite as a non-lamellar two-phase decomposition product of austenite. Moreover, five bainite morphologies were recognized: granular bainite, upper bainite, degenerate upper bainite, lower bainite, and degenerate lower bainite. The term 'degenerate' refers to the events where cementite formation is prevented, and carbo-enriched retained austenite or martensite constituents are formed instead.

A more general classification of the bainitic microstructure was established by Gerdemann [25]. In this classification method, more detailed descriptions of primary and secondary phases were considered, including the location of the secondary phase in the microstructure. **Table 1** shows an overview of the classification in the study for bainitic features.

Table 1. Classification scheme for bainite according to Gerdemann [25].

Primary phase		**S**econdary phase		
Crystallographic structure	Morphology	Location	Crystallographic structure	Morphology
BCC (Ferrite)	**P**olygonal[1]	Inter-granular (**B**oundary)	Hex (**C**arbides)	**R**ound[1]
	Quasi-polygonal[1]	**I**ntra-granular	BCT (**M**artensite)	**E**longated[2]
	Granular		FCC (**A**ustenite)	**L**ath-like[2]
	Widmanstätten		**N**one	**F**ilm-like[2]
	Acicular[2]			**C**lustered
	Lath-like[2]			

[1]Roundness (Difference between the smallest enclosing and smallest enclosed ellipse)

[2]Aspect ratio (Length to width ratio)

In recent years, the majority of the bainite studies have focused on isothermally formed microstructures and, for simplicity, have predominantly categorized them according to their secondary phase, as previously noted, as carbide-bearing bainite (CBB) and carbide-free bainite (CFB) [8,21,35–38].

Incomplete transformation phenomenon

The addition of Si and/or Al in amounts greater than 1 wt.-% can retard the formation of cementite [15,39]. Thus, the CFB microstructure typically consists of α_B plates (subunits)

separated by carbon-enriched γ_R films, forming sheaves (agglomerations of the subunits with identical orientation), following an isothermal heat treatment procedure, as shown in **Figure 3**. However, in these circumstances, the volume fraction of α_B, which forms during isothermal transformation, is limited by the incomplete reaction phenomenon (T_0 concept). This concept, introduced by Bhadeshia [40], explains the temporary cessation of ferrite formation before the full transformation of austenite is achieved (according to the lever rule) in the absence of carbide precipitation. Under the assumption of diffusionless transformation of bainite, the phase transformation is only possible when the carbon concentration of austenite is below a critical threshold. When the critical value is reached, further transformation of austenite into bainite is impossible at the same temperature, which is determined by the T_0 curve (**Figure 4**a). Bainitic transformation proceeds only if the free energy difference between austenite and ferrite is negative. For a carbon concentration at T_0, where the free energy difference is zero at a given isothermal temperature, the transformation stops (**Figure 4**a).

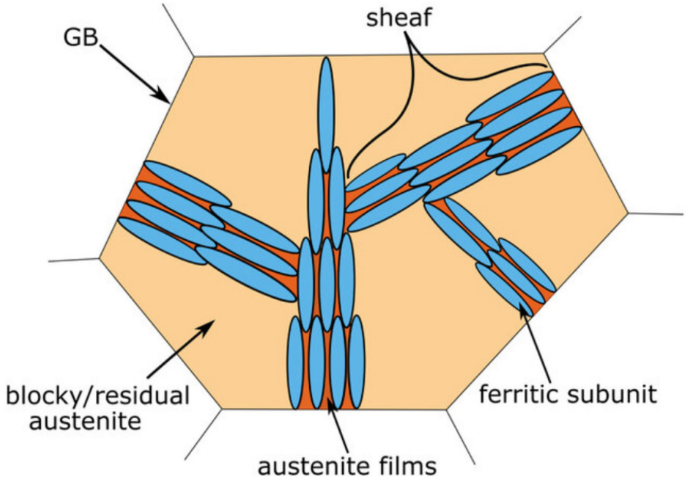

Figure 3. Illustration of a carbide-free microstructure consisting of bainitic ferrite plates (subunits), retained austenite films, and formation of blocky retained austenite (possibly martensite-austenite islands in subsequent cooling) [41].

In CFB, changes in the transformation temperatures significantly influence the resulting microstructure, similar to CBB. As indicated in **Figure 4**a, decreasing the isothermal transformation temperature allows more carbon partitioning into the surrounding austenite, as the carbon threshold of austenite increases before bainitic transformation ceases. This occurs due to the increased free energy difference between α_B and austenite at lower temperatures, leading to the formation of more α_B and increased carbon partitioning. Chang et al. [42] introduced a method to estimate the thickness of austenite films between α_B plates during bainite transformation, as illustrated in **Figure 4**b. When an α_B plate develops (sub-unit 1), the carbon is partitioned into the surrounding austenite, leading to the development of a carbon-diffusion

field around the α_B plate. The carbon concentration in this field drops with increasing distance from the α_B plate, as shown in **Figure 4**b. Moreover, according to the T_0 concept, the spontaneous transformation from austenite to α_B can only take place when the carbon concentration in austenite is below the threshold value ($X_{CT'0}$). Based on this mechanism, the thickness of the γ_R films can be controlled by the transformation temperature, as the threshold carbon concentration in austenite increases with decreasing transformation temperature. This means the next parallel α_B plate can form at a higher carbon concentration with a smaller distance, which is inherited as thinner γ_R films between α_B plates and finer microstructure.

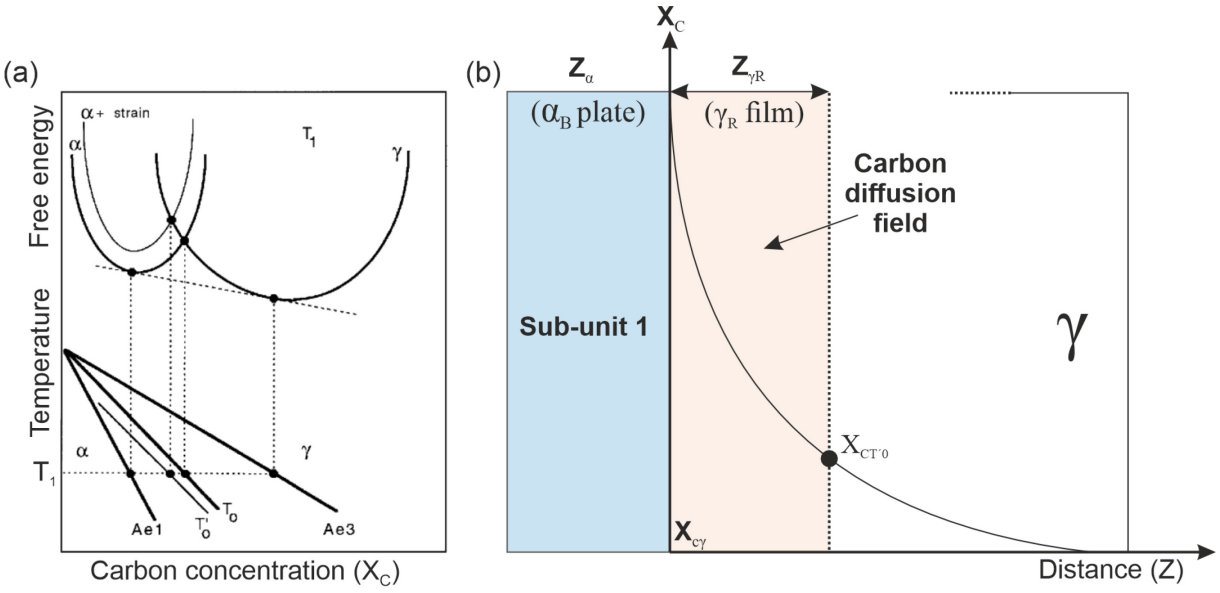

Figure 4. Schematic representation of the T_0 concept (T'_0 also takes the strain energy into account) [12]. (b) Schematic representation of austenite film thickness estimation between bainitic ferrite plates (reconstructed from [42]).

However, in most cases, not all austenite transforms into thin films. As illustrated in **Figure 3**, some regions retain a blocky morphology, primarily located at prior austenite grain boundaries (PAGB). Since these blocky regions do not fully undergo bainitic transformation, the carbon partitioning remains incomplete. Due to their size, morphology, and incomplete carbon enrichment, their stability remains insufficient, making them more prone to undergo martensitic transformation upon cooling. This leads to the formation of martensite-austenite (MA) islands and/or unstable blocky γ_R formation in the final microstructure [28,43]. It has been shown in multiple studies [15,20,44] that film-like γ_R between the α_B plates is both chemically and mechanically more stable than the MA islands formed during subsequent cooling, as well as the larger, blocky austenitic regions that remain in the microstructure. Therefore, the formation of these constituents is often considered undesirable due to their potential adverse effects on mechanical properties [44–46].

Nano-bainitic microstructures

In the early 2000s, Caballero and Bhadeshia [46] introduced a novel approach to minimize the blocky austenitic regions in the CFB microstructure and generate exceptionally strong bainite. This was achieved by lowering the bainite start temperature (B_s) significantly down to 125 °C by introducing carbon concentrations up to 1 wt.-%. The resulting microstructure comprised ultra-fine nanoscale α_B plates, 20 – 40 nm thick, surrounded by highly stable γ_R films, and minimized blocky austenitic regions, especially due to the increased amount of bainitic reaction. This group of alloys was later called nano-bainitic steels. This design yielded remarkable mechanical properties, including an ultimate tensile strength (UTS) of 2.5 GPa, a hardness exceeding 600 HV, and impressive fracture toughness (K_{Ic}) in the range of 30 – 40 MPa·$m^{1/2}$. Even though high carbon concentration promotes a finer bainitic microstructure by enabling transformation at lower temperatures, it significantly slows down the transformation kinetics, extending the required holding time to as much as 30 days [16,46–48]. Although the development of new alloying concepts over the years has allowed for a reduction in transformation time [19,49], it has remained relatively long, exceeding 15 hours, which limits the industrial applicability.

1.2.3. Influence of alloying elements in bainite

The influence of alloying elements on bainitic steels is critical, as in other steels, in tailoring the transformation behavior, microstructure, and mechanical properties. Alloying elements can significantly change phase stability, phase transformation temperatures and kinetics, which modify the final microstructure. Thus, a comprehensive understanding of these effects is essential for the proper design of bainitic steels, specifically for intended applications. In the following sub-sections, the influence of most important elements is discussed.

Carbon

It is well-known that increasing carbon concentration decreases the martensite start temperature (M_s) as well as the bainite start temperature (B_s) [50]. It is reported that an increased carbon concentration retards the bainite transformation and prolongs the incubation of the bainitic reaction [51]. In CBB steels, increased carbon concentrations increase the supersaturation of α_B, leading to increased carbide precipitation. It has a significant influence on the stability and strength of austenite, which improves the chemical stability of austenite against phase transformation. Particularly in CFB steels, carbon in γ_R has a direct influence on the mechanical properties, as the mechanical stability of austenite enhances with increasing carbon concentration. In addition to that, the strength of austenite is an effective factor that influences

α_B plate thickness, as mechanically stronger austenite with higher carbon concentration will have a greater resistance against the advancement of α_B at the phase interface [52].

Manganese

As in most steels, manganese is crucial to achieving hardenability [53,54]. Similar to carbon, manganese is a very strong austenite stabilizing element, which decreases M_s and B_s [55,56]. In addition, bainite transformation kinetics and incubation time are slowed down by increasing Mn concentrations [51,57], which can be attributed to the influence of Mn on austenite stability. As an austenite-stabilizing element, Mn decreases the free energy difference between ferrite and austenite. This is reflected as prolonged incubation times and slower transformation kinetics, as the driving force is reduced [51]. Furthermore, Mn tends to segregate at PAG and phase boundaries, which reduces the mobility of the interface due to the solute drag-like effect (SDLE). As a result, the resistance against bainite growth increases and slows down the transformation kinetics [55].

Silicon and Aluminum

Si and Al have similar effects on bainite and have great importance, especially on the design of CFB microstructures. Both elements are effectively used to retard carbide precipitation due to their insolubility in cementite [58,59]. When the cementite is forced to inherit the Si/Al in para-equilibrium conditions (as in bainitic transformation), the driving force drops significantly. This slows down the precipitation kinetics, effectively retarding cementite precipitation [12,33]. Consequently, the excessive carbon that is rejected from α_B is enriched in the surrounding austenite during bainitic transformation, leading to the stabilization of austenite at room temperature [51]. In other words, Si and Al enable the generation of CFB microstructures.

Approximately 1 wt.-% Si and/or Al is sufficient to suppress the carbide precipitation [21,35]. However, for industrial applications, Si alloying is limited due to possible surface defects, particularly during the continuous casting process [60], due to the formation of a low-melting eutectic infiltrating the steel along the austenite grain boundaries, causing intergranular oxidation during highly oxidizing conditions at high temperatures [61]. Additionally, it was also reported that Si may deteriorate the galvanizability of the steel through the formation of hard and stable Mn_2SiO_4 oxide films on the steel surface [9]. As a substitute, too much Al alloying may increase the M_s [62], which increases the bainite transformation temperatures. It was also found that the higher Al alloying in combination with Mn reduces the hot ductility [63]. Moreover, Al has a significantly less solid solution hardening effect compared to Si [29]. On the other hand, it increases the transformation kinetics and promotes α_B formation [29,31].

It has been reported that the combined alloying concepts of Si and Al could be beneficial to achieve optimum properties [9].

Chromium

As one of the most frequently used alloying elements in steel, Cr is used to improve the hardenability of steel [48] and is known as a very strong carbide former [64]. Similar to Mn, Cr also decreases the B_s and increases the incubation period for the bainitic transformation [51]. One of the reasons for this is explained by the limited diffusion of carbon due to SDLE, as in Mn, by accumulating at the phase boundaries with other substitutional alloying elements [65]. Additionally, it decreases the Gibbs free energy difference between ferrite and austenite, which additionally contributes to the slower bainite transformation kinetics [51]. On the other hand, this element creates a transformation-free gap between pearlite and bainite during continuous cooling, facilitating the formation of larger bainite fractions without forming pearlite [66].

Molybdenum and Boron

As Mo is a carbide-forming element, it is commonly used to improve the hardenability of steels [25]. Although Mo is a ferrite-forming element, it is widely used to retard the formation of ferrite and pearlite [10]. This is explained by the segregation of Mo at austenite grain boundaries. Accordingly, the effectiveness of ferrite formation is reduced as the nucleation sites are occupied by Mo [67]. In addition to that, Mo may form carbides, which slows down the carbon diffusion, leading to a delay of pearlite formation [64]. It was reported that it has no significant influence on B_s, while it increases M_s slightly by fractions above 0.5 wt.-% [51].

Boron segregates at austenite grain boundaries, as Mo, where it strongly suppresses the formation of ferrite and pearlite, enhancing the hardenability during continuous cooling by reducing the activity of C [68]. However, B has a very high affinity to form nitrides or carbides that are stable at very high temperatures, which can reduce the effectiveness of B [69]. Hence, Ti alloying is often employed to tie up N, allowing B to remain in the solid solution and be effective at grain boundaries [70].

1.3. Mechanical performance of bainitic steels

The development of steel alloys with improved mechanical properties is essential to enhance the longevity and reliability of engineering components. This not only improves the engineering performance but also contributes to environmental sustainability by promoting the circularity of the steel industry [5,71]. Over the decades, different variants of bainitic steels drew a

significant amount of research attention to achieve this goal due to their promising properties and low alloying concepts [6,7,15,37,41,72,73].

The microstructure of bainitic steels can be significantly altered by chemical composition and processing, which ultimately influences the mechanical properties [12,58,64,73,74]. Most commonly, the quasi-static tensile properties of bainitic steels, especially carbide-free variants, are reported with a very good combination of strength and ductility [35,58,59]. Multiple studies revealed that CFB steels achieve comparable quasi-static tensile properties to 3rd generation advanced high-strength and martensitic steels [15,20,75]. Particularly, with the introduction of retained austenite as the secondary phase in CFB, excellent quasi-static tensile properties are obtained associated with the transformation-induced plasticity (TRIP) effect. Under uniaxial loading, the gradual transformation of γ_R to martensite results in high strength levels with improved elongation. Especially with the development of nano-bainitic steels, it has become possible to generate bainitic steels exhibiting tensile strengths exceeding 2 GPa and tensile elongation around 20% [19,46,49], although with prolonged transformation times. A comparison of tensile elongation and tensile strength of different steels with bainitic steels is displayed in **Figure 5**.

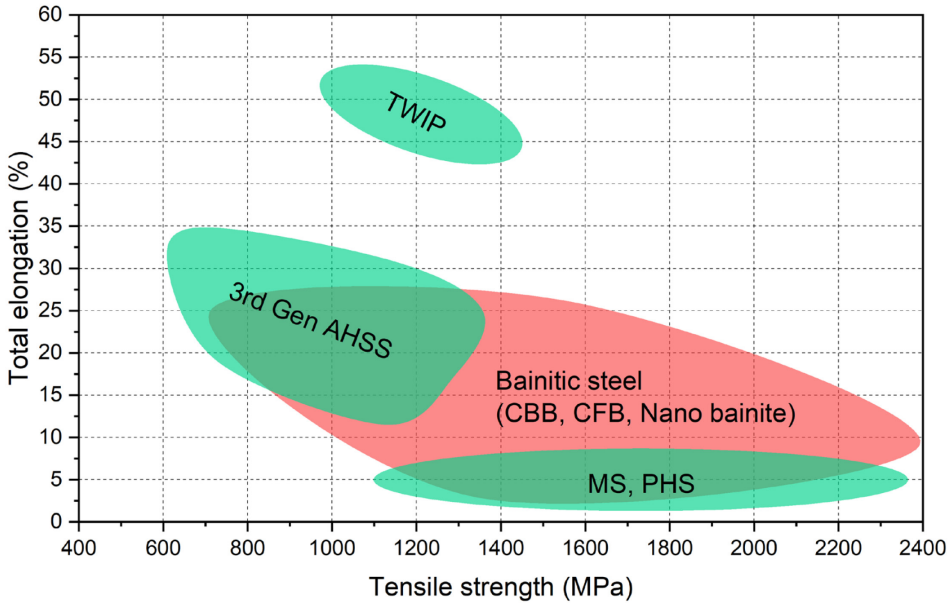

Figure 5. Balance of tensile elongation and tensile strength of different alloys compared to bainitic steels.

Strength and ductility

Besides processing, the strength of bainite can be influenced by many other factors, including strengthening due to substitutional and interstitial elements, dislocation strengthening, as well as precipitation hardening in the case of CBB steels [12]. In parallel, since α_B is a stronger phase

than austenite, the α_B characteristics play an important role in the overall strength of bainitic steels [76].

According to the T_0 concept in CFB alloys, with a decrease in transformation temperature, the α_B fraction can be increased while decreasing the plate thickness. This not only refines the microstructure but also enhances the dislocation strengthening [64]. Thus, yield strength (YS) increases [76,77]. Additionally, in CFB steels, the γ_R can transform to martensite via transformation-induced plasticity under mechanical loading, which contributes to tensile strength while improving ductility [77].

In the case of CBB, excessive carbon precipitates most commonly as cementite. During deformation, mobile dislocations have to bypass hard cementite precipitates (Orowan mechanism) as they are not able to shear them, which enhances the tensile strength. In addition to that, lower transformation temperatures lead to finer cementite precipitation along with finer α_B plate thickness, which improves the strength as well as the ductility of the material as the effective grain size decreases [12].

Impact toughness

Highly misoriented microstructural obstacles formed as a result of the displacive transformation of α_B, following an orientation relationship with the parent austenite phase, such as packet and block boundaries, improve the impact toughness [78]. Conventional CBB is influenced by the existence of carbides (size and distribution), which can act as crack initiation sites under impact loading.

It has been shown that the finer carbide distribution obtained at lower transformation temperatures can improve the impact toughness, even at higher strength values. The cracks that form from the fine cementite precipitates are smaller in comparison. Therefore, their propagation into α_B is impeded, leading to higher impact toughness than high-temperature CBB [12].

In CFB, it has been shown that the γ_R fraction influences the impact toughness energy of the materials. In multiple studies conducted on high-carbon and Si-rich alloys [77,79], extensive amounts of γ_R (up to 30%) were found to be very beneficial, particularly in film-like morphology between α_B plates. This was associated with the strong stabilization of γ_R with a high amount of carbon at increased fractions. However, in the majority of cases, γ_R not only exists in film-like morphology, but also in blocky morphology located on PAGBs or as MA islands after subsequent cooling. Caballero et al. [39] mentioned that the coarse MA islands can

be a factor contributing to the deterioration of the impact toughness. Additionally, the influence of the MA islands was discussed in the context of the welding of pipeline steels [80–83]. It was shown that MA islands formed on PAGBs result in complete debonding, leading to cleavage fracture during impact loading.

Cyclic mechanical properties

Evaluating only quasi-static tensile properties is not sufficient to assess the overall mechanical performance. Therefore, cyclic properties must also be considered to ensure a comprehensive assessment under different loading conditions and to determine the materials' suitability for specific applications. Since the formation of bainite and martensite is codependent, and both originate from primarily displacive transformation mechanisms, making their comparison is notably relevant in the context of fatigue performance of high-strength steels. This is particularly important for understanding and differentiating the underlying fatigue mechanisms, particularly in HCF regimes. Given that the fatigue behavior of martensite is comparatively well understood, this knowledge can be used as a foundation for interpreting and elucidating the fatigue mechanisms in bainitic microstructures. Nevertheless, their comparison is not straightforward, particularly due to various types of bainitic microstructures such as CBB, CFB, upper bainite, lower bainite, and nano-bainite.

The localization of cyclic plasticity within slip bands is widely recognized as a primary precursor to fatigue crack initiation [84–89]. In martensitic microstructures, these slip bands are predominantly located along the lath boundaries oriented at 45° to the loading axis, corresponding to the maximum shear stress plane, which ultimately leads to crack initiation with continued cyclic loading [85]. This correlation between the maximum shear stress plane and slip band formation highlights its critical role in determining crack initiation sites, a mechanism that is also observed in bainitic steels with favorably oriented features [90]. However, the exact location of the crack initiation is still not well understood in both microstructures [84]. Additionally, the cracking mechanisms in the HCF regime appear to be different from those in the low-cycle fatigue (LCF) regime for many metallic materials [84]. In LCF, while slip bands typically form early in the fatigue life and are widely distributed across the specimen surface, in HCF, they are more isolated, confined to favorable locations, and persist for most of the fatigue life. In the HCF regime, the slip band formation and progression are strongly influenced by the local microstructure [91,92].

Krupp et al. [93] investigated the fatigue behavior of thermomechanically processed micro-alloyed forging steel in self-tempered martensitic and lower CBB conditions. The

homogeneously distributed nano-size cementite precipitates contributed to very high fatigue strength and limit at high-cycle and very high-cycle fatigue regimes (HCF and VHCF, respectively) compared to the lower CBB with larger cementite precipitates. It was stated that the failures at VHCF regimes in tempered martensite initiated at non-metallic inclusions, while no non-metallic inclusion was identified as a crack initiation site in lower CBB. This surprising result was attributed to the larger PAG size of the bainite condition, leading to local stress concentrations exceeding the stress concentrations at non-metallic inclusions, and the lower matrix strength of bainite, increasing the cyclic plasticity around the crack-initiating defect. Similarly, in another study [90], an internal non-inclusion crack initiation was also observed in a CFB microstructure under uniaxial fatigue loading with a stress ratio of R = 0.1. This was attributed to the pile-up of dislocation dipoles at PAGBs in slip bands, which increases local stress concentrations and promotes micro-crack nucleation and growth.

Baek et al. [94] studied the HCF behavior of martensite/bainite (M/B) steels as a function of phase fractions, concluding that the material state with a larger martensite fraction exhibits improved fatigue strength. It was additionally stated that the M/B boundaries act as stress concentrators, leading to the formation of cracks. In another study conducted by Zhao et al. [95] on VHCF of martensite/bainite multiphase steel, it was shown that the plastic deformation occurred in the bainite lath leads to debonding from the adjacent martensite, which results in crack initiation at grain boundaries between large bainite laths and martensite. Similarly, Chen et al. [96] investigated fatigue cracking resistance of M/B steels with bainite fractions ranging from 21% to 70%. It was revealed that the plasticity-induced crack closure (PICC) effect is more pronounced with increasing bainite fraction, relating it to the increased plastic zone at the crack tip. On the other hand, the fatigue cracks were deflected more frequently and effectively by martensite packets. Correspondingly, while the fatigue improves with increasing bainite fraction, the crack deflection worsens, concluding that there should be a trade-off between these two mechanisms influencing the fatigue cracking resistance. Consequently, the material states with a bainite fraction between 49% and 60% exhibited higher crack resistance, which was attributed to the simultaneous roles of PICC and crack deflection.

It has been reported that the resistance against fatigue crack propagation is significantly influenced by the size, dimension, and crystallographic features of bainite packets and blocks [19,97], similar to what is observed in martensite [92,98]**.** As a consequence of the displacive transformation of α_B, the microstructure exhibits a high degree of misorientation with a significant amount of inter-variant boundaries as a result of hierarchy. These boundaries can

serve as effective barriers to fatigue crack propagation, similar to the effect observed in martensitic microstructures [99]. **Figure 6**a illustrates possible microstructural barriers, consisting of PAG, packet, and block boundaries. It is well established that the high density of these boundaries and internal dislocations within martensitic laths is a key factor contributing to the high fatigue performance of martensitic steels [84,86].

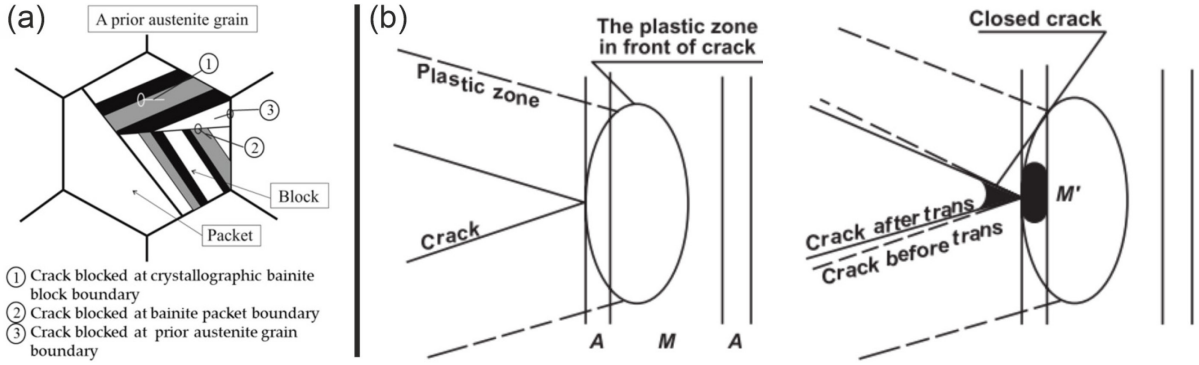

Figure 6: (a) Scheme of a bainitic microstructure illustrating possible microstructural barriers for a growing fatigue crack [99]. (b) A schematic representation showing the influence of strain-induced transformation of austenite to martensite at the crack tip [100].

Rementeria et al. [97] showed that the fatigue crack in a nano-bainitic microstructure is significantly deflected at the phase boundaries if they are located between two different bainite blocks or packets. However, the phase boundaries in a bainite block were ineffective in deflecting the crack. This suggests that the crack does not change orientation significantly at the phase interface between the α_B plate and the γ_R film, as the austenite phase has many more equivalent slip systems than ferrite, which increases the probability of an available slip system with a similar orientation as the prior ferrite. On the other hand, high-angle boundaries, such as block, packet, and PAG boundaries, act as effective obstacles that deflect the fatigue crack. In another study on nano-bainitic steels [99], it was stated that the size of critical crack length lies between the size of bainite block width and block length (**Figure 7**a), concluding that the bainite block size is the main obstacle for short fatigue cracks and governs the fatigue limit.

The isothermally produced CFB steels, however, have rather complex multi-component microstructures consisting of α_B plates surrounded by γ_R films. Moreover, in most cases, the microstructure also exhibits MA islands. This increases the number of effective factors on fatigue properties and brings complexity to understanding microstructure-fatigue crack interaction. On one hand, compared to α_B and martensite, austenite is a softer phase that is more susceptible to localized deformation, inducing fatigue crack initiation due to local plasticity exhaustion or high stress concentrations at the phase boundaries [91,101]. On the other hand,

the γ_R at the crack tip may transform to martensite due to the TRIP effect and decelerate crack propagation by volume expansion, energy absorption, and crack closure effects (**Figure 6**b) [100]. Long et al. [35] studied the fatigue properties of CFB and CBB steels under total strain amplitude. It was stated that carbides, as a secondary phase, cause stress concentration during cyclic loading, leading to deterioration of fatigue life, while metastable γ_R improves the fatigue life under total strain amplitude due to martensitic transformation. Yang et al. [102] found that increased γ_R fraction in a nanostructured bainitic steel increases the fatigue limit at cycles of 10^7. It was expressed that the fatigue limit of the nanostructured bainitic steels is influenced by the microstructure rather than the strength and hardness. Wenyan et al. [103] studied the influence of γ_R fraction in CFB steel specimens ranging between 8 – 23%. It was found that the threshold of stress intensity factor (SIF) range increased, and the crack propagation rate decreased with increasing γ_R fraction (**Figure 7**b). Kumar et al. [104] published similar findings on the influence of γ_R fraction in a study conducted on nano-bainitic steel.

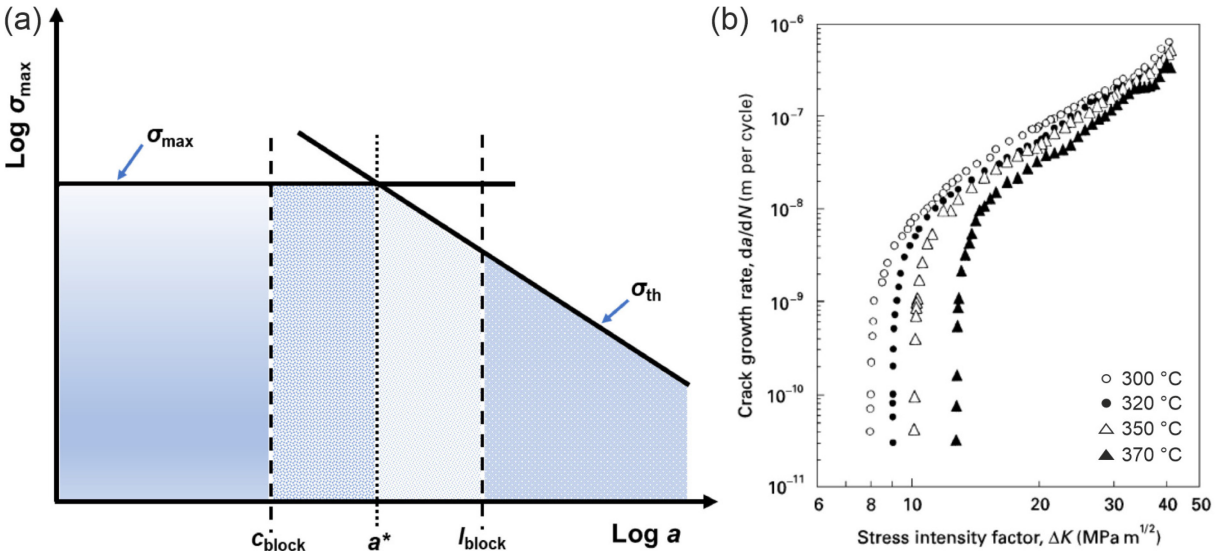

Figure 7. (a) Kitagawa diagram illustrating the critical defect length in relation to the length and width of the bainite block [19], (b) Fatigue crack propagation rate as a function of bainite transformation temperature [103]

Conversely, unstable blocky γ_R and MA islands can be detrimental. Gao et al. [44] studied the role of γ_R morphology on fatigue crack initiation and propagation. It was stated that the film-like γ_R between the α_B plates arrests the fatigue crack via transforming to martensite, while blocky γ_R or MA islands located on PAGBs cause intergranular cracking. In other words, the morphology, size, fraction, and stability of secondary phases (γ_R and MA islands) influence fatigue properties considerably. In this respect, the positive aspects of having advantageous misoriented barriers against fatigue cracks can be outweighed by the unfavorable features of microstructural constituents, leading to a deterioration of fatigue properties.

In summary, the mechanical performance of bainitic steels is governed by a multitude of factors, including chemical composition, processing parameters, and the type and characteristics of individual microstructural constituents. This inherent complexity brings additional challenges in establishing clear correlations between bainitic microstructures and mechanical properties, particularly for mechanisms as complex as fatigue. Consequently, a holistic and integrated approach is required to understand the role of each microstructural feature in deformation behavior, thereby enabling the targeted design of bainitic steels for specific engineering applications.

2. Objective and scope

The primary objective of this work is to find design strategies to optimize the overall mechanical performance of bainitic steels through alloying and processing. For this purpose, the effects of Si and Al, key alloying elements for preventing carbide formation and for generating carbide-free bainite (CFB), on phase transformation and microstructural evolution are systematically investigated in a Fe–0.2C–2.5Mn base-alloy. To isolate the individual effect of each alloying element, Si and Al were completely substituted for one another in the alloy design. By focusing on this relatively simplified alloy system, the study aims to establish the fundamental effect of these elements, while providing a robust experimental basis for simulations and data-driven modelling efforts conducted in connected works. Consequently, a more complex alloying system was deliberately avoided at this stage. Furthermore, the influence of transformation temperature on the quasi-static tensile properties and high-cycle fatigue (HCF) performance of carbide-bearing bainite (CBB) and CFB microstructures is comparatively assessed. Finally, the mechanical response under various loading conditions is analyzed to elucidate the complex role of microstructural constituents, particularly retained austenite and martensite–austenite (MA) islands in CFB, particularly in controlling fatigue crack resistance, impact toughness, and fracture mechanisms.

In this context, the following aspects are addressed through a comprehensive mechanical, microstructural, and fractographic investigation employing multiple techniques, including SEM, EBSD, and synchrotron X-ray diffraction (SYXRD).

- Phase transformation characteristics and microstructural features of CBB and CFB microstructures under continuous and isothermal cooling conditions.
- Determination of experimental continuous-cooling-transformation (CCT) and time-temperature-transformation (TTT) diagrams, along with the development of an empirical formula to estimate M_s for the studied materials and beyond.
- Influence of Si and Al on CFB microstructure and phase transformation behavior through complete substitution of these elements.
- Effect of isothermal phase transformation temperature on quasi-static tensile and HCF performance of CBB and CFB.
- Mechanical performance of CBB and CFB under bending fatigue and impact loading.
- Microstructural features controlling the crack propagation in CBB and CFB.
- Role of retained austenite and MA islands in crack propagation behavior within the CFB microstructure.

3. Experimental section

The following subsections provide a brief overview of the most important experimental methods that were used in this study. Each method was selected and employed with respect to the specific aims of the study, ensuring reproducibility and relevance of the investigated phenomenon. Detailed descriptions are provided to allow a clear understanding of the experimental workflow and the interpretation of the obtained results.

3.1. Materials and processing

Three steel ingots (80kg) were produced in a laboratory-scale vacuum induction furnace with nominal compositions of Fe–0.2C–2.5Mn, Fe–0.2C–2.5Mn–1.5Si, and Fe–0.2C–2.5Mn–1.5Al (wt%). The ingots, with a cross-section of 140 × 140 mm², were homogenized at 1200 °C and then forged into billets with a cross-section of 60 × 60 mm². Subsequently, a second homogenization process at 1200 °C for 5 hours was carried out, followed by furnace cooling. The specimens required for the planned experiments were machined and extracted from these billets. The measured chemical compositions of the alloys investigated in this study are shown in **Table 2**. Si and Al are added to the alloy composition to generate a CFB microstructure. In order to isolate the individual effect of Si and Al, they were completely substituted for one another. Medium carbon concentrations were used for sufficient strength and austenite stability, while hardenability is enhanced by Mn.

Table 2. Chemical composition of the investigated alloys. Optical emission spectroscopy (OES) was employed to determine the chemical compositions, while carbon was determined with combustion analysis.

Alloy	C	Mn	Si	Al	P	S	Cr	Mo
CBB	0.18	2.48	0.01	0.002	0.003	0.002	0.04	0.01
CFB-Si	0.19	2.38	1.48	0.003	0.003	0.003	0.04	0.01
CFB-Al	0.19	2.46	0.01	1.41	0.004	0.003	0.04	0.02

3.2. Dilatometry

Phase transformation temperatures and transformation behavior during heat treatments were determined using a DIL 805A/D (TA Instruments, Germany) dilatometer with rectangular specimens measuring 4.0 × 7.0 × 1.4 mm³ under vacuum conditions. Firstly, the Ac_1 and Ac_3 temperatures were identified using a heating rate of 0.005 K/s. Second, the CCT diagrams of the studied steels were constructed by performing 12 experiments per alloy. A heating rate of 3.33 K/s was applied, and specimens were austenitized at Ac_3 + 60 K for 600 seconds to ensure

a fully austenitic microstructure. Following austenitization, specimens were continuously cooled to room temperature at various cooling rates. The martensite start temperature (M_s) was determined from the cooling curves that showed only martensitic transformation, while the bainite start temperature (B_s) was derived from the cooling curves without any prior phase transformation. The average values from these measurements were taken as the characteristic transformation temperatures. To complete the CCT diagrams, the phase fractions of the obtained microstructures were quantified using light optical microscopy (LOM), and the specimen hardness was measured to establish correlations. Finally, to partially construct TTT diagrams for the bainitic transformation region, the same austenitization conditions were employed. Specimens were then cooled to various temperatures above M_s and held isothermally for 30 minutes to ensure complete bainitic transformation.

3.3. Scanning electron microscopy (SEM)

SEM was performed for both microstructural and fractographic examinations using a field-emission gun ZEISS SIGMA SEM (Carl Zeiss Microscopy GmbH, Germany). For the microstructural investigations, specimen preparations involved wet mechanical grinding with SiC abrasive paper up to 1200 grit, followed by polishing using diamond paste with particle sizes of 6 µm and 1 µm, respectively. The polished specimens were then etched with 3% HNO_3 (Nital) to reveal the microstructure. The investigations were carried out using an aperture size of 30-75 µm, an accelerating voltage of 15-20 kV, and a working distance of 9-20 mm with the secondary electron (SE) detector. For the high-resolution measurements using the InLens detector, an accelerating voltage of 5 kV and a working distance of 2 mm were employed.

3.4. Electron backscatter diffraction (EBSD)

Further microstructural and crystallographic analyses of the dilatometer, tensile, and bending fatigue specimens were accomplished using EBSD. For this purpose, the specimens were mechanically ground and polished, as previously described in section 3.2. After the final mechanical polishing step, the specimens were polished with oxide polishing suspension (OPS) for approximately 20 minutes without applying excessive force. To ensure uniform polishing during extended durations, the specimens were rotated 90° every two and a half minutes. The EBSD measurements were conducted using a NORDLYS NANO detector (Oxford Instruments, Great Britain) in the same SEM with a 75 µm aperture, an accelerating voltage of 20 kV, and a working distance of 17 mm. The step size of the measurements varied between 50 nm – 100 nm, depending on the material and purpose of the measurements. Post-processing of the EBSD data was carried out with the MATLAB (MathWorks Inc., USA) toolbox MTEX

[105]. Low-angle grain boundaries were defined by a misorientation angle $5° \leq \theta \leq 15°$, while high-angle grain boundaries were defined as $\theta > 15°$.

To estimate the area fraction of the MA islands in CFB microstructures, unindexed pixels in EBSD maps were used as indicators. The quality of the Kikuchi patterns, and thus the phase detection, is influenced by various microstructural factors such as dislocation density, grain boundaries, and triple points, which can disrupt the crystal lattice. These disruptions lead to a reduction in image quality (IQ) and result in unindexed pixels, where no phase can be identified. CFB microstructures generated under isothermal conditions typically contain freshly transformed MA islands (section 1.2.2) formed during subsequent cooling. Since fresh martensite has a significantly higher dislocation density compared to α_B, the IQ of these two phases differs noticeably. In particular, the high dislocation density in MA regions reduces the quality of the Kikuchi patterns, causing a decrease in IQ and a higher possibility of unindexed pixels in the EBSD map. As the MA islands tend to form in blocky morphology, the unindexed pixels in the EBSD map appear as distinct clusters, reflecting the characteristic morphology of the MA islands. **Figure 8**a shows the morphology of the MA islands in an SEM image, while **Figure 8**b displays the clusters of unindexed pixels in the EBSD phase map (same CFB), illustrating their spatial correlation.

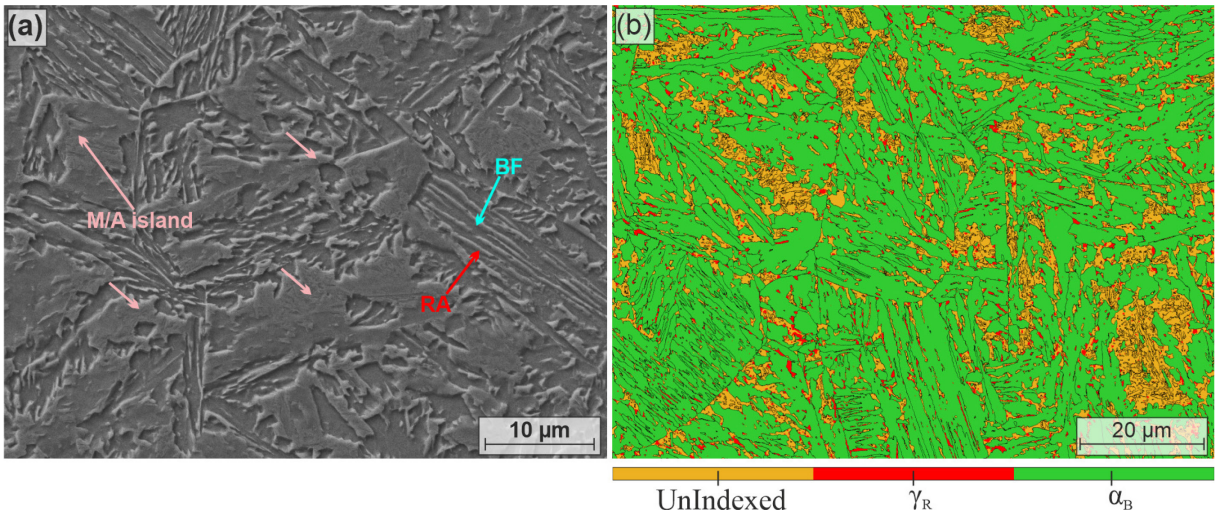

Figure 8. (a) SEM image and (b) EBSD phase map of a CFB microstructure.

3.5. Fatigue testing

For fatigue tests, cylindrical fatigue specimens with the smallest gauge diameter of 4 mm and a total length of 107 mm were machined longitudinally from the billets. The surface of the specimens was mechanically polished with diamond paste down to 1 µm to increase the surface quality. The tests were performed on a RUMUL GIGAFORE 50 (Russenberger Prüfmachinen

AG, Switzerland) resonant testing machine with a testing frequency of 1 kHz and a stress ratio of R = -1.

For the load increase test (LIT), a single specimen was tested for each material condition. The tests were initiated at a predefined stress amplitude and maintained for 10^6 cycles. After each 10^6-cycle interval, the test was paused, and the stress amplitude was increased by 10 MPa. This procedure was repeated until the fracture. In order to estimate the fatigue limit of the studied steels, the surface temperature of the specimen was monitored using a thermocouple during the tests, and no external cooling was applied. The stress amplitude at which a significant temperature rise occurs was recorded and taken as an approximate indication of the material's fatigue limit. A graphical representation of this procedure is shown in **Figure 9a**.

For staircase testing, 8 to 10 specimens were used for each material condition. The test limit was defined as 10^7 cycles. Specimens that failed before reaching this limit were classified as failures, while those that endured 10^7 cycles were considered runouts. Following each test, the stress amplitude was adjusted by ± 5 MPa, decreased in the case of failure, and increased in the case of runout. The test procedure is schematically shown in **Figure 9b**. During testing, specimens were air-cooled to avoid heating effects. The average fatigue limit was calculated using the Dixon-Mood equation [106], according to the following equation:

$$\mu = S_0 + \Delta S \left(\frac{\sum_{i=0}^{i_{max}} i n_i}{\sum_{i=0}^{i_{max}} n_i} \mp 0.5 \right) \quad (1)$$

In this equation, S_0 is the minimum stress amplitude corresponding to the less frequent outcome, either failure or survival. ΔS represents the step size, and the parameter i is an integer indicating the stress amplitude level. In this context, i_{max} refers to the highest stress amplitude level reached during the staircase procedure, and n_i is the number of specimens associated with the less frequent outcome at the stress level i. If failures are more frequent, $i = 0$ corresponds to the lowest stress amplitude level at which a specimen survives. Conversely, if survivals are more frequent, $i = 0$ marks the lowest stress amplitude level at which a specimen fails. The positive sign (+) in Eq. (1) is used when the failure events are more frequent, whereas the negative sign (-) is applied when survival events are more frequent. In cases where the failures and survivals occur in equal numbers, both calculations yield the same result.

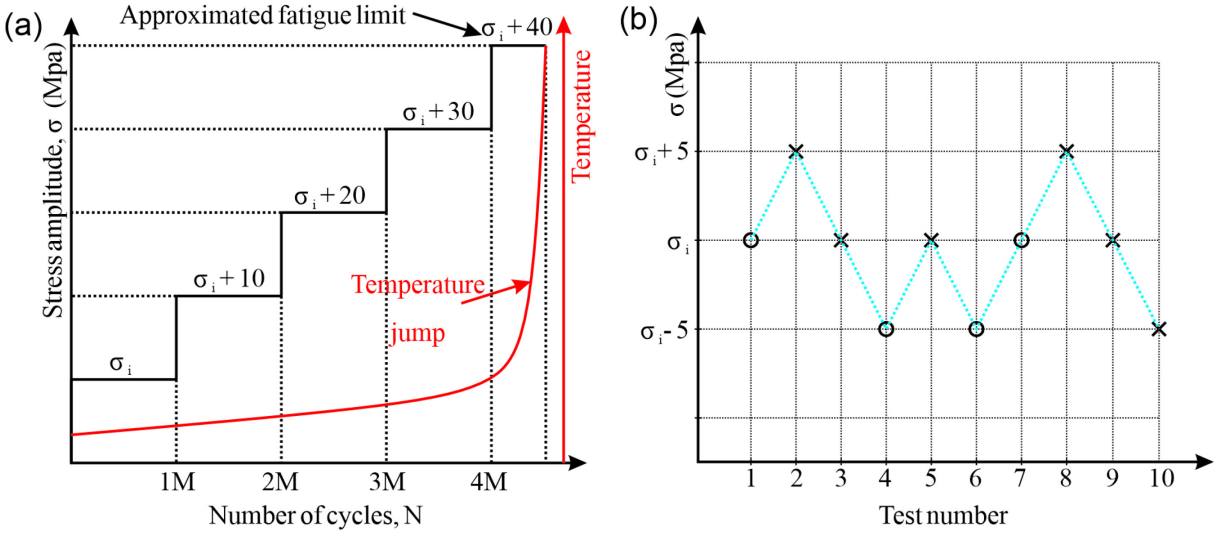

Figure 9. Graphical representation of (a) load increase test procedure and (b) staircase testing procedure.

4. Publication I

Effects of Silicon and Aluminum Alloying on Phase Transformation and Microstructure Evolution in Fe–0.2C–2.5Mn Steel: Insights from Continuous–Cooling–Transformation and Time–Temperature–Transformation Diagrams

O. Gulbay, A. Gramlich, U. Krupp

Steel Research International (2024)

DOI: 10.1002/srin.202400159

Chapter 4 highlights the influence of Si and Al on the bainitic phase transformation behavior and microstructure evolution in a Fe–0.2C–2.5Mn steel. The assessment of phase transformation behavior was supported by experimental determination of CCT and TTT diagrams via dilatometry. The microstructural investigations were performed using LOM and SEM, while XRD was used for phase identification. Additionally, a linear empirical formula was proposed to calculate the martensite start temperature. The main findings are summarized below:

- Al has a stronger influence on promoting the formation of ferritic microstructures compared to Si. Increased prior austenite grain size, resulting from Al alloying, promotes the formation of Widmanstätten structures during continuous cooling at higher cooling rates.
- Si slows down bainite transformation kinetics by stabilizing austenite through carbon enrichment, as a consequence of suppressed carbide precipitation, and strengthening of austenite via solid solution hardening. Although Al has similar effects, it reduces the incubation time for bainite transformation due to an increased driving force that outweighs the retarding effects.
- Compared to Si, Al promotes a finer CFB microstructure along with film-like γ_R morphology in isothermal heat treatment conditions. This is associated with increased α_B formation and improved carbon enrichment into the surrounding austenite, thereby improving γ_R and suppressing MA island formation.
- The proposed M_s formula enhances the accuracy between experimental and calculated M_s values.

RESEARCH ARTICLE

Editor's Choice

steel research international

www.steel-research.de

Effects of Silicon and Aluminum Alloying on Phase Transformation and Microstructure Evolution in Fe–0.2C–2.5Mn Steel: Insights from Continuous–Cooling–Transformation and Time–Temperature–Transformation Diagrams

Oguz Gulbay, Alexander Gramlich, and Ulrich Krupp*

The impact of silicon and aluminum on phase transformation behavior, particularly bainite, and microstructure evolution in Fe–0.2C–2.5Mn steel are presented. Continuous–cooling–transformation (CCT) and time–temperature–transformation (TTT) diagrams are determined experimentally. An aluminum extended empirical formula is introduced to estimate the martensite start temperature (M_s) with a thorough assessment of existing formulae. Results show that aluminum significantly increases M_s and has a stronger influence on promoting ferritic microstructures than silicon. During continuous cooling, alongside bainite, formation of Widmanstätten structures is induced in aluminum-alloyed steel at higher cooling rates due to increased prior austenite grain size. Silicon decelerates bainite transformation kinetics by enhancing austenite's chemical stability through carbon enrichment via preventing carbide precipitation and by strengthening austenite against displacive phase transformation via solid solution hardening. Although aluminum has similar effects, incubation time is shortened during isothermal treatment because of the increased driving force, which overcompensates for the retardation effects. A finer carbide-free bainitic microstructure is achieved in aluminum-alloyed steel with more pronounced film-like retained austenite (RA) formation and superior carbon enrichment, improving RA stability and suppressing martensite–austenite island formation. Finally, with the proposed formula, an accurate approximation to experimental M_s is accomplished.

1. Introduction

In recent years, the development of steel with superior properties has become crucial to increase the longevity and reliability of engineering components not only to produce better products but also to improve the circularity of the steel industry.[1] For this purpose, bainitic steels have attracted significant research attention to fulfill these requirements due to their promising properties in combination with their low-cost alloying and production concepts.[2–4] Variations in chemical composition and processing parameters substantially influence the microstructure and the morphology of the microstructural constituents of bainite, which affects the performance of the material considerably. If there is no kinetic hindrance, the excessive C that is rejected from bainitic ferrite (BF) precipitates as cementite between BF plates during bainitic transformation. On the other hand, by the addition of Si and/or Al (>1 wt%), cementite formation in the microstructure can be retarded due to the low solubility of these elements in cementite. The carbon, which is rejected from the BF, enriches the surrounding austenite, increasing stability. Consequently, retained austenite (RA) can be introduced to the microstructure as a secondary phase. The existence of RA in the microstructure leads to the transformation-induced plasticity effect during plastic deformation, which enhances the overall performance of the material.[5–7]

Most commercial engineering steels are either slowly cooled down to room temperature after austenitization or quenched down to martensite, which is followed by tempering.[8] In the case of bainitic steels, isothermal heat treatments are often necessary to obtain more homogeneous microstructures and to avoid martensitic transformation. Therefore, temperature control after final deformation plays a significant role in obtaining the desired microstructures and optimal properties. For designing proper heat treatment strategies, knowledge about phase transformation is essential and often summarized in continuous–cooling–transformation

O. Gulbay, A. Gramlich, U. Krupp
Steel Institute
RWTH Aachen University
52072 Aachen, Germany
E-mail: oguz.guelbay@iehk.rwth-aachen.de

The ORCID identification number(s) for the author(s) of this article can be found under https://doi.org/10.1002/srin.202400159.

DOI: 10.1002/srin.202400159

ADVANCED SCIENCE NEWS
www.advancedsciencenews.com
steel research international
www.steel-research.de

(CCT) and time–temperature–transformation (TTT) diagrams. Especially for the bainitic phase, the importance of transformation diagrams becomes even more prominent because of its complexity as a result of midrange transformation temperatures between pearlite/ferrite and martensite. However, phase transformation temperatures, kinetics, and characteristics can be highly influenced by different alloying elements. For instance, the critical cooling rate might show considerable differences,[9] leading to necessary heat treatment adjustments to obtain bainitic microstructure during continuous cooling. Martensite start temperature (M_s) can largely differ depending on the chemical composition,[10] which subsequently changes bainite transformation temperatures and phase transformation ranges. Concerning this, the M_s of materials also has a significant importance to be able to design accurate heat treatment strategies. It can be determined via experimental techniques such as dilatometry. Besides, many empirical equations have been developed over the years to predict the M_s of the materials to reduce material consumption, time, and costs.[11–22]

A study on bainite transformation is attractive not only from a fundamental perspective but also because of its practical significance. Thus, it is worthwhile to conduct an elaborative study to investigate the effect of different alloying elements on phase transformation characteristics. In this study, the influence of Si and Al on phase transformation behavior, especially bainite, was investigated. The CCT and TTT diagrams were experimentally determined to assess the phase transformation characteristics along with microstructural investigations. Additionally, an empirical formula was proposed to predict M_s with Al taken into account. The proposed formula was evaluated and compared with the numerous empirical equations in the literature.

2. Experimental Section

Three steel ingots (80 kg) with nominal compositions of Fe–0.2C–2.5Mn, Fe–0.2C–2.5Mn–1.5Si, and Fe–0.2C–2.5Mn–1.5Al (wt%) were produced in a laboratory-scale vacuum induction furnace. The ingots of $140 \times 140\,mm^2$ were homogenized at 1200 °C and forged down to billets of $60 \times 60\,mm^2$. Subsequently, another homogenization process at 1200 °C for 5 h was performed, which was followed by furnace cooling. The measured chemical compositions of the studied alloys are given in **Table 1**. Optical emission spectroscopy was employed to determine the chemical compositions, while carbon was determined with combustion analysis. The addition of 1.5 wt% Si in the second alloy and 1.5 wt% Al in the third alloy was aimed to prevent cementite precipitation during bainitic transformation and to examine the impact of these alloying elements on the phase transformation behavior. Consequently, this chemical composition concept was adopted to generate carbide-bearing bainite (CBB) for the first alloy and carbide-free bainite (CFB) for the second and third alloys. Accordingly, the first alloy was denoted as CBB, while the second and third alloys were labeled as CFB-Si and CFB-Al, concerning the cementite-suppressing alloying elements Si and Al, respectively.

Dilatometry was used to determine phase transformation temperatures (A_{c1}, A_{c3}, B_s, and M_s) as well as to characterize the transformation behavior during heat treatments. For the experiments, a DIL 805A/D (TA instruments, Germany) dilatometer and rectangular specimens ($4.0 \times 7.0 \times 1.4\,mm^3$) were used. First, the A_{c1} and A_{c3} were determined using a heating rate of $0.05\,K\,s^{-1}$. Second, CCT diagrams were determined by performing 12 experiments per alloy. The heating rate was set to $3.33\,K\,s^{-1}$, while the austenitization temperature was selected as $A_{c3} + 60$ K for 600 s to ensure fully austenitic microstructures. After austenitization, the specimens were continuously cooled to room temperature with various cooling rates. The M_s of the materials was determined from the cooling curves that showed only martensitic transformation and the B_s was established from the cooling curves that exhibited no prior phase transformation to bainitic transformation in CCT diagrams. The average of these values was considered as transformation temperatures. Third, to determine the TTT diagrams partially (bainitic transformation regions), after the same austenitization conditions, the specimens were cooled down to various temperatures above the M_s and held for 30 min to ensure complete phase transformation.

For light optical microscopy (LOM) and scanning electron microscopy (SEM) investigations, the surface of the specimens was prepared by mechanical grinding up to 1200 SiC grit paper followed by polishing with 6 and 1 µm diamond paste. Subsequently, the specimens were etched with 3% HNO_3 (Nital). SEM investigations were completed via field-emission gun Zeiss Sigma SEM (Carl Zeiss Microscopy GmbH, Germany) with a 30 µm aperture, an accelerating voltage of 15 kV, and a working distance of 9 mm for the secondary-electron detector. Quantitative X-ray diffraction (XRD) analysis was used to determine the RA fractions of CFB alloys. XRD patterns were acquired using a Stresstech diffractometer (Cr source) with a voltage of 30 kV and a current of 8 mA. The hardness of the dilatometer specimens was determined using Vickers 30 (HV30) indentation with a holding time of 15 s. The average of three measurements was considered as a hardness value for each specimen. The width of RA films and BF plates in CFB alloys was measured via ImageJ software and the average of ≈300 measurements from multiple SEM images was considered as the width.

3. Results

3.1. Continuous Cooling

The austenitization behavior of the studied alloys during continuous heating was described by the temperatures A_{c1} and A_{c3},

Table 1. Chemical composition of the studied alloys in wt%.

Alloy	C	Mn	Si	Al	P	S	Cr	Mo
CBB	0.18	2.48	0.01	0.002	0.003	0.002	0.04	0.01
CFB-Si	0.19	2.38	1.48	0.003	0.003	0.003	0.04	0.01
CFB-Al	0.19	2.46	0.01	1.41	0.004	0.003	0.04	0.02

Table 2. Transformation temperatures determined via dilatometry [°C].

Alloy	A_{c1}	A_{c3}	B_s	M_s
CBB	687	825	580 ± 4	384 ± 3
CFB-Si	700	900	582 ± 2	374 ± 3
CFB-Al	720	984	620 ± 2	413 ± 2

ADVANCED SCIENCE NEWS
www.advancedsciencenews.com
steel research international
www.steel-research.de

which are shown in **Table 2**. The A_{c1} of the studied alloys was found to exist between 687 and 720 °C. In the case of A_{c3}, significantly different values were obtained. The A_{c3} of CBB was determined as 825 °C, which increased to 900 and 984 °C in CFB-Si and CFB-Al, respectively. The phase transformation behavior during continuous cooling of the studied alloys was characterized using CCT diagrams (**Figure 1**). Bainite start temperature (B_s) and M_s of the alloys were also extracted from dilatometer experiments (Table 2). The B_s of CBB and CFB-Si were very similar at ≈580 °C, while Al addition in CFB-Al increased the B_s significantly to 620 °C. The M_s of CBB was determined as 384 °C. It decreased slightly to 374 °C with Si addition in CFB-Si. Moreover, similar to the B_s, the M_s increased considerably in CFB-Al to 413 °C.

The CCT diagrams are shown in Figure 1, while the LOM images of selected cooling curves, numbered in each CCT diagram, revealed the microstructure evolution of the studied alloys (**Figure 2**). The CCT diagram of CBB shows that with reducing cooling rate, the microstructure evolved from martensite-to-bainitic microstructure (Figure 1a). It was also found that at lower cooling rates, it was possible to obtain a fully bainitic microstructure. Additionally, the fully bainitic region was also enlarged since diffusion-controlled phase transformations were barely detected at very slow cooling rates (displayed with dashed lines). Micrographs obtained from different cooling curves of CBB alloy support these findings as well. The micrograph obtained from the first selected curve of CBB alloy exhibits a fully martensitic microstructure (Figure 2a), while it was fully bainitic in the rest of the selected curves (Figure 2b,c).

It was revealed that the bainitic phase field shifted to the right with Si alloying in CFB-Si compared to CBB. In other words, Si alloying decreased the critical cooling rate for the initiation of the bainitic phase transformation and accordingly increased the phase fraction of martensite at lower cooling rates (Figure 1a,b). Unlike CBB, diffusion-controlled phase transformations were clearly observed in CFB-Si at slower cooling rates as displayed in Figure 1b. Only the martensitic phase was present in the micrograph of the first selected curve (Figure 2d). The second selected curve exhibited a combination of martensitic and bainitic microstructures (Figure 2e), while the third curve consisted of bainitic microstructure along with a small amount of pearlite and α-ferrite formed at the prior austenite grain boundaries (PAGB) as shown in Figure 2f.

The CCT diagram of CFB-Al uncovered that the window to obtain a fully martensitic structure in CFB-Al was smaller than in the other alloys (Figure 1c). Moreover, a more pronounced

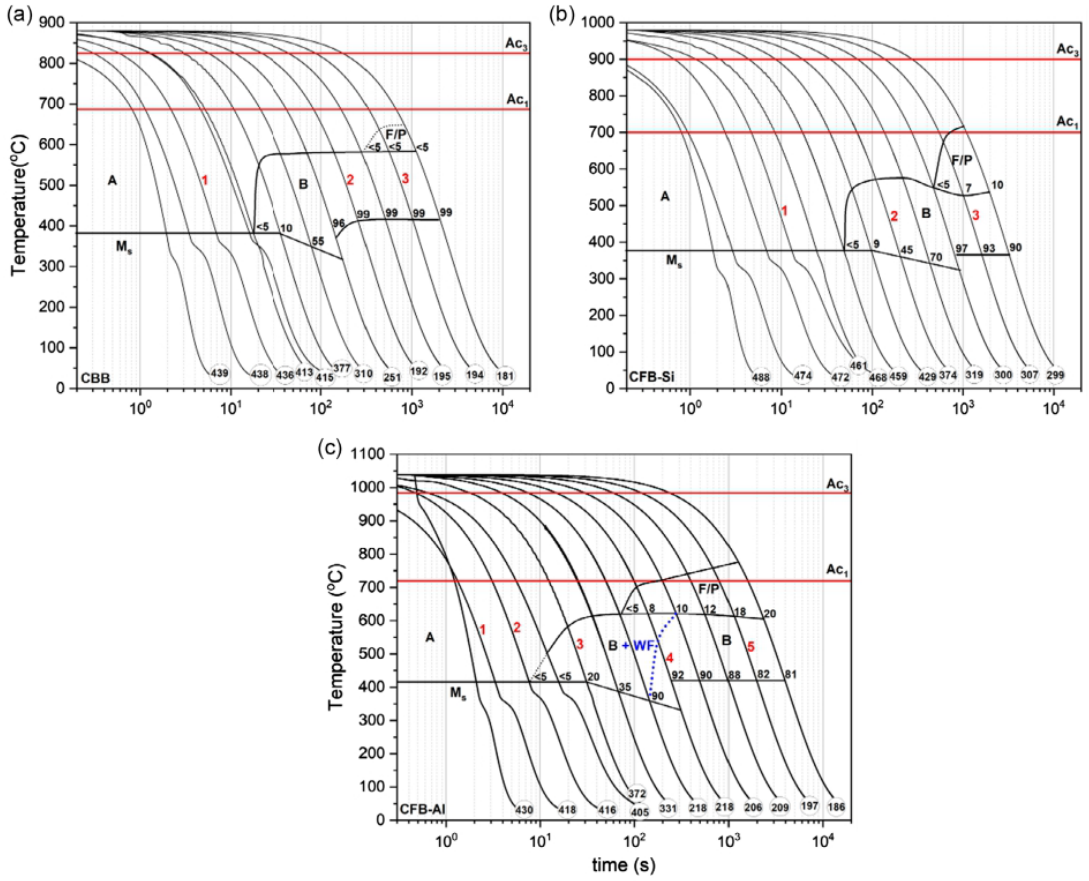

Figure 1. CCT diagrams of a) CBB, b) CFB-Si, and c) CFB-Al. Hardness is given in HV30.

ADVANCED SCIENCE NEWS
www.advancedsciencenews.com

steel research international
www.steel-research.de

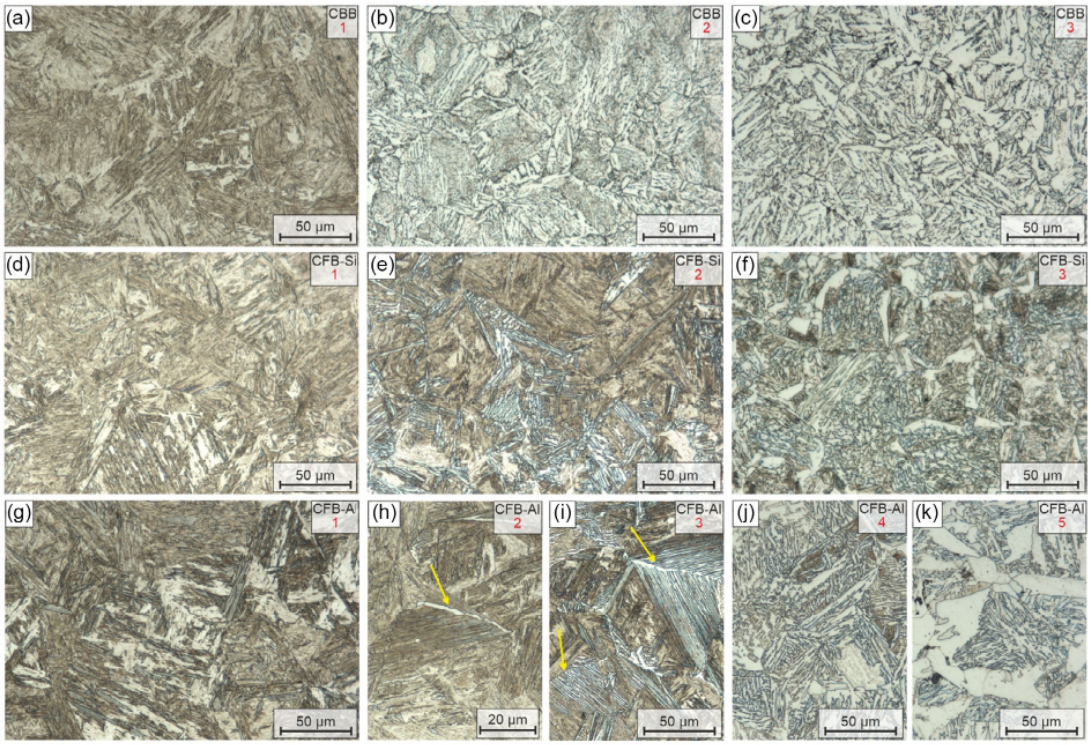

Figure 2. LOM images of the selected curves from the CCT diagram of each alloy in Figure 1. a–c) CBB, d–f) CFB-Si, and g–k) CFB-Al. Yellow arrows indicate Widmanstätten structures.

α-ferrite/pearlite formation was detected at slower cooling rates, which decreased the possibility of achieving a fully bainitic microstructure (Figure 1c). However, the microstructure evolution of CFB-Al displayed differences with decreasing cooling rate. Therefore, in CFB-Al, five cooling curves were selected to evaluate microstructure evolution. With a very high cooling rate, a fully martensitic microstructure was achieved from the first selected cooling curve (Figure 2g). At lower cooling rates, unlike the rest of the alloys, not only bainitic microstructure but also Widmanstätten ferrite (WF) was detected, which were developed as plates from PAGB in a well-defined orientation in an austenite grain. In curve two, allotriomorphic ferrite (AF) formation at PAGB and WF formation from AF can already be observed (Figure 2h). These formations were even clearer in the microstructure of curve three, as displayed in Figure 2i, where WF formation can be observed both from AF and directly from the PAGB (highlighted with yellow arrows). Furthermore, it was noticed that the formation of WF was suppressed at further lower cooling rates in curve four and a more pronounced bainitic microstructure was obtained (Figure 2j). The separation of WF formation in the CCT diagram of CFB-Al was indicated with the blue dotted line in Figure 1c. With a further decrease in cooling rate, in curve five, the microstructure consisted of bainite, a small amount of pearlite, and clear α-ferrite formation at PAGB (Figure 2k).

Furthermore, it is important to point out that while the bainitic microstructure of CBB exhibited cementite precipitates (Figure 2b), CFB-Si and CFB-Al alloys contained RA as a secondary phase in the bainitic microstructure instead of cementite, as intended (Figure 2e,j, respectively).

3.2. Isothermal Cooling

In order to investigate the phase transformation behavior during isothermal cooling conditions, the studied materials were held at different temperatures above M_s using a dilatometer. **Figure 3** displays the partial TTT diagrams of the alloys (only bainitic transformation), which were constructed by the determination of the beginning and end of the bainitic transformation from the obtained time–dilatation curves for each temperature. The maximum temperature at which only bainitic transformation occurred during isothermal treatment was 475 °C for CBB and CFB-Si (Figure 3a,b, respectively). In CFB-Al, the maximum temperature was shifted to 500 °C (Figure 3c), which is a similar behavior as it was observed in CCT diagrams. The phase transformation of all alloys started considerably fast (below 10 s). In the case of CFB-Si, initiation of the phase transformation was slightly shifted to longer times compared to CBB, while it was shifted back to even faster initiation times in the case of CFB-Al (Figure 3). Contrary to the initiation, the completion time of the bainitic transformation displayed larger differences. In the case of CBB, it varied between 100 and 165 s depending on the temperature, as shown in Figure 3a. With Si alloying, completion

ADVANCED SCIENCE NEWS
www.advancedsciencenews.com
steel research international
www.steel-research.de

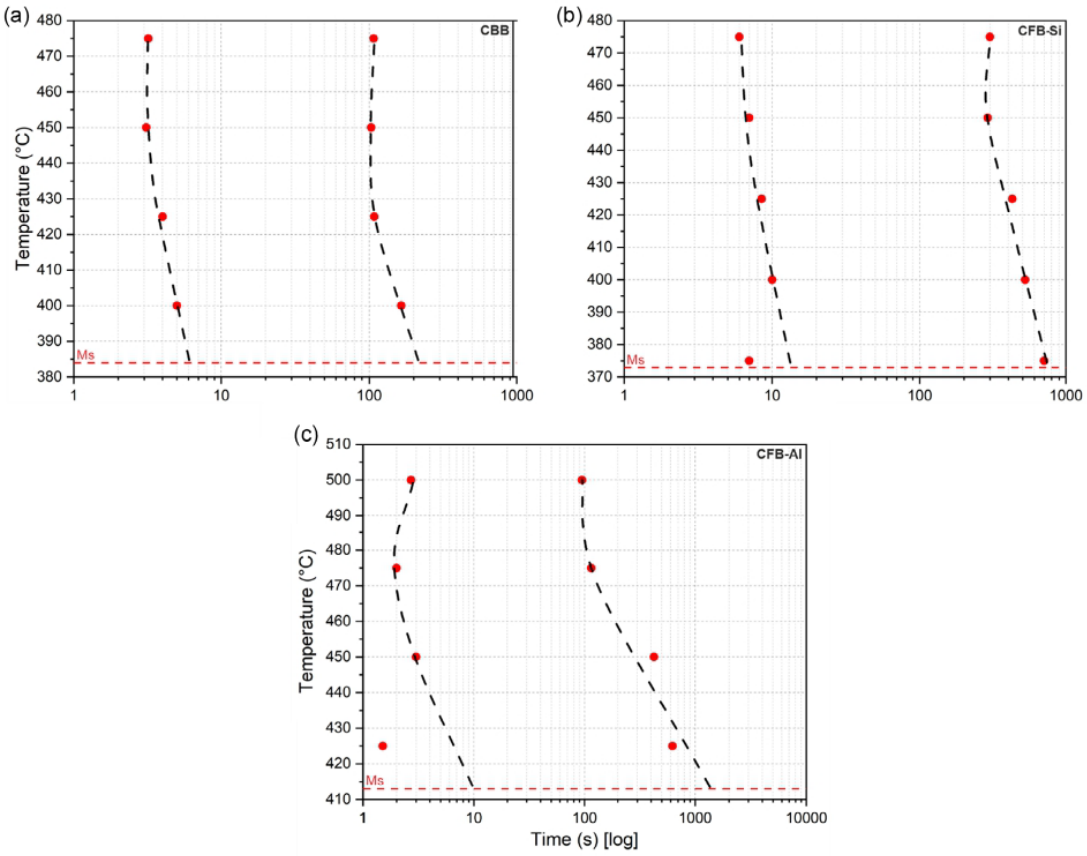

Figure 3. TTT diagrams of a) CBB, b) CFB-Si, and c) CFB-Al.

time increased up to 700 s at lower temperatures in CFB-Si (Figure 3b), while with Al alloying, it differed between 95 and 625 s in CFB-Al (Figure 3c). The summary of the beginning and end of bainite transformation times is given in **Table 3**. Additionally, it is worth mentioning that in CFB-Si and CFB-Al, at 375 and 425 °C, respectively, the initiation and completion times shifted to the left unexpectedly. This might be attributed to a possible martensitic transformation. Studies suggest that bainitic transformation accelerates with the existence of prior martensite in the microstructure due to an increased number of nucleation sites (martensite/austenite (M/A) interfaces) and dislocations introduced by martensite transformation.[23,24] When considered, the lowest isothermal heat treatment temperature for CFB-Si and CFB-Al is very close to their determined M_s values, which may exhibit differences in individual tests. In addition to that, in the case of minor segregation in the microstructure, especially Mn, martensite transformation kinetics can be influenced and induce local martensitic transformation during cooling. Therefore, it is possible that there was a slight martensitic transformation prior to bainite, which influenced the initiation of the bainite phase transformation.

Table 3. The summary of the beginning and end of bainite transformation times.

Heat treatment temperature [°C]	CBB		CFB-Si		CFB-Al	
	$t_{beginning}$ [s]	t_{end} [s]	$t_{beginning}$ [s]	t_{end} [s]	$t_{beginning}$ [s]	t_{end} [s]
375	–	–	7	699	–	–
400	5	165	10	520	–	–
425	4	107	8.5	425	1.5	625
450	3.1	103	7	290	3	425
475	3.2	108	6	300	2	115
500	–	–	–	–	2.7	95

Unexpected behavior was observed for the investigated alloys during the subsequent quenching after the isothermal holding, especially for CFB-Si and CFB-Al. In **Figure 4**a, dilatation curves of the experiments, which were conducted at 450 °C, are shown. As displayed, no subsequent transformation was observed in the dilatation curves of CBB and CFB-Al. Contrarily, CFB-Si exhibited a clear martensitic transformation during subsequent cooling at ≈100 °C, as highlighted in Figure 4a. The SEM investigations supported the dilatometric findings as well. As expected, CBB exhibited cementite as a secondary phase of

ADVANCED SCIENCE NEWS
www.advancedsciencenews.com
steel research international
www.steel-research.de

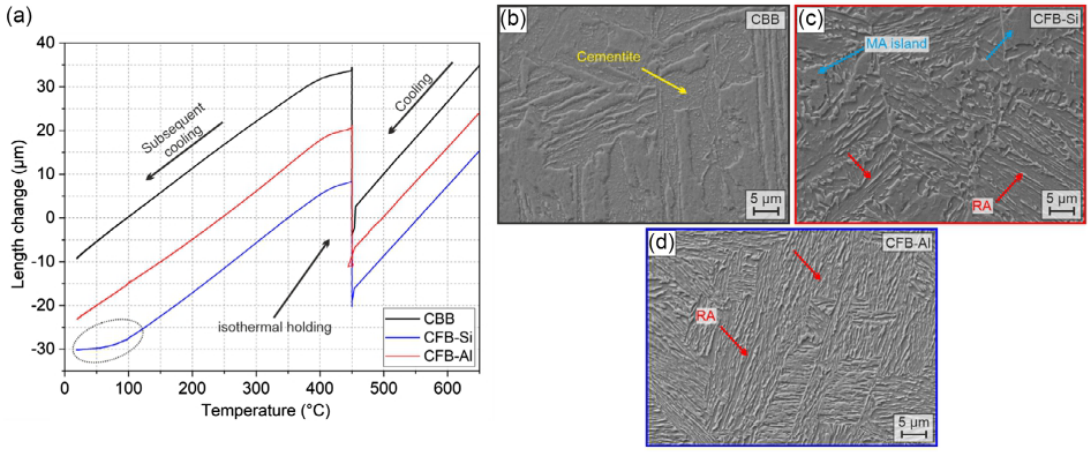

Figure 4. a) Dilatation curves of the studied alloys, which were obtained at 450 °C. SEM images of b) CBB, c) CFB-Si, and d) CFB Al.

bainitic microstructure (Figure 4b) with no RA and/or martensitic constituent. CFB-Al exhibited CFB microstructure consisting of fine RA films between BF plates (Figure 4d). In CFB-Si, in addition to RA films between BF plates, a clear MA island formation is observed, which is formed during subsequent cooling (Figure 4c). Furthermore, when investigating dilatation curves at different isothermal holding temperatures, the martensitic transformation became even more prominent when the isothermal temperature was higher (increased M_s) (Figure SA1a, Supporting Information). In the case of CFB-Al, only slight martensitic transformation was detected at 500 °C in the dilatation curves (Figure SA1b, Supporting Information).

XRD analysis revealed that the RA fractions of CFB-Si and CFB-Al after subsequent cooling were 4.7% and 5.3%, respectively. Although the volume fractions of RA of CFB alloys are similar in the final microstructure, their size and morphology exhibited differences. As shown in Figure 4c,d, a more refined CFB microstructure was achieved in CFB-Al compared to CFB-Si. Film-like RA morphology was more pronounced in CFB-Al, while a coarser CFB microstructure was obtained in CFB-Si along with large MA islands. **Figure 5** illustrates the average width of RA films and BF plates of CFB alloys. The average width of RA films was measured as 0.11 µm in CFB-Al, while it was 0.23 µm in CFB-Si. A similar trend was observed in the average width of BF plates. It was measured as 0.20 µm in CFB-Al, which increased to 0.26 µm in CFB-Si.

3.3. Comparison of Experimental and Calculated M_s

The alloying elements have a strong influence on M_s. In literature, a great number of empirical formulae are developed to estimate the M_s of steel alloy. In these formulae, the impact of each alloying element is taken into consideration significantly differently. Moreover, the majority of the empirical formulae are based on linear regression. In **Table 4**, an overview of linear formulae used in this study is displayed. Only the formulae containing Si and/or Al were preferred to calculate the M_s considering the effective alloying elements in the studied alloys

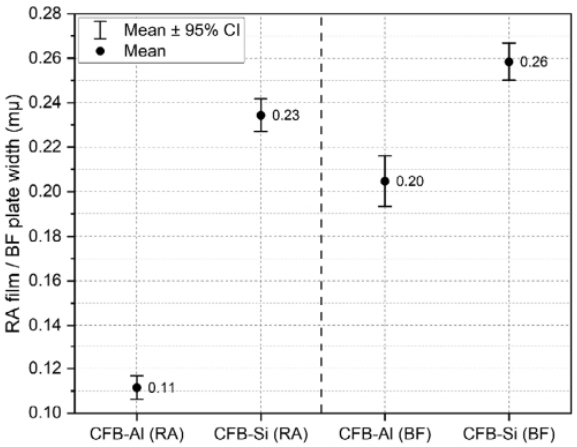

Figure 5. Mean width of RA films and BF plates in CFB-Al and CFB-Si alloys (450 °C) with 95% confidence index.

(except Andrews). It is important to point out that among 15 models, only four of them contained Al, while only two models included Si and Al together (highlighted as bold in Table 4).

Table 5 shows the M_s of the studied alloys determined via dilatometry along with calculated values via 15 linear formulae from Table 4. To show the accuracy of the formulae, root-mean-square deviation (RMSD) was calculated for each formula, as shown in Table 5. The calculated RMSD values for the studied alloys scattered in a very wide range between 8 and 58. Among all the models, eight of them displayed RMSD $\geq$ 20, while only five formulae exhibited RMSD $\leq$ 15. These results uncover the dependency of the calculated M_s on the used formulae. Additionally, results clearly showed that Al has a significant impact on M_s. However, Al was only included in four of these models (Table 4). When considered, only the model of Mahieu (containing both Si and Al) showed good M_s prediction with RMSD $<$ 10 for the

ADVANCED SCIENCE NEWS
www.advancedsciencenews.com

steel research international
www.steel-research.de

Table 4. Overview of formulae to calculate M_s based on linear regression models comparing the factors of different elements. Not all elements are included in the table. Complete equations are summarized in Table SA2, Supporting Information.

Model	C_0	C_C	C_{Mn}	C_{Si}	C_{Al}	C_{Cr}	C_{Ni}	C_{Mo}	C_B
Andrews[11]	539.0	−423.0	−30.4	–	–	−12.1	−17.7	−7.5	–
Capdevila et al.[12] (in K)	764.2	−302.6	−30.6	−14.5	–	−8.9	−16.6	2.4	–
Gramlich[13]	517.0	−423.0	−30.4	–	**37.0**	–	–	82.0	−700.0
Ishida[14]	545.0	−330.0	−23.0	**−7.0**	**2.0**	−14.0	−13.0	−5.0	–
Kung and Rayment[15]	539.0	−423.0	−30.4	−7.5	–	−12.1	−17.7	−7.5	–
Liu 1[16]	550.0	−361.0	−39.0	–	**30.0**	−20.0	−17.0	−5.0	–
Liu 2[16]	538.0	−317.0	−33.0	−11.0	–	−28.0	−17.0	−11.0	–
Mahieu[17]	539.0	−423.0	−30.4	**−7.5**	**30.0**	–	–	–	–
Nehrenberg[16,21,22]	499.0	−292.0	−32.4	−10.8	–	−22.0	−16.2	−10.8	–
Payson and Savage[16,21,22]	499.0	−308.0	−32.4	−10.8	–	−27.0	−16.2	−10.8	–
Rowland-Lylew[16,21,22]	499.0	−324.0	−32.4	−10.8	–	−27.0	−16.2	−10.8	–
Steven and Haynes[15,21]	561.0	−474.0	−33.0	−7.5	–	−17.0	−17.0	−21.0	–
Sverdlin and Ness[18]	520.0	−320.0	−50.0	−5.0	–	−30.0	−20.0	−20.0	–
Trzaska[19]	541.0	−401.0	−36.0	−10.5	–	−14.0	−18.0	−17.0	–
Wang[20]	545.0	−470.0	−37.7	−3.96	–	−21.5	–	38.9	–

Table 5. Overview of experimentally determined and calculated M_s of the three studied alloys (via 15 different linear models and optimized formula) with RMSD (for studied and further included alloys) and coefficient of determination R^2 (for further included alloys). Bold characters were used to highlight and compare the experimental values and measured values with the new formula.

Method	CBB [°C]	CFB-Si [°C]	CFB-Al [°C]	RMSD (studied alloys)	RMSD (all alloys)	R^2 (all alloys)
Experimental	**384**	**373**	**413**	–	–	–
Andrews	387	386	383	19	21	0.953
Capdevila et al.	360	339	358	40	25	0.936
Gramlich[13]	366	364	414	12	15	0.970
Ishida	428	417	428	37	65	0.976
Kung and Rayment	387	375	383	17	16	0.965
Liu 1	388	388	427	12	26	0.956
Liu 2	398	382	395	14	22	0.946
Mahieu[17]	387	375	426	8	20	0.983
Nehrenberg	365	350	363	34	23	0.934
Payson and Savage	362	346	360	37	26	0.945
Rowland-Lylew	359	343	357	40	28	0.950
Steven and Haynes	393	381	389	15	15	0.966
Sverdlin and Ness	337	332	335	58	73	0.878
Trzaska	379	363	376	23	19	0.949
Wang	366	359	362	32	26	0.958
Developed	**384**	**372**	**412**	**<1**	**8**	**0.990**

studied alloys. For further investigation, not only the three studied alloys but also further alloys with different chemical compositions were included from the literature. An additional 23 alloys with varying chemical compositions with different M_s were also analyzed.[13,25–27] The chemical composition and M_s of the additional alloys are given in Table SA1, Supporting Information. Furthermore, the RMSD and coefficient of determination (R^2) values are displayed in Table 5 for each formula, considering the additional alloys as well (26 alloys in total). It can be seen that the lowest obtained RMSD increased to 15 when the number of analyzed alloys increased to 26.

For the optimization of a new formula, the model from Steven and Haynes was selected (Equation (1)). Although RMSD was not the lowest for the three studied alloys, it was the lowest for the

ADVANCED SCIENCE NEWS
www.advancedsciencenews.com
steel research international
www.steel-research.de

26 alloys (Table 5). As shown in Equation (1), Al was not included in the formula. Additionally, when the experimental values were compared with calculated values via the formula Steven and Haynes, it was recognized that the majority of the calculated values were larger than the experimental values (lying on the left in **Figure 6**a). Therefore, the equation was found to be attractive for optimization to increase the accuracy of the M_s calculations. In the optimized formula (Equation (2)), besides slight changes, the initial parameter was reduced since most of the calculated values were higher than experimental values and Al was introduced with a positive factor based on the obtained results. Furthermore, boron was included with a negative factor as in the formula of Gramlich, which resulted in more accurate results considering literature alloys that contain boron. The RMSD for the studied alloys was below 1, which is nearly a perfect match (Table 5). When all the M_s data were included from the literature, the results show that the best fit was accomplished via the optimized formula by achieving the minimum RMSD and the maximum R^2 values (Table 5). The optimized formula was the only one that provided RMSD <10, while the original formula from Steven and Haynes was 15. In addition to that, the modified formula exhibited the highest R^2 value by 0.990 (Table 5). Figure 6b also depicts the correlation between the experimental M_s values and calculated M_s values via the optimized formula showing a better fit compared to Steven and Haynes (Figure 6a).

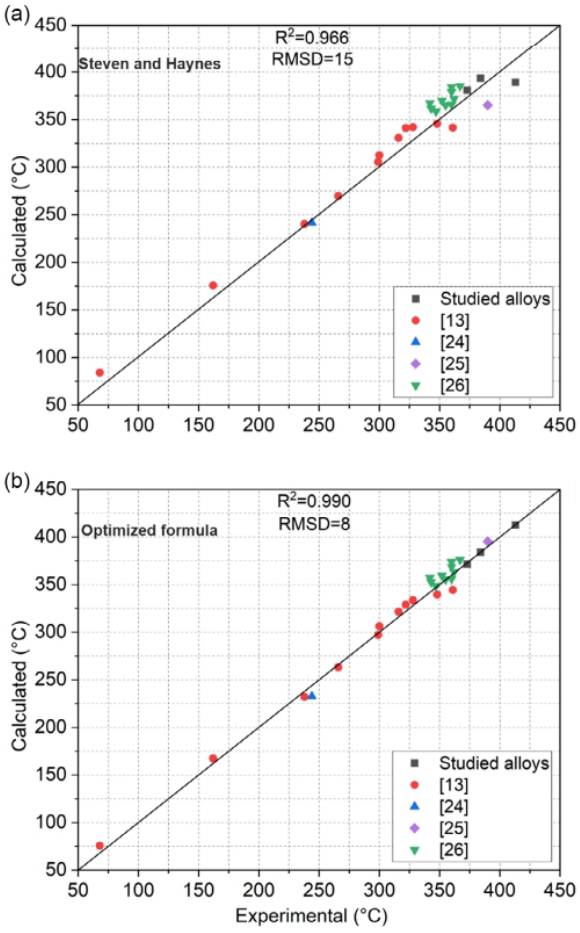

Figure 6. Comparison of experimental and calculated M_s a) via Steven and Haynes and b) via optimized formula.

$$M_s = 561 - 474 \times w_C - 33 \times w_{Mn} - 7.5 \times w_{Si} - 17 \times w_{Ni} - 17 \times w_{Cr} - 21 \times w_{Mo} + 10 \times w_{Co} \quad (1)$$

$$M_s = 552 - 474 \times w_C - 33 \times w_{Mn} - 7.5 \times w_{Si} + 23 \times w_{Al} - 17 \times w_{Ni} - 17 \times w_{Cr} - 10 \times w_{Mo} - 700 \times w_B \quad (2)$$

4. Discussion

In the context of the increasing circularity of the steel industry, lean alloying concepts will gain additional attention in the upcoming years. The Fe–Mn–C–Si–(Al) system is especially promising for the circular economy, as these groups of steels combine light-weighting potential as well as the option of integrated and shorter heat treatment routes. While a large variety of properties can be achieved in this system, none of the alloying elements tends to accumulate during recycling (like Cu or Mo).[28,29] Therefore, these steels can be considered a good feedstock for the production of recycling steels. Only by holistically addressing the material development, the respective environmental impact of high-strength steels can be reduced.[30]

In order to broaden the knowledge about these promising steel grades, the effects of Si and Al on phase transformation temperatures, CCT and TTT diagrams, bainitic phase transformation characteristics, and microstructure evolution were investigated. It was observed that Si and Al alloying increased the A_{c3} and enlarged the intercritical area of the corresponding alloys due to the ferrite-stabilizing effect of these elements.[31,32] Moreover, it is known that Al is an even stronger ferrite-forming element than Si.[33–35] As a result of this, CFB-Al not only exhibited the highest A_{c3} among the studied alloys but also the largest intercritical area, which could be useful to improve process stability during the continuous annealing process.[32]

Si alloying decreased M_s slightly, while Al alloying increased M_s significantly. The driving force for diffusionless transformation was calculated for each alloy (between 300 and 500 °C) via Bhadeshia's model,[36] as illustrated in **Figure 7**a. It can be seen that the martensitic transformations occur when similar driving forces are achieved, which is in the range from −1061 to −1142 J mol^{-1} (highlighted in Figure 7a). Moreover, at the same temperature, a slightly lower driving force is achieved with Si alloying, while a significant increase is obtained with Al alloying. In other words, the driving force for the martensitic transformation was achieved at higher temperatures in CFB-Al, while it was only possible at lower temperatures in CFB-Si, which explains the observed differences in M_s due to Si and Al alloying.

In addition to the investigations, a new linear formula was proposed to estimate the M_s of steel alloys due to the inaccuracy of the existing formulae in literature as the majority of them do not contain Al (Table 4). On the other hand, it was shown that Al has a strong influence on M_s. Therefore, for the cause of proper

ADVANCED SCIENCE NEWS
www.advancedsciencenews.com
steel research international
www.steel-research.de

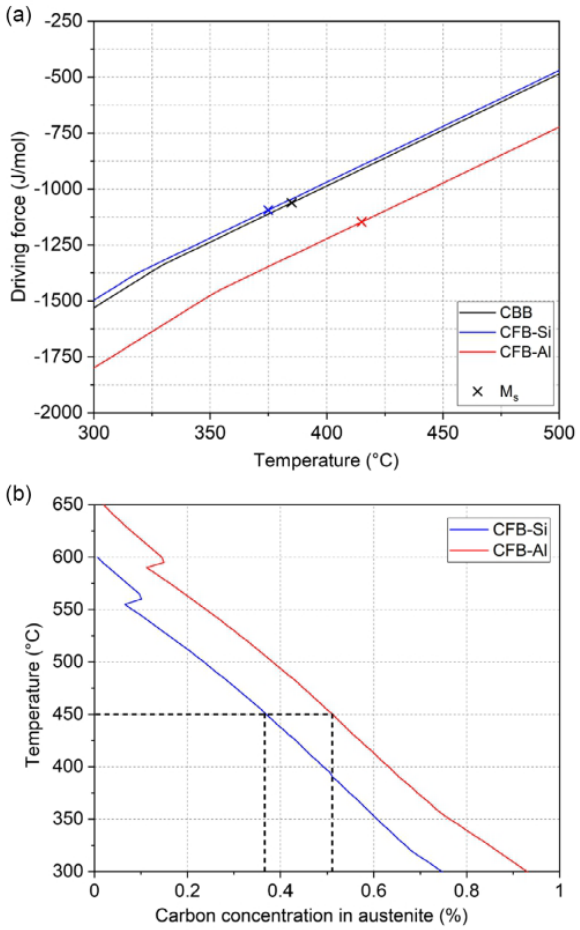

Figure 7. a) Driving force for the diffusionless transformation of the studied alloys. b) T_0 curves of CFB-Si and CFB-Al. The strain energy of BF was taken into account by 400 J mol^{-1}.

process design, it is important to consider Al to calculate M_s. It can be observed that the proposed formula provided more accurate results with less deviation compared to other models by showing the lowest RMSD = 8 and the higher $R^2 = 0.990$ (Table 5).

Regarding the impact of Si alloying on phase transformation, it was demonstrated that Si alloying in CFB-Si delayed the bainite transformation during continuous cooling as well as during isothermal heat treatment compared to CBB. In the CCT diagram, Si alloying decreased the critical cooling rate for the initiation of the bainitic transformation (Figure 1a,b). This is consistent with the findings in the TTT diagram, where Si alloying prolonged the incubation period for bainitic transformation (Figure 3a,b). These can be attributed to the fact that Si is a very strong carbide inhibitor, which indirectly improves the chemical stability of austenite against phase transformation. Because of this hindrance, carbon remains in austenite unlike in CBB, which also delays the formation of carbon-depleted zones for the initiation of bainite transformation. Thus, the transformation kinetics slow down.[37] Additionally, it was stated that the solid solution hardening effect of Si decelerates the bainite transformation kinetics by strengthening the austenite matrix against the shape change occurring during displacive bainite transformation.[38] Therefore, with Si alloying, the amount of strain energy that must be overcome increases, which results in slower phase transformation kinetics. Furthermore, at lower cooling rates, a clear formation of pearlite and α-ferrite was detected in CFB-Si as opposed to CBB (Figure 2c,f, respectively). Si as a ferrite stabilizer promotes the formation of α-ferrite by increasing the driving force for the transformation of austenite to ferrite. Thus, the formation of diffusive phases in CFB-Si shifted to the left and higher temperatures in CCT diagram compared to CBB (Figure 1a,b).

In the case of CFB-Al, the incubation period in the TTT diagram shifted slightly to shorter times in contrast to CFB-Si (Figure 3c) although Al has the same effect as Si to hinder carbide precipitation. It was demonstrated in the literature that Al alloying increases the free energy change ($|\Delta G^{\gamma\alpha}|$) during bainitic transformation.[35,39] As a result of this increase in driving force via Al alloying, the retardation effect due to enhanced chemical stability because of suppressed carbide precipitation can be overcompensated.[40] Regarding the continuous cooling behavior of CFB-Al, the situation seems to be more complicated. In the microstructure examination, not only bainitic structures but also Widmanstätten structures were detected at high cooling rates, which was not observed in isothermally treated specimens. Furthermore, with a decreasing cooling rate, prominent microstructure changed from Widmanstätten structures to bainite and diffusive-controlled phases. Two types of Widmanstätten structures were identified, which were formed either directly from PAGBs (primary WF) or from AF formed at PAGBs (secondary WF) as displayed in Figure 2i. These findings fit the characteristics of WF that were reported in the literature.[41,42] It was demonstrated that cooling rate and PAG size are determining factors for the formation of Widmanstätten structures. Higher cooling rates and increased PAG size favor the formation of Widmanstätten structures.[41,43,44] This is strongly supported by the obtained results during continuous cooling of CFB-Al. As displayed in **Figure 8**, CFB-Al exhibited the largest PAG size (with grains exceeding 100 µm) as a result of higher austenitization temperatures due to increased A_{c3}. Li et al.[45] also established that Al alloying can substantially accelerate austenite grain growth by increasing the grain growth activation energy of austenite.

It can be clearly concluded that, directly or indirectly, Al alloying has a stronger influence on promoting the formation of ferritic microstructures compared to Si. For instance, since Al is a stronger ferrite stabilizer, A_{c3} increases significantly. Thus, the formation of α-ferrite was shifted to higher temperatures and to faster times in the CCT diagram (Figure 1c). Because of the same reason, the austenitization of CFB-Al shifted to higher temperatures, which increased the PAG size. This indirectly contributed to the conditions to form Widmanstätten structures during continuous cooling in addition to the increased driving force.

During isothermal treatments, it was illustrated that the completion time of the bainitic transformation in CFB alloys was longer than in CBB alloy (Figure 3). The major difference between CBB and CFB alloys is the type and amount of

ADVANCED SCIENCE NEWS
www.advancedsciencenews.com
steel research international
www.steel-research.de

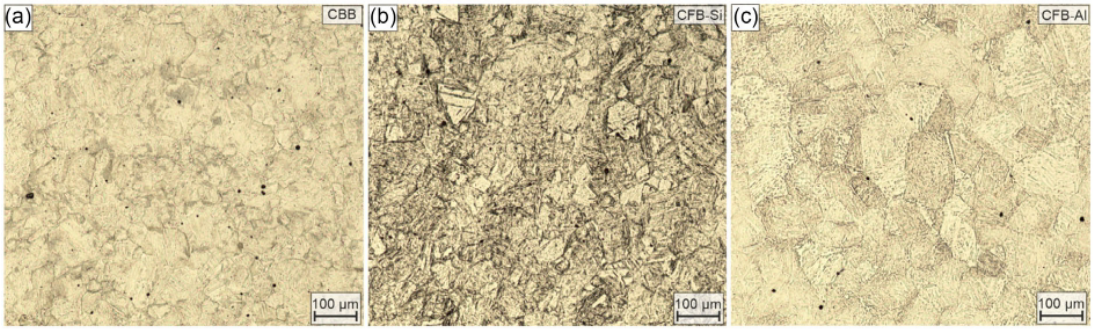

Figure 8. Prior austenite grains of a) CBB, b) CFB-Si, and c) CFB-Al (treated with picric acid).

secondary phases. In CBB, cementite precipitated as a secondary phase, while in CFB alloys, RA was formed. It is known that cementite precipitation can be retarded by the addition of Si/Al. This is only valid when cementite is forced to inherit the silicon in the parent phase from which it precipitates. Si has a low solubility in cementite and when cementite is forced to form at lower temperatures under paraequilibrium conditions (e.g., bainite transformation temperatures), where the atomic mobility is limited, Si is trapped in cementite during its growth. As a result of this, a significant reduction in free energy change of the reaction occurs, which slows down the precipitation kinetics, thus retarding the precipitation.[4,46] Similar effects have been reported for Al; however, the data for this alloying is scarce.[4] Therefore, as a result of Si and Al alloying, cementite precipitation is ceased and, the excessive carbon, which is rejected from BF, enriches the surrounding austenite in CFB alloys.[46,47] This leads to the thermal stabilization of austenite during bainitic transformation, which results in RA in the microstructure at room temperature. As mentioned, increased Si content lowers the bainitic transformation kinetics through the prevention of carbide formation and solid solution hardening effect of Si.[38] The solid solution hardening of Si strengthens the austenite phase against displacive bainite transformation by increasing the amount of generated strain energy to overcome and thus bainitic transformation kinetics is slowed down. From another perspective, when considering the influence of the strength of austenite during phase transformation, not only Si and Al but also carbon should be considered. It is well known that carbon increases the yield strength of austenite. Since carbon is partitioned into austenite in CFB alloys during bainitic transformation, it should have an impact on the strength of the austenite phase and consequently on the phase transformation kinetics. Moreover, Al does not influence the strength of austenite as much as Si.[35] Therefore, carbon may be the effective factor that increases the strength of the austenite of CFB-Al, which influences the phase transformation kinetics. As suggested in the incomplete-reaction phenomenon (T_0 concept), the diffusionless transformation of bainite is only possible when the carbon concentration in austenite is below a critical threshold.[48] As mentioned before, $|\Delta G^{\gamma\alpha}|$ increases with Al alloying during bainitic transformation.[35,39] This was also supported by the thermodynamic calculations as shown in Figure 7a, which indicates that in CFB-Al, more BF can be formed, and correlatively, more carbon can be partitioned into the surrounding austenite at the same transformation temperature compared to CFB-Si. In order to support that, T_0 curves (temperature vs. carbon concentration) of CFB-Si and CFB-Al are illustrated in Figure 7b, which were also acquired via the thermodynamical calculations using Bhadeshia's model.[36] It is clear that the maximum carbon solubility of austenite is higher in CFB-Al at the same temperature during bainitic transformation. This shows that Al alloying promotes the BF formation during bainitic transformation along with increased carbon enrichment in RA, which will increase the strength of austenite, and hence, it will contribute to slowing down the kinetics to complete the phase transformation.

The alloying of Si and Al also influences austenite stability and thus martensitic transformation. It was observed that CFB-Si exhibited prominently more martensitic transformation during subsequent cooling after isothermal heat treatment temperatures, which was identified both via dilatometry and SEM investigations (Figure 4). This indicates that the thermal stability of RA in CFB alloys exhibits differences depending on the alloying elements, pointing out to the carbon concentration of CFB alloys, which is illustrated in the T_0 curve (Figure 7b). Thermodynamic calculations showed that CFB-Al can accommodate more carbon in the untransformed austenite and more BF can be formed due to an increase in $|\Delta G^{\gamma\alpha}|$ during the phase transformation. As a result, CFB-Al displayed superior RA stability compared to CFB-Si, which was reflected with no dilatation signal in the dilatation curve of CFB-Al and fewer martensitic constituents in SEM images (Figure 4). Furthermore, compared to CFB-Si, the diffusionless bainite transformation can proceed further in CFB-Al. Thus, due to less BF formation and less carbon partitioning in CFB-Si, more unstable blocky RA remained, which subsequently led to martensitic transformation and formation of MA islands in the microstructure (Figure 4). The XRD results supported these findings as well. Based on thermodynamic calculations, the volume fraction of RA in CFB-Si was expected to be higher right after the isothermal holding due to less BF formation. However, in the final microstructure, XRD analysis revealed a higher RA fraction of CFB-Al. This also points out that the RA in CFB-Si has poor thermal stability, which resulted in martensitic transformation during subsequent cooling. Correspondingly, the measured RA fraction was decreased in the final microstructure.

ADVANCED SCIENCE NEWS
www.advancedsciencenews.com

steel research international
www.steel-research.de

Regarding the size and morphology of the bainitic constituents, CFB-Al exhibited finer microstructure and a more pronounced formation of film-like RA morphology compared to CFB-Si. Following the formation of the BF plate, a carbon-enriched zone develops due to carbon partitioning, and the carbon concentration in this zone decreases over a distance.[49] Therefore, based on the T_0 concept, if the ability of austenite to accommodate carbon is superior, the formation of the next BF can start at higher carbon concentrations at the austenite interface. Hence, in CFB-Al, the adjacent BF can thermodynamically be initiated from a smaller distance. A similar effect can also be achieved by reducing the isothermal transformation temperature.[49,50] This, in combination with a higher BF fraction, was inherited as a refined CFB microstructure and profound formation of film-like RA in CFB-Al occurred.

5. Conclusion

The influence of Si and Al on the bainitic phase transformation characteristics and microstructure evolution was investigated in a Fe–0.2C–2.5Mn steel. The phase transformation behavior was characterized by the determination of CCT and TTT diagrams. A linear empirical formula was proposed to calculate martensite start temperature and compared with a number of different formulae from the literature. The following conclusions can be drawn. 1) For the investigated steel, Al has a stronger influence on promoting the formation of ferritic microstructures in comparison to Si. Rivetingly, increased prior austenite grain size due to Al alloying induces the formation of Widmanstätten structures during continuous cooling at higher cooling rates. 2) Si alloying decelerates overall bainite transformation kinetics due to increased chemical stability of austenite against phase transformation as a result of carbon enrichment because of the prevention of carbide precipitation and by strengthening of austenite against displacive phase transformation via solid solution hardening. On the contrary, although Al has similar effects, Al alloying shortens the incubation time of bainite transformation during isothermal heat treatment due to increased driving force, which overcompensates the retardation effects. 3) In isothermal heat treatment, compared to Si, Al alloying promotes the formation of film-like RA and finer CFB structure. This is associated with increased BF formation and improved carbon enrichment into the surrounding austenite. Consequently, it enhances the RA stability, which reduces MA island formation. 3) The proposed new M_s formula significantly improves the compatibility of the experimental and calculated M_s values of materials.

Supporting Information

Supporting Information is available from the Wiley Online Library or from the author.

Acknowledgements

The authors would like to thank Michael Schillheim and Robert Gier for their technical assistance during the experimental phase of this study.
Open Access funding enabled and organized by Projekt DEAL.

Conflict of Interest

The authors declare no conflict of interest.

Data Availability Statement

The data that support the findings of this study are available from the corresponding author upon reasonable request.

Keywords

bainite, martensite start temperatures, microstructures, phase transformations, Widmanstätten ferrites

Received: February 24, 2024
Revised: August 6, 2024
Published online: August 25, 2024

[1] A. Gramlich, W. Hagedorn, K. Greiff, U. Krupp, *Adv. Eng. Mater.* **2023**, *25*, 2201931.
[2] C. Hofer, H. Leitner, F. Winkelhofer, H. Clemens, S. Primig, *Mater. Charact.* **2015**, *102*, 85.
[3] F. G. Caballero, S. Allain, J. Cornide, J. D. Puerta Velásquez, C. Garcia-Mateo, M. K. Miller, *Mater. Des.* **2013**, *49*, 667.
[4] H. K. D. H. Bhadeshia, *Bainite in Steels: Transformations, Microstructure and Properties*, 2nd ed., IOM Communications, London **2001**.
[5] C. Garcia-Mateo, F. G. Caballero, *Mater. Trans.* **2005**, *46*, 1839.
[6] C. Hofer, S. Primig, H. Clemens, F. Winkelhofer, R. Schnitzer, *Adv. Eng. Mater.* **2017**, *19*, 1600658.
[7] G. Gao, R. Liu, K. Wang, X. Gui, R. Misra, B. Bai, *Scr. Mater.* **2020**, *184*, 12.
[8] H. K. D. H. Bhadeshia, D. V. Edmonds, *Met. Sci.* **1983**, *17*, 411.
[9] D. V. Doane, *J. Heat Treat.* **1979**, *1*, 5.
[10] T. Cool, H. K. D. H. Bhadeshia, *Mater. Sci. Technol.* **1996**, *12*, 40.
[11] K. W. Andrews, *J. Iron Steel Inst.* **1965**, *203*, 721.
[12] C. Capdevila, F. G. Caballero, C. G. de Andrés, *ISIJ Int.* **2002**, *42*, 894.
[13] A. Gramlich, C. van der Linde, M. Ackermann, W. Bleck, *Results Mater.* **2020**, *8*, 100147.
[14] K. Ishida, *J. Alloys Compd.* **1995**, *220*, 126.
[15] C. Y. Kung, J. J. Rayment, *Metall. Trans. A* **1982**, *13*, 328.
[16] C. Liu, Z. Zhao, D. O. Northwood, Y. Liu, *J. Mater. Process. Technol.* **2001**, *113*, 556.
[17] J. Mahieu, B. C. de Cooman, J. Maki, *Metall. Mater. Trans. A* **2002**, *33*, 2573.
[18] *Steel Heat Treatment Handbook* (Eds: G. E. Totten, M. A. H. Howes), Dekker, New York, NY **1997**.
[19] J. Trzaska, *Arch. Metall. Mater.* **2016**, *61*, 981.
[20] J. Wang, P. J. van der Wolk, S. van der Zwaag, *Mater. Trans., JIM* **2000**, *41*, 761.
[21] S. Kaar, K. Steineder, R. Schneider, D. Krizan, C. Sommitsch, *Scr. Mater.* **2021**, *200*, 113923.
[22] D. Barbier, *Adv. Eng. Mater.* **2014**, *16*, 122.
[23] Y. Toji, H. Matsuda, D. Raabe, *Acta Mater.* **2016**, *116*, 250.
[24] A. Navarro-López, J. Sietsma, M. J. Santofimia, *Metall. Mater. Trans. A* **2016**, *47*, 1028.
[25] C. Blankart, S. Wesselmecking, U. Krupp, *Metals* **2021**, *11*, 1879.
[26] M. Morawiec, A. Skowronek, A. Kozłowska, C. Garcia-Mateo, A. Grajcar, *J. Therm. Anal. Calorim.* **2023**, *148*, 1365.

[27] M. A. Ackermann, *Doctorate Dissertation*, RWTH Aachen University, Aachen, Germany **2020**.
[28] D. Panasiuk, I. Daigo, T. Hoshino, H. Hayashi, E. Yamasue, D. H. Tran, B. Sprecher, *J. Ind. Ecol.* **2022**, *26*, 1040.
[29] D. Raabe, M. Jovičević-Klug, D. Ponge, A. Gramlich, A. K. da Silva, A. N. Grundy, H. Springer, I. S. Filho, Y. Ma, *Annu. Rev. Mater. Res.* **2024**, *54*, 247.
[30] W. Hagedorn, A. Gramlich, K. Greiff, U. Krupp, *Sustainable Mater. Technol.* **2022**, *34*, e00509.
[31] M. Cai, H. Ding, J. Zhang, L. Li, X. Li, L. Du, *J. Iron Steel Res. Int.* **2009**, *16*, 55.
[32] M. Gomez, C. I. Garcia, D. M. Haezebrouck, A. J. Deardo, *ISIJ Int.* **2009**, *49*, 302.
[33] A. Mertens, P. J. Jacques, J. Sietsma, F. Delannay, *Steel Res. Int.* **2008**, *79*, 954.
[34] D.-W. Suh, S.-J. Park, C.-S. Oh, S.-J. Kim, *Scr. Mater.* **2007**, *57*, 1097.
[35] C. Garcia-Mateo, F. G. Caballero, H. K. D. H. Bhadeshia, *ISIJ Int.* **2003**, *43*, 1821.
[36] M. Peet, H. Bhadeshia, MAP_STEEL_MUCG83 (Materials Algorithms Project Program Library). Cambride University (UK), software, https://www.phase-trans.msm.cam.ac.uk/map/steel/programs/mucg83.html.
[37] J. Tian, G. Xu, Z. Jiang, X. Wan, H. Hu, Q. Yuan, *Steel Res. Int.* **2019**, *90*, 1800474.
[38] S. Lin, A. Borgenstam, A. Stark, P. Hedström, *Mater. Charact.* **2022**, *185*, 111774.
[39] J. Tian, G. Xu, M. Zhou, H. Hu, Z. Xue, *J. Iron Steel Res. Int.* **2019**, *26*, 846.
[40] K. Zhu, C. Mager, M. Huang, *J. Mater. Sci. Technol.* **2017**, *33*, 1475.
[41] H. K. D. H. Bhadeshia, *Theory of Transformations in Steels*, CRC Press, Boca Raton, FL **2021**.
[42] H. K. D. H. Bhadeshia, R. W. K. Honeycombe, *Steels: Microstructure and Properties*, Butterworth-Heinemann, Amsterdam **2017**.
[43] R. P. Todorov, K. G. Khristov, *Met. Sci. Heat Treat.* **2004**, *46*, 49.
[44] S. Jones, H. Bhadeshia, *Acta Mater.* **1997**, *45*, 2911.
[45] S.-S. Li, Y.-H. Liu, Y.-L. Song, L.-N. Kong, T.-J. Li, R.-H. Zhang, *Steel Res. Int.* **2016**, *87*, 1450.
[46] E. Kozeschnik, H. K. D. H. Bhadeshia, *Mater. Sci. Technol.* **2008**, *24*, 343.
[47] B. P. J. Sandvik, H. P. Nevalainen, *Met. Technol.* **1981**, *8*, 213.
[48] H. Bhadeshia, D. V. Edmonds, *Acta Metall.* **1980**, *28*, 1265.
[49] L. C. Chang, H. K. D. H. Bhadeshia, *Mater. Sci. Technol.* **1995**, *11*, 874.
[50] O. Gulbay, M. Ackermann, A. Gramlich, A. R. Durmaz, I. Steinbach, U. Krupp, *Steel Res. Int.* **2023**, *94*, 2300238.

5. Publication II

Influence of Transformation Temperature on the High-Cycle Fatigue Performance of Carbide-Bearing and Carbide-Free Bainite

O. Gulbay, M. Ackermann, A. Gramlich, A. R. Durmaz, I. Steinbach and U. Krupp:

Steel Research International (2023)

DOI: 10.1002/srin.202300238

Chapter 5 highlights the influence of isothermal transformation temperature on the HCF performance of CBB and CFB. The fatigue limit of each bainite state is determined using the staircase method on a 1 kHz resonant testing machine. A modified one-specimen load increase test (LIT) is introduced as an efficient alternative for estimating fatigue limits using a high-frequency testing machine. The assessment of fatigue performance is supported by quasi-static tensile testing of each bainite state, along with through characterization using SEM, EBSD, and SYXRD. The main findings are summarized below:

- The proposed LIT demonstrates efficiency to be an alternative method to estimate the fatigue limit of bainitic steels at high frequency testing conditions, offering a faster approach compared to the conventional staircase method.
- Unindexed regions in the EBSD maps of CFB are effectively used to identify MA islands. The resulting statistical data provide valuable insights to assess the fatigue behaviour of both alloys.
- An increased fraction and stability of film-like γ_R, obtained at a lower transformation temperature, enhances the HCF performance of CFB by absorbing crack propagation energy through an improved TRIP effect. An increased fraction of unstable blocky γ_R and MA islands in high-temperature CFB deteriorates HCF performance.
- Finer carbide distribution and increased fraction of high-angle boundaries, generated at a lower transformation temperature, improve the HCF performance of CBB due to enhanced barrier effect against fatigue crack propagation.

RESEARCH ARTICLE

steel research international
www.steel-research.de

Influence of Transformation Temperature on the High-Cycle Fatigue Performance of Carbide-Bearing and Carbide-Free Bainite

Oguz Gulbay, Marc Ackermann, Alexander Gramlich, Ali Riza Durmaz, Ingo Steinbach, and Ulrich Krupp*

This study investigates the high-cycle-fatigue (HCF) behavior of carbide-bearing bainite (CBB) and carbide-free bainite (CFB) fabricated at different transformation temperatures. The fatigue limit of each material is determined via staircase method using a 1 kHz resonant testing machine. A new load increase test is proposed as an efficient alternative to estimate the fatigue limit in HCF regimes. The assessment of the fatigue behavior is accompanied by data-driven microstructural analyses via state-of-the-art computer vision tools. The analyses reveal that the finer carbide distribution, which is obtained at lower transformation temperature, enhances the overall performance of CBB. Electron backscatter diffraction (EBSD) measurements of CFB before and after tensile testing evidence the transformation of retained austenite (RA) to martensite during deformation. The finer film-like and stable RAs, which are promoted via reduction in transformation temperature, enhance the HCF properties by absorbing the energy required for fatigue crack propagation through improved transformation-induced plasticity. However, blocky unstable RA and/or martensite-austenite (MA) islands at prior austenite grain boundaries deteriorate the HCF properties of high-temperature CFB. Furthermore, unindexed regions in EBSD maps are effectively used to differentiate the MA islands of CFB, as validated by scanning electron microscopy (SEM) images and deep learning-based MA island segmentation.

1. Introduction

The development of new steels with good mechanical properties and high-fatigue resistance is critical for various industries because it improves the longevity and reliability of structures and components, which consecutively increases the circularity of the steel industry.[1] Bainitic steels with cost-effective alloying concepts have attracted significant research attention to fulfil the requirements of many industrial applications. The performance of bainitic steels is highly related to the microstructural constituents and their morphology, which can be tailored by the chemical composition and processing parameters. In general, bainitic steels can be divided into two subgroups based on their microstructural constituents: carbide-bearing bainite (CBB) and carbide-free bainite (CFB). If there is no kinetic hindrance, then at higher temperatures bainitic steel may experience carbide precipitation (mostly cementite) in between bainitic ferrite (BF) plates. At lower temperatures, some of the carbon can be trapped and/or precipitated in supersaturated ferrite due to lower diffusion, leading to reduced amount of carbon partitioning into surrounding austenite, therefore, finer carbide precipitation between and within the BF plates.[2,3] In contrast, by the addition of silicon (>1 wt%), retained austenite (RA) can be introduced as secondary phase.[4,5] The low solubility of silicon in cementite hinders cementite precipitation. This enables carbon diffusion from ferrite to austenite during phase transformation, which results in stabilization of the austenite.[6,7] Commonly, RA exhibits

O. Gulbay, M. Ackermann, A. Gramlich, U. Krupp
Steel Institute
RWTH Aachen University
52072 Aachen, Germany
E-mail: oguz.guelbay@iehk.rwth-aachen.de

The ORCID identification number(s) for the author(s) of this article can be found under https://doi.org/10.1002/srin.202300238.

DOI: 10.1002/srin.202300238

A. R. Durmaz
Meso and Micromechanics
Fraunhofer Institute for Mechanics of Materials IWM
79108 Freiburg, Germany

I. Steinbach
Interdisciplinary Center for Advanced Material Simulations
Ruhr Universität Bochum
44801 Bochum, Germany

ADVANCED SCIENCE NEWS
www.advancedsciencenews.com

steel research international
www.steel-research.de

film-like morphology between BF plates with a higher stability or blocky morphology with a lower stability.[4] Depending on the stability of austenite that varies with local carbon concentration, size, and morphology, some part of it may transform to martensite during cooling and form a complex structure called martensite–austenite (MA) islands.[8–10] The RA may transform to martensite through transformation-induced plasticity (TRIP) effect during deformation, leading to enhanced performance of the steel under static,[10,11] and cyclic loading[12,13] conditions. According to the incomplete-reaction phenomenon (T_0 concept), the reduction in transformation temperature results in more diffusionless bainite transformation until a critical carbon concentration is reached, in which the free energy of BF is no longer less than that of austenite.[14] Therefore, at lower transformation temperatures, in addition to refinement of microstructural constituents, fraction, size, morphology, chemical composition, and stability of RA can also be altered.[2,15] Therefore, designing bainitic steels requires understanding the microstructure and its influence on the steel's performance during engineering applications.

Fatigue properties of bainitic steels have been broadly studied.[13,16–21] It is suggested that the propagation of fatigue crack is strongly influenced by microstructural barriers such as, bainite block boundaries, packet boundaries, and prior austenite grain boundaries.[16–18] It was reported that carbides in CBB may reduce the fatigue life by causing stress concentration during cyclic loading.[19] However, the impact of RA in CFB is relatively complicated. It is reported that RA may transform to martensite at the crack tip, which absorbs the energy required for crack propagation and decelerates the crack growth. On the other hand, Gao et al.[13] showed that while interplate film-like RA arrested the crack growth via martensitic transformation and changed the active slip system, the blocky RA or MA islands located at prior austenite grain boundaries led to intergranular fatigue cracking. However, most of the studies focused on the fatigue behavior of CFB and there are only a limited number of comparative studies on CBB and CFB in high-cycle fatigue (HCF) regimes.

The fatigue limit is one of the most important measures for engineering applications and outcome of a fatigue test series. It essentially quantifies the stress amplitude limit below which macroscopic fatigue crack should not initiate during cyclic loading, which is used to design components to avoid failures and promote sustainability. As one of the traditional methods, staircase test method (up-and-down method) is often used to determine the fatigue limit of materials.[22–25] Although determination of fatigue limit via traditional methods might be more reliable, it is still expensive, time-consuming, and requires a large amount of specimens.[26,27] In recent years, multiple studies are conducted for rapid determination of fatigue limit (or fatigue life) based on temperature evolution of specimens during fatigue testing correlated with fatigue damage of material, which is used to estimate the fatigue strength and the fatigue limit.[26–33] It is important to develop efficient, cheaper, and compatible methods to estimate fatigue limit of materials, especially to increase the applicability of these tests for industrial purposes (e.g., component testing). The load increase test (LIT) is one of these methods being used to estimate fatigue limit of various materials,[31–33] which provides reliable estimation of fatigue limit in a time- and cost-efficient manner. However, most of the studies on LIT are employed in low frequencies and relatively at small number of cycles.[31–33] For this matter, a new LIT procedure is proposed using a 1 kHz resonance fatigue testing machine to estimate fatigue limit of bainitic steels in HCF regimes.

The first aim of this study is the comprehensive characterization of microstructure, mechanical properties, and HCF behavior of CBB and CFB formed at two different temperatures. The second aim is the verification of the fatigue limit of the studied bainitic steels determined via staircase method with the results obtained from the proposed LIT.

2. Experimental Section

2.1. Materials

Two steel ingots (80 kg), Fe–0.2C–2.5Mn and Fe–0.2C–1.5Si–2.5Mn (wt%), were produced in a laboratory-scale vacuum induction furnace. The ingots of $140 \times 140\ mm^2$ were homogenized at 1200 °C and forged down to the billets of $60 \times 60\ mm^2$. Subsequently, another homogenization process for 5 h was performed followed by furnace cooling. Silicon was added to the second alloy to prevent cementite precipitation during the bainitic transformation. The measured chemical compositions of the two alloys were given in **Table** 1. Similarly, this chemical composition concept was chosen to generate CBB and CFB.

2.2. Dilatometry

Dilatometry was used to determine phase transformation temperatures (A_{c1}, A_{c3}, and M_s) as well as to characterize the transformation behavior during heat treatments. For the experiments, a DIL 805A/D (TA instruments, Germany) dilatometer and rectangular specimens ($4.0 \times 7.0 \times 1.4\ mm^3$) were used. The A_{c1} and A_{c3} were determined using a heating rate of $0.05\ K\ s^{-1}$. The M_s was determined via quenching the specimens to room temperature with a cooling rate of $100\ K\ s^{-1}$ after the austenitization was completed, which was determined to be $\approx M_s = 375$ °C for both alloys. For the rest of the experiments, the heating rate was set to $3.33\ K\ s^{-1}$, where as the austenitization temperature was selected as $A_{c3} + 60$ K for a duration of 300 s for both steels to ensure fully austenitic microstructures. With respect to the isothermal heat treatments, the specimens were cooled with $100\ K\ s^{-1}$ to isothermal holding temperatures of 400 and 450 °C and held for 45 min, respectively. This was followed by a final quenching to room temperature with $100\ K\ s^{-1}$. The dilatometer experiments were graphically represented, and the material annotations based on the alloy and heat

Table 1. Chemical compositions of the investigated steels in wt.-%. The chemical compositions were determined with optical emission spectroscopy (OES) and carbon was determined with combustion analysis.

Alloy	C	Si	Mn	P	S	Cr	Mo	Al	Cu
CBB	0.18	0.01	2.48	0.003	0.002	0.04	0.01	0.002	0.02
CFB	0.19	1.48	2.38	0.003	0.003	0.04	0.01	0.003	0.02

ADVANCED SCIENCE NEWS
www.advancedsciencenews.com

steel research international
www.steel-research.de

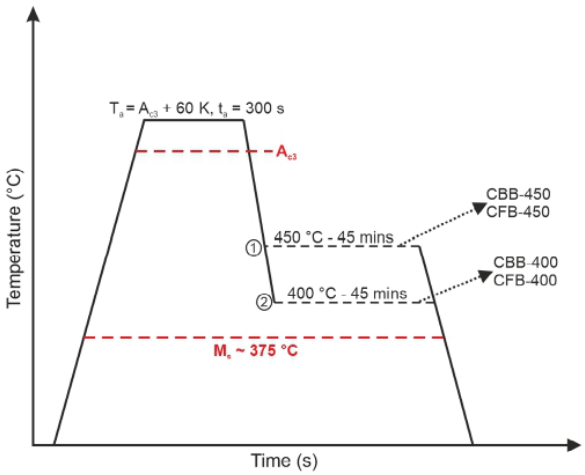

Figure 1. Schematic time–temperature diagram of dilatometer experiments for CBB and CFB alloys.

treatments were shown in **Figure 1**. To investigate the mechanical and fatigue properties of the materials, heat treatments were reproduced in salt baths for the testing samples.

2.3. Microstructural Investigation

The surface of the specimens was prepared for metallographic analysis by mechanical grinding up to 1200 SiC grit paper followed by polishing with 6 and 1 µm diamond paste. Subsequently, the specimens were etched with 3% HNO_3 (Nital). Scanning electron microscopy (SEM) investigations were carried out using a field-emission gun Zeiss Sigma SEM (Carl Zeiss Microscopy GmbH, Germany) with a 30 µm aperture, an accelerating voltage of 15 kV and a working distance of 9 mm for the secondary electron (SE) detector, where as the accelerating voltage and working distance were reduced to 5 kV and 2 mm, respectively, for the high-resolution measurements with InLens detector. For the fracture surface investigations of the fatigue specimens, the SEM was employed with aperture sizes up to 75 mµ, an accelerating voltage of 15 kV, and working distances up to 20 mm using the SE detector. For electron backscatter diffraction (EBSD) measurements, the specimens were polished with oxide polishing suspension (OPS) for ≈20 min after the final mechanical polishing step. The EBSD measurements were conducted using a NordlysNano (Oxford Instruments, Great Britain) detector with a 75 µm aperture, an accelerating voltage of 20 kV, a working distance of 17 mm, and a step size of 100 nm for the CBB alloys, where as it was reduced to 50 nm for the CFB alloys to be able to detect nanoscale RA. The SEM images were analyzed with ImageJ software to determine the width of BF plates and RA films of the CFB alloys. Postprocessing of the EBSD data was carried out with the MATLAB (MathWorks Inc., USA) toolbox MTEX.[34] Low-angle grain boundaries were defined by a misorientation angle $5° \leq \theta \leq 15°$, where as high-angle grain boundaries were defined as $\theta > 15°$.

For the carbide analysis, a customized MATLAB script for rule-based image processing was written based on ref. [35,36] Grain boundaries with similar pixel values as the carbides were filtered by first applying a low circularity value to MATLAB's regionprops function using Image Processing Toolbox and subsequently subtracting the filtered grain boundary regions from the mask. Finally, the total carbide fraction, carbide area, and carbide equivalent diameter were calculated from the final mask. In total, three micrographs were analyzed covering $57 \times 53\ \mu m^2$ per image and averaged for each CBB material condition.

A deep learning model was used as a second approach to segment the MA islands in CFB steel. The model was previously trained on SEM micrographs of bainitic steels with 512×512 image size. For further details on the training data, used model, and hyperparameters, the reader was referred to ref. [37] The calculation of the MA fraction per image was based on 48 cropped images to 512×512 px covering a total area of $170 \times 228\ \mu m^2$.

2.4. Retained Austenite Measurement

To quantify and compare the RA phase fractions of the CFB alloys, EBSD, Feritscope, and synchrotron X-ray diffraction (SYXRD) were employed. Details for the EBSD measurements and postprocessing were explained in Section 2.3. Ferromagnetic portion of the CFB alloys was determined via Feritscope (Helmut Fischer GmbH, Germany) to obtain RA fraction. Calibration of the Feritscope was done using standard magnetic saturation via 14.7%, 30.6%, 86.2%, and 100% ferromagnetic materials supplied by the manufacturer. For each specimen, the RA phase fraction was computed as an average of ten measurements. Ex situ SYXRD experiments were conducted at beamline P21.1 of PETRA III at Deutsches Elektronen-Synchrotron Center (DESY) in Hamburg, Germany. The beamline was operated at a fixed energy of 82.5 kV, supplying X-ray with a wavelength of ≈0.15 Å. Postprocessing of the obtained diffraction profiles to quantify the RA fractions of CFB alloys was done via Rietveld refinement method with Materials Analysis Using Diffraction (MAUD) software.[38]

2.5. Mechanical Testing

For uniaxial tensile tests, B5 × 25 cylindrical tensile specimens with a gauge diameter of 5 mm and a gauge length of 25 mm were used. The uniaxial tensile tests were performed with a universal electromechanical testing machine ZWICKROELL Z100 (ZwickRoell GmbH & Co. KG, Germany) at room temperature with a strain rate of $0.001\ s^{-1}$. Three tensile specimens were tested for each condition. After the completion of the tensile tests, one tensile specimen from each CFB alloy was sectioned ≈10 mm below the fracture surface for microstructural characterization. The preparation of the sectioned surfaces was done according to Section 2.3. Moreover, hardness of the dilatometer specimens was measured using Vickers 10 (HV10) indentation. To make sure that the hardness values were representative, five indentations were done on different positions of the specimens and the average of these measurements was taken as a representative hardness value of the materials.

ADVANCED SCIENCE NEWS
www.advancedsciencenews.com

steel research international
www.steel-research.de

2.6. Fatigue Testing

For fatigue tests, cylindrical fatigue specimens with the smallest gauge diameter of 4 mm and a total length of 107 mm were used. The surface of the specimens was mechanically polished with diamond paste down to 1 µm to increase the surface quality. The tests were performed on a RUMUL GIGAFORE 50 (Russenberger Prüfmachinen AG, Switzerland) resonant testing machine with a testing frequency of 1 kHz and a stress ratio o f $R = -1$.

For LIT, only one specimen was used for each material state. Tests were started from an initial stress amplitude and tested for 10^6 cycles. After each 10^6 cycles, the test was stopped and the stress amplitude was increased by 10 MPa. This procedure was applied until the fracture occurred. The temperature of the specimen surface was monitored via a thermocouple during the tests and cooling was not applied.

For staircase testing, 8–10 specimens were used for each material state. The test limit was set to 10^7 cycles. With respect to this, specimens that failed before the test limit were annotated as failures, where as the ones that survived 10^7 cycles were annotated as runouts. In the case of a failure or a runout, the stress amplitude was respectively decreased or increased by 5 MPa in the subsequent test. The specimens were cooled down via air cooling during the tests. Moreover, the average fatigue limit derived from the staircase method was determined by the equation from Dixon–Mood.[23] The equation for the average fatigue limit is

$$\mu = S_0 + \Delta S\left(\frac{\sum_{i=0}^{i_{max}} i n_i}{\sum_{i=0}^{i_{max}} n_i} \mp 0.5\right) \quad (1)$$

where S_0 is the minimum stress amplitude of the less frequent occurrence of failed or survived specimens, ΔS is the step size, the parameter i is an integer which represents the stress amplitude level, i_{max} is the highest stress amplitude level reached in staircase, n_i is the number of specimens of the less frequent event at stress amplitude level i. If the failure is more frequent, $i = 0$ corresponds to the lowest stress amplitude level at which a specimen survives. On the contrary, if the survival is more frequent, $i = 0$ is the lowest stress amplitude level at which specimen fails. The plus sign (+) in Equation (1) is used when failure is more frequent, where as the minus sign (–) is used when survival is more frequent. In the case of an equal number of failures and survivals, the same result would be expected as a result of both calculations.

3. Results

3.1. Dilatometry

Dilatometer specimens of both steels were isothermally heat treated at 400 and 450 °C as represented in Figure 1. After austenitization, the specimens were first quenched to isothermal holding temperatures, which appeared as a sudden increase in dilatation curves (**Figure 2**b,c). After isothermal holding, the specimens were subsequently quenched down to room temperature. In Figure 2a, the relative length change as a function of time during isothermal holding is displayed. It can be seen that, after sufficient time, all curves reached a plateau, which indicates that bainitic transformation was completed in all states. The relative change in length, after the bainitic phase transformation was completed, increased with decreasing isothermal holding temperature in both steels. In CBB alloy, it rose from 0.55% to 0.59% with a decrease of isothermal holding temperature from 450 to 400 °C, respectively. A similar trend was observed in CFB alloy by an increment from 0.41% to 0.51% with a decrease of temperature from 450 to 400 °C, respectively.

Dilatation curves of each heat treatment state after austenitization are shown in Figure 2b,c. There was no trace of further phase transformation during subsequent cooling in CBB-400 and CBB-450, indicated by no deflection in the dilatation curves (Figure 2b). This was also the case for the CFB-400 (Figure 2c). On the other hand, such a deflection was observed in the dilatation curve of CFB-450 around 100 °C (as highlighted in Figure 2c), which suggests a martensitic transformation during subsequent cooling after bainitic transformation at 450 °C.

3.2. Microstructure

SEM images of CBB-400 and CBB-450 are shown in **Figure 3**a,b, respectively. It was revealed that in both states, BF was formed as matrix and excessive carbon was precipitated as cementite, as intended. The cementite precipitates were distributed in the BF with a certain direction (≈60° with respect to the growth direction of BF) during bainitic phase transformation. SEM

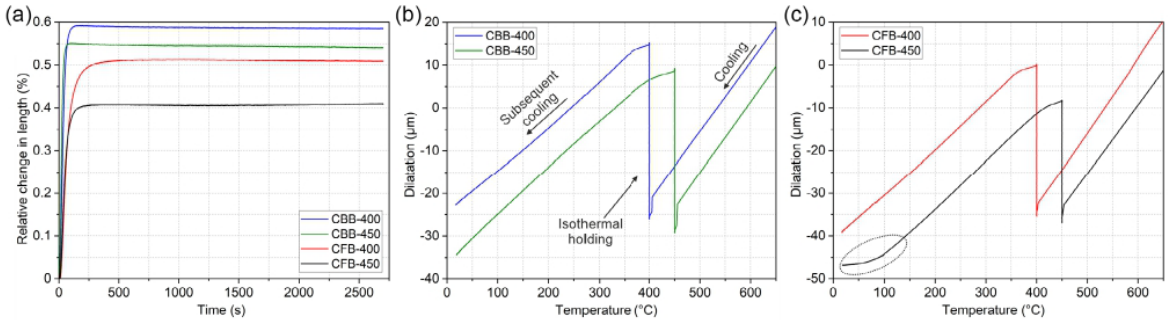

Figure 2. a) Relative length change as a function of time during isothermal holding, b) dilatation curves of CBB-400 and 450, and c) dilatation curves of CFB-400 and 450.

ADVANCED SCIENCE NEWS
www.advancedsciencenews.com

steel research international
www.steel-research.de

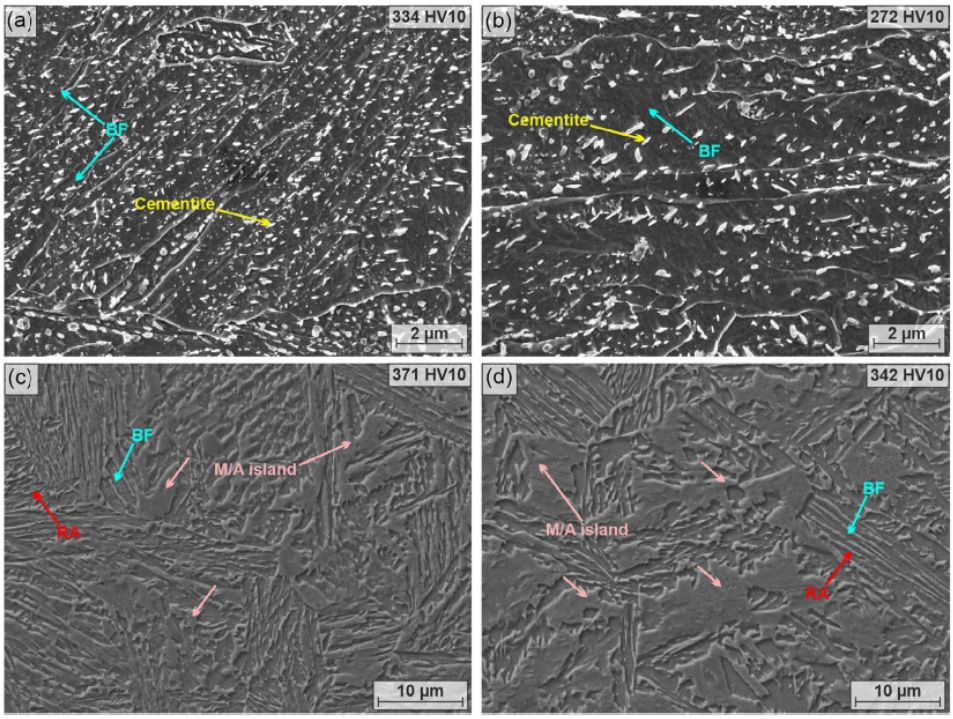

Figure 3. SEM images of a) CBB-400 and b) CBB-450 acquired via InLens detector, c) CFB-400 and d) CFB-450 acquired via SE detector.

Table 2. Average carbide diameter, average area of a carbide, and average carbide fraction with standard deviations based on analysis done on a surface area of three micrographs covering in total of ≈7282 µm^2.

Material state	Carbide diameter [nm]	Carbide area [$\times 10^5$ nm^2]	Carbide fraction [%]
CBB-400	321.73 ∓ 5.75	1.10 ∓ 0.04	13.38 ∓ 0.36
CBB-450	350.17 ∓ 13.32	1.35 ∓ 0.12	9.94 ∓ 0.85

images revealed a coarser cementite morphology with an increase in isothermal holding temperature in CBB-450, where as cementite particles were finely dispersed in CBB-400. Statistical results obtained from quantitative carbide analysis on a surface area of CBB alloys, as displayed in **Table 2**, were in a good agreement with the qualitative observation of the SEM images. Carbide diameter increased from 321 to 350 nm, the average area of a single carbide increased from 1.1×10^5 to 1.35×10^5 nm^2, where as carbide fraction decreased from 13.4% to 10% with an increase of transformation temperature from 400 to 450 °C. In addition, there was no trace of martensite or MA islands in the microstructure of both states, which is an indication of no RA in the microstructure. This was also supported by the EBSD phase maps, shown in **Figure 4**a,b, where no RA was indexed both in CBB-400 and CBB-450.

CFB-400 and CFB-450 exhibited plate-like BF as displayed in Figure 3c,d, respectively. The RA films were observed in between the BF plates. It was noticed that the microstructure became finer with decreasing isothermal holding temperature. The average width of the BF plates was measured as 0.15 µm in CFB-400, where as it was increased to 0.24 µm in CFB-450. Similarly, the average width of the film-like RA was 0.16 µm in CFB-400, where as it went up to 0.30 µm in CFB-450. The summary of BF and RA width of CFB alloys can be found in **Table 3**.

In addition, MA islands were observed in both states of CFB alloy (Figure 3c,d). The amount and size of the MA islands decreased with decreasing isothermal holding temperature in CFB-400. **Table 4** shows the amount of segmented MA islands via deep learning evaluation model as well as unindexed pixels obtained during EBSD measurements for CFB alloys. Regarding the deep learning model, the fraction of MA islands was determined as 17.9% in CFB-450, where as it was decreased to 11.7% in CFB-400. When EBSD phase maps of CFB alloys are considered, the fraction of unindexed pixels (displayed in orange) was considerably high (Figure 4c,d). The fraction of the unindexed pixels was 8.8% in CFB-400, where as it was increased to 19% in the CFB-450. It is worth to mention that the fraction of unindexed pixels obtained for CFB-alloys was in good agreement with the MA island fractions acquired via segmentation model (Table 4). On top of this, most of the unindexed pixels appeared as big clusters consisting of very small RA particles (Figure 4c,d). Moreover, the size and morphology of these big unindexed clusters displayed substantial similarities with the MA islands observed in Figure 3c,d.

Based on the EBSD phase maps, not only film-like RA but also blocky type RA was detected, especially in CFB–400 (Figure 4c).

ADVANCED SCIENCE NEWS
www.advancedsciencenews.com

steel research international
www.steel-research.de

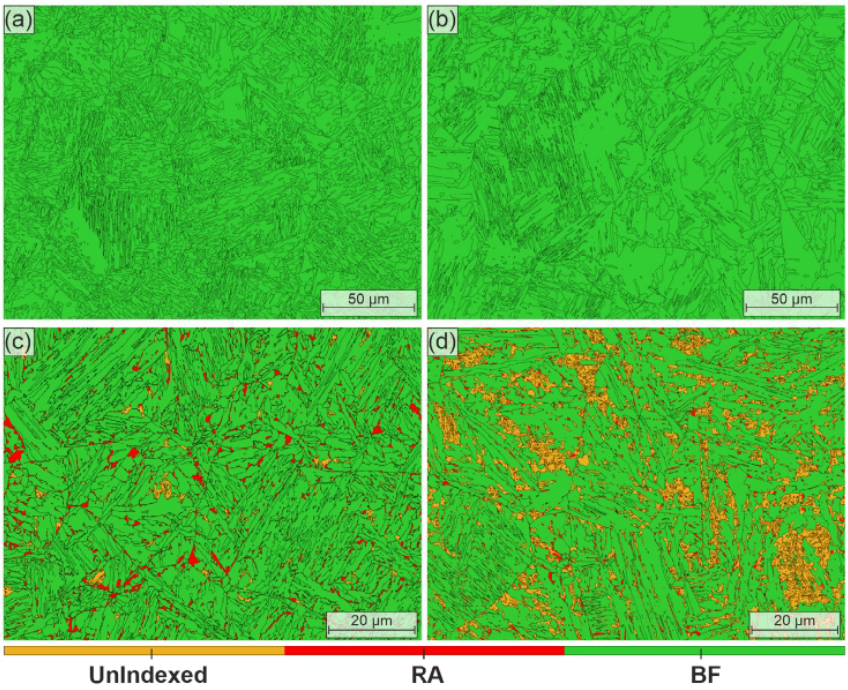

Figure 4. EBSD phase maps of a) CBB-400, b) CBB-450, c) CFB-400, and d) CFB-450.

Table 3. Average width of BF plates and RA films of CFB-400 and CFB-450.

Material state	Bainitic ferrite [µm]	Retained austenite [µm]
CFB-400	0.15 ∓ 0.04	0.16 ∓ 0.05
CFB-450	0.24 ∓ 0.06	0.30 ∓ 0.07

Table 4. Fraction of segmented MA islands and unindexed pixels in EBSD maps of CFB alloys.

Material state	Segmented MA islands [%]	EBSD unindexed pixels [%]
CFB-400	11.7 ∓ 3.3	8.8
CFB-450	17.9 ∓ 4.2	19

It was recognized that the blocky RA was mostly located on the prior austenite grains boundaries (PAGB). In the case of CFB-450, instead of blocky RA, mostly big unindexed clusters were observed located on the PAGB, where as small RA particles were indexed in or around these clusters (Figure 4d).

Moreover, the CFB-400 exhibited 3.3% RA, where as it was 1.1% in CFB-450 (displayed in red) according to the EBSD measurements. However, RA detected via EBSD was significantly lower compared to the results acquired via Feritscope and Synchrotron X-ray diffraction (SYXRD). In CFB-400, the fraction of RA measured as 16.2% and 14.3%, where as it was 8.9% and 8.7% in CFB-450 via Feritscope and SYXRD, respectively. The RA measurements via different techniques are shown in

Table 5. Retained austenite fraction of CFB alloys obtained via different methods.

Material state	EBSD [%]	Feritscope [%]	SYXRD [%]
CFB-400	3.3	16.2 ∓ 0.6	14.3
CFB-450	1.1	8.9 ∓ 0.5	8.7

Table 5. Overall results showed that the CFB-400 contained more RA in the final microstructure compared to CFB-450.

3.3. Mechanical Properties

Table 6 shows the mechanical properties for each specimen condition. Furthermore, engineering stress–strain curves are presented in **Figure 5**a. Similar in Figure 5a, all stress–strain curves exhibited continuous yielding behavior and uniform plastic deformation. The CFB alloys exhibited considerably better

Table 6. Mechanical properties of the materials.

Material state	$R_{p0.2}$ [MPa]	R_m [MPa]	A_g [%]	A_5 [%]	Hardness [HV10]
CBB-400	738 ∓ 13	866 ∓ 12	4.2 ∓ 0.7	13.4 ∓ 0.6	334 ∓ 7
CBB-450	589 ∓ 13	720 ∓ 17	6.0 ∓ 0.9	16.8 ∓ 1.2	272 ∓ 9
CFB-400	765 ∓ 5	1134 ∓ 4	11.6 ∓ 0.6	19.4 ∓ 0.2	371 ∓ 5
CFB-450	667 ∓ 5	1137 ∓ 15	8.5 ∓ 1.0	14.3 ∓ 2.0	342 ∓ 3

ADVANCED SCIENCE NEWS
www.advancedsciencenews.com
steel research international
www.steel-research.de

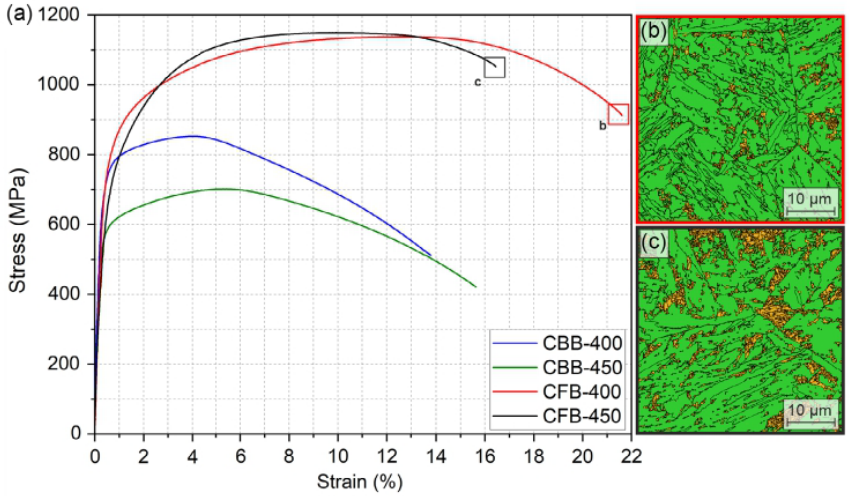

Figure 5. a) Engineering stress–strain curves of all CBB and CFB alloys. EBSD phase map of b) CFB-400 and c) CFB–450 after deformation.

mechanical properties than the CBB alloys, that is, higher strength, ductility, as well as hardness.

In the CBB alloy, with the holding temperature decreasing from 450 to 400 °C, the yield strength ($R_{p0.2}$) increased from 589 to 738 MPa, the tensile strength (R_m) increased from 720 to 866 MPa and the hardness increased from 272 to 334 HV10. In contrast, the uniform elongation (A_g) decreased from 6.0% to 4.2%, where as the total elongation (A_5) decreased from 16.8% to 13.4%.

In the case of the CFB alloy, a similar trend was noticed on the change of the mechanical properties, when the isothermal holding temperature was decreased from 450 to 400 °C. The yield strength increased from 667 to 765 MPa, the hardness increased from 342 to 371 HV10, where as the tensile strength of both specimens remained between 1130 and 1140 MPa. The uniform elongation was raised from 8.5% to 11.6%, where as the total elongation was raised from 14.3% to 19.4%. Apart from that, EBSD phase maps of CFB-400 and CFB-450 are shown in Figure 5b,c, respectively. Unlike the undeformed state of CFB alloys (Figure 4c,d), only traces of RA were found after deformation.

3.4. Fatigue Properties

LIT was conducted for each material state (**Figure 6**a,c,e,g). For the CBB alloys, the initial stress amplitude was set to 300 MPa, where as it was set to 400 MPa for CFB alloys, values being far below the yield strength of the materials (see Table 6). After each 10^6 cycles, the test was stopped and the stress amplitude was increased by 10 MPa until the fracture occurred. The temperature of the specimen surface was monitored via a thermocouple during the tests. It was observed that the temperature increased with increasing number of cycles and stress amplitude in all specimens. Before the specimens failed, the temperature increase became significant compared to the main phase of the test. Moreover, the stress amplitude, where the significant temperature jump occurred, was presumed as an approximation of the fatigue limit of the material. In general, it is clear that the CFB alloys exhibited substantially better performance during LIT. For CBB-400 and CBB-450, both specimens failed when the stress amplitude reached to 340 MPa (Figure 6a,c). In the case of CFB-400 and CFB-450, the specimens failed at a stress amplitude of 470 and 450 MPa, respectively (Figure 6e,g). It is also worth mentioning that the temperatures reached in CFB alloys were considerably higher than what was achieved in CBB alloys.

In addition, and to verify the LIT, the staircase method was applied to determine the fatigue limit of the materials. The test limit was set to 10^7 cycles. If a specimen failed at cycles less than 10^7, the stress amplitude was decreased by 5 MPa for the next test. Otherwise, the stress amplitude was increased by 5 MPa for the subsequent test. Average fatigue limit values of each material were calculated by the Dixon–Mood equations.[23] Graphical representations of staircase testing results based on failures and survivals are given in Figure 6b,d,f,h for each material state. The average fatigue limit of CBB-400 was determined as 343 MPa, where as it decreased to 330 MPa in CBB-450. The CFB alloys exhibited a very higher fatigue limit by 495 and 479 MPa, respectively, in CFB-400 and CFB-450. Determined fatigue limit data of each material state via both methods are shown in **Table 7**.

In addition to the determination of the fatigue limit, fracture surface of the fatigue specimens were investigated via SEM to identify the fatigue crack origins of the investigated alloys. It was observed that the fatigue crack initiated from the surface (highlighted with black arrow) in all the materials (Appendix A, Figure A1, Supporting Information). Furthermore, the crack propagation region of CFB alloys were larger than the crack propagation region of CBB alloys. In all the failed specimens, including LIT, no other pattern was observed.

4. Discussion

4.1. The Effect of Heat Treatment on Microstructure

Microstructural investigations showed that silicon addition to CFB alloys prevented the cementite precipitation due to low

ADVANCED SCIENCE NEWS
www.advancedsciencenews.com

steel research international
www.steel-research.de

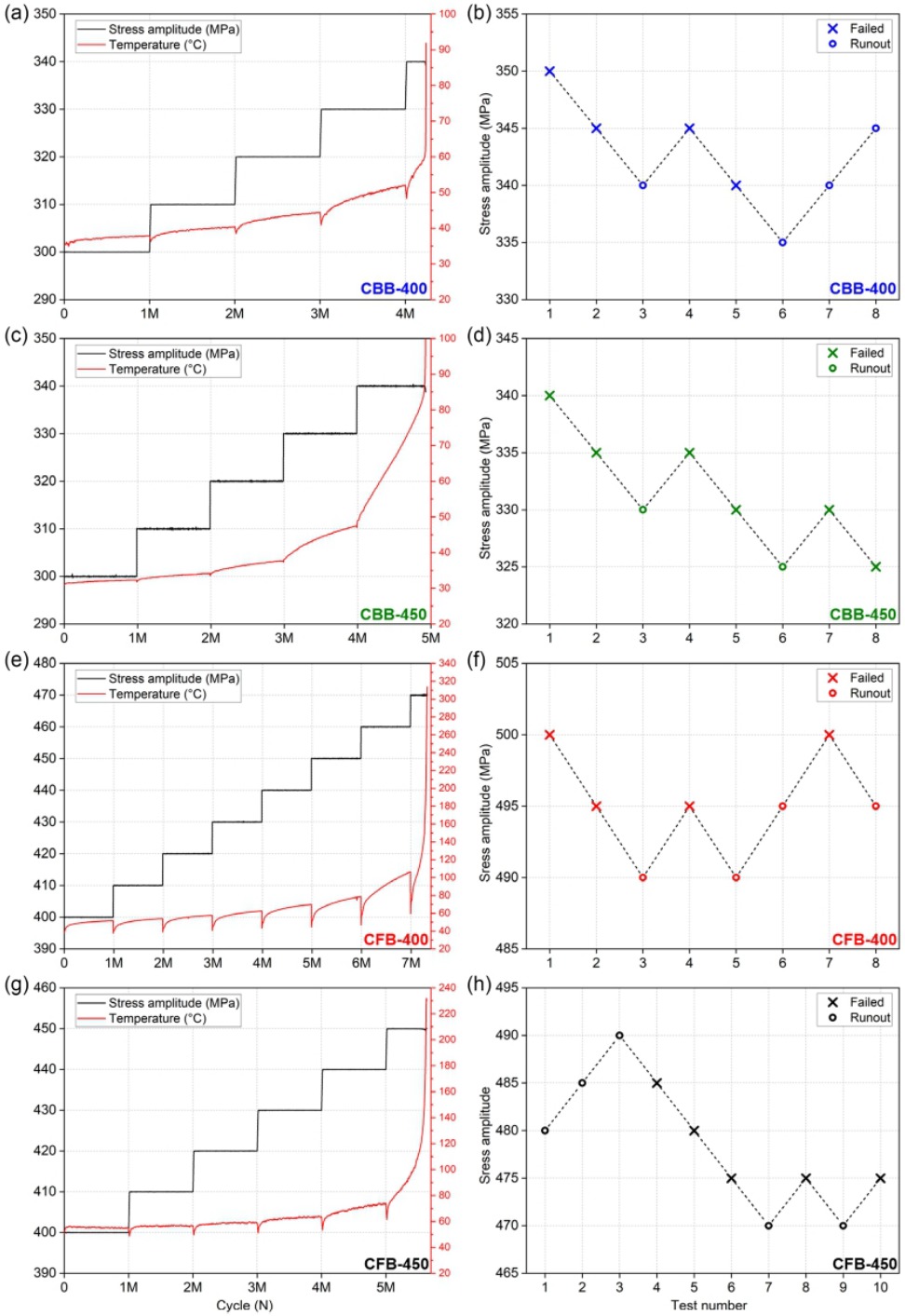

Figure 6. Load increase test of a) CBB-400, c) CBB-450, e) CFB-400 and g) CFB-450; and staircase test of b) CBB-400, d) CBB-450, f) CFB-400 and h) CFB-450.

ADVANCED SCIENCE NEWS
www.advancedsciencenews.com

steel research international
www.steel-research.de

Table 7. Fatigue limit of the materials determined via load increase test and staircase method.

Material state	Fatigue limit determined by load increase test [MPa]	Fatigue limit determined by staircase method [MPa]
CBB-400	340	343
CBB-450	340	330
CFB-400	470	495
CFB-450	450	479

solubility of silicon in cementite.[6,7] Therefore, the excessive carbon, which was rejected from BF, was enriched into the surrounding austenite during the bainitic transformation, which resulted in thermal stabilization of austenite.[6,7] Therefore, RA was observed in CFB alloys at room temperature, where as cementite precipitates were observed in CBB alloys (Figure 3).

In CBB-400, cementite precipitates showed a finer morphology and a denser distribution compared to the ones in CBB-450 (Figure 3a,b). Because of slower kinetics as a result of lower isothermal transformation temperature of CBB-400, time required for carbide precipitation increases. Therefore, it is possible that some of the carbon was trapped and/or precipitated as carbides in the BF, where as the rest was partitioned in surrounding austenite and/or precipitated as cementite.[2,39] Highly magnified InLens micrographs of CBB-400, shown in **Figure 7**a, also underpinned this hypothesis by depicting very small precipitates, which points to carbide precipitation in the BF. Contrary to this, although some smaller precipitates were visible in the micrograph of CBB-450 (Figure 7d), it was negligible compared to CBB–400. For the same reason, cementite between the BF was refined since only a part of the carbon had the opportunity to be partitioned into austenite and precipitated.

The results revealed that the inefficient detection of RA via EBSD compared to Feritscope and SYXRD. Using EBSD, only a small surface area of the specimen can be investigated. In contrast, Feritscope and SYXRD cover a certain volume of the specimens during the measurements. Another reason for insufficient RA identification is the nanoscale nature of RA films, which makes it harder to resolve them during EBSD measurement. When the phase maps of CFB-400 and CFB-450 are considered, most of the detected RA was in blocky morphology (Figure 4c,d). Similarly, the increased amount of martensitic constituents in the investigated area naturally decreases the amount of measured RA. Therefore, limited surface area and microstructural features of the investigated area may restrain the RA measurements via EBSD.

EBSD investigations of CFB alloys exhibited a considerable fraction of unindexed phases (Figure 4c,d), which can be attributed to the existence of MA islands in the microstructure. The fact that the unindexed regions appeared as big clusters as MA islands observed in SEM images (Figure 3c,d) and the size and fraction of these clusters were in good agreement with the MA islands in SEM images supported this attribution. Figure 7c,f show the band contrast (BC) maps combined with austenite phase maps for CFB-400 and CFB-450, respectively. The unindexed regions observed on the phase maps coincide with dark areas on the BC maps. It is highly likely that MA islands were not indexed because of low Kikuchi pattern quality due to high-defect density of martensitic constituents and appeared as dark on the BC maps. In addition, especially in the large unindexed regions of CFB-450, small RA particles were indexed, demonstrating the presence of untransformed RA in these regions (Figure 4d), which provides an argument for the presence of MA islands.[40] Besides this, it is significant to note that the CBB alloys, containing no martensite, displayed negligible fraction of unindexed phases compared to martensite containing

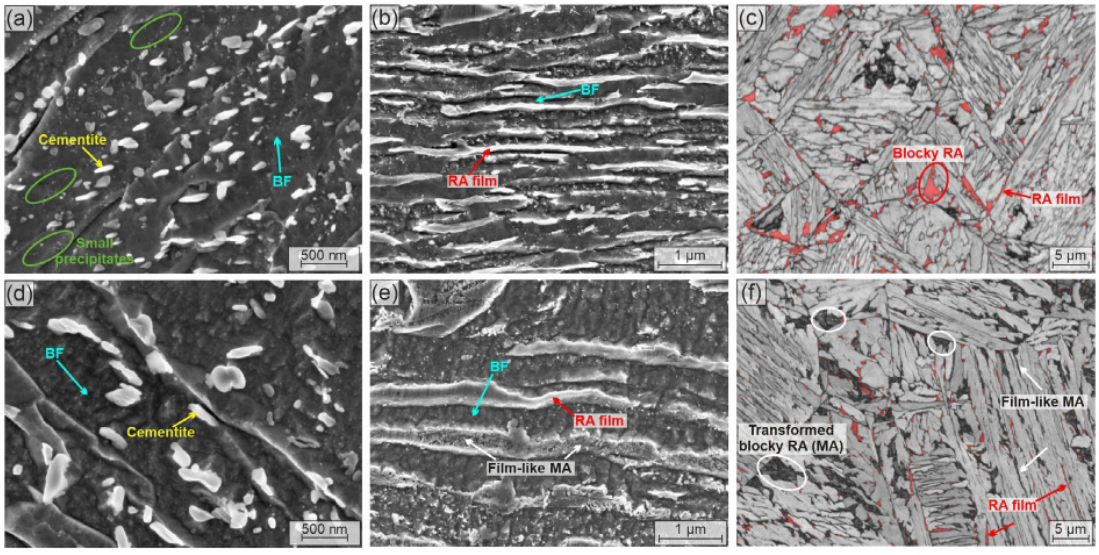

Figure 7. SEM images acquired via InLens detector of a) CBB-400, d) CBB-450, b) CFB-400, and e) CFB–450. BC map combined with austenite phase of c) CFB-400 and f) CFB-450.

ADVANCED SCIENCE NEWS
www.advancedsciencenews.com
steel research international
www.steel-research.de

CFB alloys. As a result, unindexed regions in the EBSD phase maps of CFB alloys were considered as MA islands.

The amount and size of MA islands decreased with decreasing transformation temperature. This can be related to the influence of bainite transformation temperature on BF fraction, carbon partitioning, and correspondingly, on the morphology and stability of the RA after the transformation is completed. It is widely accepted that there are two main types of austenite in CFB microstructures. One of them is nanoscale film-like austenite formed in between BF plates, the other one is rather extensive and blocky austenite.[4] According to incomplete-reaction phenomenon (T_0 concept),[14] with decreasing isothermal phase transformation temperature the diffusionless transformation of bainite can proceed even further until a critical carbon concentration is reached, where the free energy of BF is no longer less than that of austenite. Here in, at higher transformation temperatures, due to less BF formation and carbon partitioning, more blocky austenite will remain in the microstructure with less carbon enrichment, which would lead to martensitic transformation during subsequent cooling.[8] Although blocky RA on the PAGB was visible in CFB-400 (Figure 7c), multiple large dark clusters on PAGB with a similar morphology were realized in CFB-450 (Figure 7f) indicating MA island formation due to lower stability of RA in CFB–450. The dilatation curve obtained for CFB-450 supported this observation by showing a pronounced martensitic transformation during subsequent cooling (Figure 2c), which indicates the higher M_s associated with the blocky RA due to lower thermal stability.

It was also observed that the width of BF plates and RA films decreased with decreasing transformation temperature, which is in good agreement with the literature.[15,41–43] After a BF plate forms, a carbon-enriched zone forms around the BF plate due to carbon partitioning, and carbon concentration of this zone drops by distance.[44] Regarding the T_0 concept, spontaneous transformation of austenite to BF can only occur when the carbon concentration in austenite is below a certain level. In addition, at lower transformation temperatures, BF formation can start at higher carbon concentrations at the austenite interface compared to higher transformation temperatures.[14] Therefore, at 400 °C, the next BF plate can thermodynamically start forming from a smaller distance compared to 450 °C, which was inherited as thinner RA films in the microstructure of CFB-400.[44] In addition, the reduction in the BF plate width in CFB-400 can be explained by increasing strength of the RA with decreasing transformation temperature.[45] It was established that the shape change due to diffusionless bainite transformation is not accommodated elastically. In contrast, plastic relaxation is observed in the austenite adjacent to BF plate, which creates a dislocation debris that resists the further growth of BF plate. Therefore, the mechanically stronger the RA, the greater the resistance against the advancement of BF interface.[45]

Although the RA fraction of CFB-450 should have been higher considering the T_0 concept, CFB-400 exhibited a higher RA fraction in the final microstructure (Table 5). The reason might be the influence of morphology, size, and stability of RA explained above. Figure 7b,e display the images acquired via InLens detector for CFB–400 and CFB–450, respectively. These images also confirmed the low-thermal stability of RA in CFB-450, for which some of the RA films were already partly transformed to martensite (highlighted with white arrow in Figure 7e) during subsequent cooling after isothermal treatment at 450 °C, inherited by highly deformed appearance in the micrograph. This was also reflected in Figure 7f by coexistence of film-like RA (highlighted with red arrow) and dark film-like morphologies (highlighted with white arrow). In contrast, this was not the case for CFB-400 as shown in Figure 7b,c, which indicates the higher stability of the RA in CFB–400. Therefore, it is highly possible that not only the blocky RA but also some of the film-like RA transformed partly to martensite due to low-thermal stability, which led to low detection of RA as well as increased amount of film-like unindexed regions in the EBSD measurements of CFB-450.

4.2. Mechanical Properties

As a general comparison, CFB alloys clearly exhibited better mechanical properties, which is related to the microstructural differences. CFB alloys displayed significantly higher strength as well as higher uniform and total elongation than CBB alloys. The face-centered cubic RA phase can facilitate more dislocation motion than the face-centered cubic phase, which enhances the plasticity of the material during deformation.[19] In addition, the elongation can be enhanced with the introduction of RA into the bainitic microstructure, which can be altered by the processing parameters.[15] Furthermore, the metastable RA transformed to martensite progressively through TRIP effect during plastic deformation, which was indicated by the absence of RA in the microstructure after deformation (Figure 5b,c). This may lead to better deformability as well as higher tensile strength and hardness.[10,46] Moreover, solid solution strengthening due to silicon alloying is another factor that improved the mechanical properties of CFB alloys.[19,41,47]

Decreased phase transformation temperature enhanced the mechanical properties of CBB alloys. The finer carbide distribution associated with finer BF in the microstructure clearly increased the hardness, yield strength, and tensile strength of CBB–400. It is worth mentioning that this substantial improvement was not accompanied by a significant loss in ductility. Moreover, when the area below the stress–strain curve of CBB alloys is considered (Figure 5a), CBB-400 covered a larger area, which points out to higher toughness for CBB-400. Long et al.[41] also showed that the low-temperature CBB exhibited higher impact toughness than high-temperature CBB.

When the mechanical properties of the CFB alloys are considered, it is evident that mechanical properties became superior with decreasing phase transformation temperature as in CBB alloys. Increased yield strength and hardness of CFB–400 can be attributed to the increased fraction of stronger BF and refinement of the microstructure due to lower phase transformation temperature.[43] The martensitic constituents might have an influence on the increase of the yield strength and hardness of CFB-400. However, even though CFB-450 had a higher fraction of martensitic constituents, it exhibited lower yield strength and hardness. Therefore, the major reason behind this increase should be the BF fraction and refinement of the microstructure. In contrast, the tensile strength showed no improvement with a decrease in transformation temperature as in yield strength and

ADVANCED SCIENCE NEWS
www.advancedsciencenews.com
steel research international
www.steel-research.de

hardness. This indicates that the tensile strength has more dependency on the martensitic constituents existing both before and after deformation. When the microstructures are considered, CFB-400 consisted of more RA. However, if the microstructures prior to cooling just after the bainitic transformation are considered, CFB-450 is expected to have more austenite considering the T_0 concept. A forementioned, some of the RA transformed to martensite during subsequent cooling due to low stability and the RA fraction in the final microstructure was reduced. This means that after deformation, the amount of martensite in the microstructure of CFB-450 should be more than CFB-400, which explains the compensation of tensile strength of CFB-450. Improved ductility of CFB-400 can be related to finely distributed film-like RA at higher fractions with higher stability. It was suggested that the best results were obtained when the RA was in the form of films between BF plates instead of big blocky morphology.[15] In addition, when the mechanical stability of RA increased to optimum levels, ductility can be improved by the enhanced elongation through prolonged TRIP effect.[11] Finally, as a side note, it was also shown that big blocky MA islands have a negative effect on the toughness properties due to unfavorable local stress concentrations and RA stability in the MA islands.[48]

4.3. Fatigue Properties

When the overall results obtained from LIT and staircase method considered, CFB alloys exhibited substantially higher fatigue limit than CBB alloys. It was shown that the fatigue limit and fatigue strength of metallic materials increases with increasing tensile strength until a critical value is reached.[49,50] Therefore, the higher fatigue limit of CFB alloys can be mainly attributed to the higher tensile strength. Superior fatigue properties of CFB alloys were also indicated by having larger crack propagation zone because of higher resistance to fatigue crack propagation, even at significantly higher stress amplitudes (Appendix A, Figure A1, Supporting Information). It was mentioned that carbides in CBB may form micropores during fatigue loading, increase the stress concentration, and decrease the fatigue life,[19] which could be another reason why CBB alloys displayed lower HCF performance overall. In addition, in the case of CFB, the metastable RA may transform to martensite due to TRIP effect induced by plastic deformation at the fatigue crack tip during crack propagation.[12,51] Huo et al.[52] demonstrated the interaction of fatigue crack propagation with RA. Because of the strain-induced transformation of RA to martensite, the system absorbs a significant amount of energy. It was stated that the fracture energy of martensite is smaller than the fracture energy of austenite, and the overall absorbed energy during the phase transformation from RA to martensite is bigger than the fracture energy difference of martensite and RA.[52–54] Thus, fatigue crack propagation can be decelerated and/or deflected (Appendix A, Figure A2, Supporting Information). Besides causing a volume expansion, the transformation of RA to martensite may result in the generation of compressive stresses at the fatigue crack tip. These compressive stresses can close the crack tip and it can only continue to propagate again when the compressive stress is eliminated.[12,52,55]

Comparing the HCF properties of CBB alloys, CBB-400 exhibited a slightly higher fatigue limit than CBB-450 (via staircase method). It was suggested that cementite plates could be strong barriers to crack growth during fatigue loading.[56,57] Therefore, finer distribution of cementite in CBB-400 could be linked to a greater fatigue limit among CBB alloys. In addition, as displayed in **Figure 8**a, the fraction of high-angle boundaries (>15°) increased in CBB-400, which are known to be effective barriers to fatigue cracks due to their highly misoriented nature.[54] It was calculated that 88% of the boundaries in CBB–450 were high-angle boundaries, as opposed to 93% in CBB-400. What is more interesting is that the relative frequency of the boundaries with a misorientation angle of 55° and greater was 70% in CBB-450, where as it was 79% in CBB–400. As a result of these factors, the fatigue cracks branch out in CBB-400. Therefore, the total path increases during crack propagation and more energy is required to reach to critical crack length and thus, the fatigue life is improved.[54]

Although the tensile strength of CFB alloys was very similar, fatigue limit of CFB-400 was prominently higher than that of

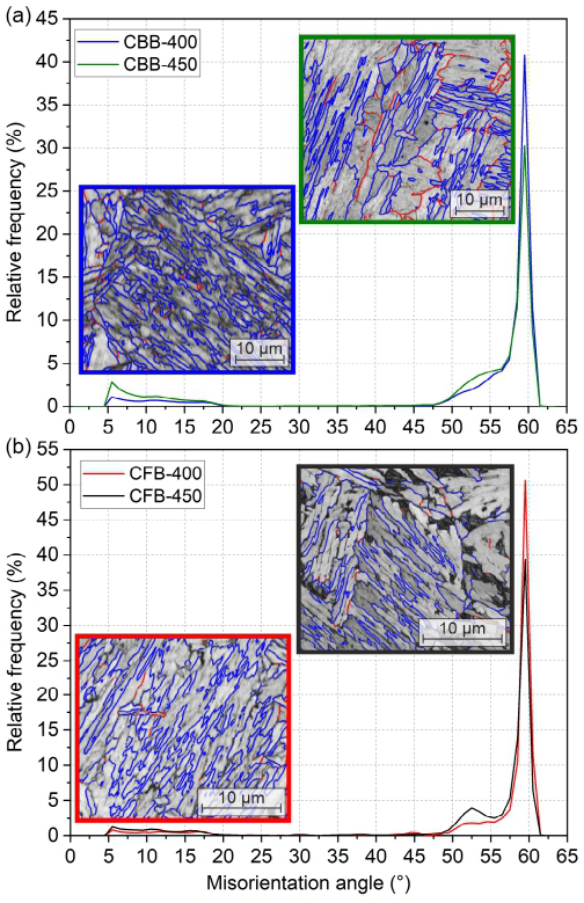

Figure 8. Grain boundary misorientation distribution of a) CBB and b) CFB alloys. Red- and blue-colored boundaries in the maps represent the low- and high-angle boundaries, respectively.

ADVANCED SCIENCE NEWS
www.advancedsciencenews.com
steel research international
www.steel-research.de

CFB-450. Enhanced fatigue limit of CFB-400 can be attributed to the following four reasons: 1) the increased number of effective barriers to prevent fatigue crack propagation due to finer morphology of BF plates and RA films; 2) with decreasing transformation temperature, fraction of the high-angle boundaries was also increased in CFB-400 (Figure 8b). The relative frequency of high-angle boundaries was 91% in CFB-450, which increased to 94% in CFB-400. In addition, 70% of the boundaries had misorientation angle of 55° and greater in CFB-450, where as this fraction was 81% in CFB 400. Compared to low-angle boundaries, high-angle boundaries are more effective barriers to deflect, decelerate, or even terminate the fatigue cracks;[54] 3) it is known that fraction, morphology, and stability of RA can be optimized via processing parameters to obtain better properties.[2,15] It is shown in the prior sections that the morphology and stability of the RA were positively altered in CFB-400, along with a higher fraction in the final microstructure compared to CFB-450. Owing to these modifications of RA, in the case of phase transformation from RA to martensite during fatigue crack propagation, more energy might be absorbed because of a prolonged TRIP effect; and 4) decreased amount and size of MA islands in the microstructure of CFB-400 might have favored the high-cycle properties. Gao et al.[13] showed that blocky RA or MA islands formed at prior austenite grain boundaries (PAGB) led to intergranular fatigue cracking due to slip impingement. Under normal circumstances, PAGB act as efficient microstructural barriers to prevent fatigue crack propagation.[16] However, as a result of blocky RA or MA island formation on the PAGB, the activation of the slip on the preferred plane of the RA becomes easier on the slip impingement, formed on the PAGB from adjacent PAG, leading to the intergranular fatigue crack.[13]

In addition to the HCF properties of the studied materials, comparison of two different methods to determine fatigue limit via high-frequency (1 kHz) resonance fatigue testing machine was conducted. Generally, it is possible to obtain more accurate results from the staircase method because it is based on a statistical approach with multiple test samples. Moreover, accuracy of the results can be improved via different parameters (e.g., step size) and more test samples. In contrast, as a consequence of the increased number of test samples, determination of fatigue limit becomes very expensive and time-consuming, even with 1 kHz testing equipment. It was observed that the results obtained from LIT were in good agreement with the results from staircase testing, especially for CBB alloys. In the case of CFB alloys, the determined fatigue limit via LIT was slightly lower than the fatigue limit determined via staircase method. When compared, significantly higher temperatures were reached in CFB alloys even in the initial stages of the LIT. At the end of the tests, CFB alloys reached temperatures beyond 200 °C, where as CBB alloys remained below 100 °C. The stress amplitudes applied to CFB alloys were also significantly higher compared to CBB alloys. Higher stress amplitudes in combination with high-testing frequencies is one of the reasons why higher temperatures were monitored in CFB alloys. In addition to the energy dissipation due to fatigue damage activities, martensitic transformation during cyclic loading might have caused an extra heat dissipation in CFB alloys, which was not the case for CBB alloys.

In the meantime, self-heating may influence the HCF properties.[58] Kozłowska et al.[59] displayed that during tensile testing, the intensity of strain-induced martensitic transformation of RA decreases because of higher stability of austenite that is corresponding to rise of stacking fault energy value of this phase.[59] Nikitin et al.[60] showed that temperature increase due self-heating inhibits the strain-induced martensitic transformation in austenitic stainless steels, which deteriorates the fatigue life. Furthermore, at high temperatures (200–300 °C), remaining RA and/or martensitic constituents may also decompose and affect the fatigue limit of the materials. Therefore, it is possible that higher temperatures due to anisothermal testing conditions may have influenced the obtained fatigue limit of CFB alloys. In contrast, the final temperature that was reached during the LIT has less importance regarding identifying the fatigue limit. If the temperature jump has already occurred, it means that the fatigue limit was already surpassed. Thus, the final temperature will have no influence on the fatigue limit as the fatigue limit is already exceeded.

However, the temperature during the LIT was still relatively high even before the final stress amplitude was reached, which may have an impact on the determined fatigue limit of CFB alloys. Therefore, some alterations in testing parameters can be made to obtain better results. For instance, active cooling can be used to observe the impact on the outcome of the test. The number of cycles to increase the stress amplitude and/or the step size of the stress amplitude increment can be changed to be able to identify the fatigue limit more accurately. Yet, it is important to consider that LIT is a one specimen test, which makes it substantially more time- and cost-efficient, and the empirical study revealed that it can provide an appropriate fatigue limit estimation of the studied materials.

5. Conclusions

In this work, a comprehensive study on CBB and CFB was performed. Assessment of HCF performance of the studied bainitic steels is completed and the influence of phase transformation temperature is investigated. A new LIT is proposed using a 1 kHz resonant testing machine as a rapid method to estimate the fatigue limit of studied bainitic steels in HCF regimes. The following conclusions can be drawn: 1) the proposed LIT is shown to be an efficient method to estimate the fatigue limit of the bainitic steels in HCF regimes as opposed to the time-consuming staircase method; 2) unindexed regions in the EBSD maps of CFB are successfully used to differentiate the MA islands. The obtained statistical data are instrumentally used to assess fatigue behavior of both alloys; 3) increased fraction and stability of RA with pronounced film-like morphology enhances the HCF performance of CFB by absorbing the energy required for crack propagation via improved TRIP effect, where as unstable blocky RA and/or MA islands formed at prior austenite grain boundaries are detrimental for HCF properties; and 4) finer carbide distribution and increased proportion of high-angle grain boundaries, as produced by lowering the transformation temperature of CBB, act as more effective barriers against fatigue crack propagation.

ADVANCED SCIENCE NEWS
www.advancedsciencenews.com

steel research international
www.steel-research.de

Supporting Information

Supporting Information is available from the Wiley Online Library or from the author.

Acknowledgements

This work was supported by the German Federal Ministry of Education and Research (BMBF) under grant numbers 13XP5118A, 13XP5118B and 13XP5118C. The authors acknowledge DESY (Hamburg, Germany), a member of the Helmholtz Association HGF, for the provision of experimental facilities. Parts of this research were carried out at PETRA III and the authors would like to thank Dr. Zoltan Hegedüs for assistance in using beamline P21.2. Beamtime was allocated for proposal I-20220679 EC. The help of Ahmet Turnali with SYXRD measurements is also gratefully acknowledged.

Open Access funding enabled and organized by Projekt DEAL.

Conflict of Interest

The authors declare no conflict of interest.

Data Availability Statement

The data that support the findings of this study are available from the corresponding author upon reasonable request.

Keywords

bainite, EBSD, fatigues, microstructures, TRIP effect

Received: April 20, 2023
Revised: June 20, 2023
Published online: July 10, 2023

[1] A. Gramlich, W. Hagedorn, K. Greiff, U. Krupp, *Adv. Eng. Mater.* **2023**, 2201931, https://doi.org/10.1002/adem.202201931.
[2] H. K. D. H. Bhadeshia, *Bainite in Steels: Transformations, Microstructure and Properties*, 2nd ed, IOM Communications, London **2001**.
[3] F. G. Caballero, M. K. Miller, C. Garcia-Mateo, *Mater. Chem. Phys.* **2014**, *146*, 50.
[4] H. K. D. H. Bhadeshia, D. V. Edmonds, *Met. Sci.* **1983**, *17*, 411.
[5] F. G. Caballero, H. Roelofs, S. Hasler, C. Capdevila, J. Chao, J. Cornide, C. Garcia-Mateo, *Mater. Sci. Technol.* **2012**, *28*, 95.
[6] E. Kozeschnik, H. K. D. H. Bhadeshia, *Mater. Sci. Technol.* **2008**, *24*, 343.
[7] B. P. J. Sandvik, *Metall. Mater. Trans. A* **1982**, *13*, 777.
[8] F. G. Caballero, C. García-Mateo, J. Chao, M. J. Santofimia, C. Capdevila, C. G. de Andrés, *ISIJ Int.* **2008**, *48*, 1256.
[9] C. Hofer, H. Leitner, F. Winkelhofer, H. Clemens, S. Primig, *Mater. Charact.* **2015**, *102*, 85.
[10] C. Hofer, S. Primig, H. Clemens, F. Winkelhofer, R. Schnitzer, *Adv. Eng. Mater.* **2017**, *19*, 1600658.
[11] C. Garcia-Mateo, F. G. Caballero, *Mater. Trans.* **2005**, *46*, 1839.
[12] M. Abareshi, E. Emadoddin, *Mater. Des.* **2011**, *32*, 5099.
[13] G. Gao, R. Liu, K. Wang, X. Gui, R. Misra, B. Bai, *Scr. Mater.* **2020**, *184*, 12.
[14] H. Bhadeshia, D. V. Edmonds, *Acta Metall.* **1980**, *28*, 1265.
[15] B. P. J. Sandvik, H. P. Nevalainen, *Met. Technol.* **1981**, *8*, 213.
[16] I. Mueller, R. Rementeria, F. G. Caballero, M. Kuntz, T. Sourmail, E. Kerscher, *Materials* **2016**, *9*, 831.
[17] M. C. Marinelli, I. Alvarez-Armas, U. Krupp, *Mater. Sci. Eng., A* **2017**, *684*, 254.
[18] R. Rementeria, L. Morales-Rivas, M. Kuntz, C. Garcia-Mateo, E. Kerscher, T. Sourmail, F. G. Caballero, *Mater. Sci. Eng., A* **2015**, *630*, 71.
[19] X. Long, F. Zhang, Z. Yang, B. Lv, *Mater. Sci. Eng., A* **2018**, *715*, 10.
[20] Y. Fan, X. Gui, M. Liu, X. Wang, C. Feng, G. Gao, *Metals* **2022**, *12*, 856.
[21] Q. Zhou, L. Qian, J. Meng, L. Zhao, F. Zhang, *Mater. Des.* **2015**, *85*, 487.
[22] W. J. Dixon, *J. Am. Stat. Assoc.* **1965**, *60*, 967.
[23] W. J. Dixon, A. M. Mood, *J. Am. Stat. Assoc.* **1948**, *43*, 109.
[24] R. Morrissey, T. Nicholas, *Int. J. Fatigue* **2006**, *28*, 1577.
[25] C. Müller, M. Wächter, R. Masendorf, A. Esderts, *Int. J. Fatigue* **2017**, *100*, 296.
[26] C. F. C. Bandeira, P. P. Kenedi, J. T. P. de Castro, *Lat. Am. J. solids Struct.* **2018**, *15*, https://www.doi.org/10.1590/1679-78254331.
[27] R. de Finis, D. Palumbo, F. Ancona, U. Galietti, *Int. J. Fatigue* **2015**, *74*, 88.
[28] K. Hayabusa, K. Inaba, H. Ikeda, K. Kishimoto, *Exp. Mech.* **2017**, *57*, 185.
[29] G. La Rosa, *Int. J. Fatigue* **2000**, *22*, 65.
[30] L. Zhang, X. S. Liu, S. H. Wu, Z. Q. Ma, H. Y. Fang, *Int. J. Fatigue* **2013**, *54*, 1.
[31] F. Walther, *Mater. Test.* **2014**, *56*, 519.
[32] F. Walther, D. Eifler, *Mater. Sci. Eng., A* **2007**, *468–470*, 259.
[33] A. Baqerzadeh Chehreh, M. Grätzel, J. P. Bergmann, F. Walther, *Metals* **2020**, *10*, 1510.
[34] F. Niessen, T. Nyyssönen, A. A. Gazder, R. Hielscher, *J. Appl. Crystallogr.* **2022**, *55*, 180.
[35] S. Ramesh Babu, T. P. Davis, T. Haas, A. Jarvenpää, J. Kömi, D. Porter, *Metals* **2020**, *10*, 171.
[36] E. R. Davies, *Computer and Machine Vision: Theory, Algorithms, Practicalities*, Academic Press, Waltham, MA, **2012**.
[37] M. Ackermann, D. Iren, S. Wesselmecking, D. Shetty, U. Krupp, *Mater. Charact.* **2022**, *191*, 112091.
[38] M. Ferrari, L. Lutterotti, *J. Appl. Phys.* **1994**, *76*, 7246.
[39] H. Bhadeshia, *Acta Metall.* **1980**, *28*, 1103.
[40] C. Hofer, F. Winkelhofer, H. Clemens, S. Primig, *Mater. Sci. Eng., A* **2016**, *664*, 236.
[41] X. Y. Long, F. C. Zhang, J. Kang, Z. N. Yang, D. D. Wu, K. M. Wu, G. H. Zhang, *Mater. Sci. Technol.* **2017**, *33*, 615.
[42] M. Morawiec, V. Ruiz-Jimenez, C. Garcia-Mateo, J. A. Jimenez, A. Grajcar, *Arch. Civ. Mech. Eng.* **2022**, *22*, 152.
[43] J. Meng, Y. Feng, Q. Zhou, L. Zhao, F. Zhang, L. Qian, *J. Mater. Eng. Perform.* **2015**, *24*, 3068.
[44] L. C. Chang, H. K. D. H. Bhadeshia, *Mater. Sci. Technol.* **1995**, *11*, 874.
[45] E. Swallow, H. K. D. H. Bhadeshia, *Mater. Sci. Technol.* **1996**, *12*, 121.
[46] H. Guo, X. Feng, A. Zhao, Q. Li, M. Chai, *J. Mater. Res. Technol.* **2020**, *9*, 1593.
[47] J. Cornide, C. Garcia-Mateo, C. Capdevila, F. G. Caballero, *J. Alloys Compd.* **2013**, *577*, S43.
[48] K. Wang, Z. Tan, G. Gao, B. Gao, X. Gui, R. Misra, B. Bai, *Mater. Sci. Eng., A* **2016**, *675*, 120.
[49] J. C. Pang, S. X. Li, Z. G. Wang, Z. F. Zhang, *Mater. Sci. Eng., A* **2013**, *564*, 331.
[50] J. C. Pang, S. X. Li, Z. G. Wang, Z. F. Zhang, *Fatigue Fract. Eng. Mater. Struct.* **2014**, *37*, 958.
[51] U. Krupp, C. West, H.-J. Christ, *Mater. Sci. Eng., A* **2008**, *481–482*, 713.
[52] C. Y. Huo, H. L. Gao, *Mater. Charact.* **2005**, *55*, 12.
[53] S. D. Antolovich, B. Singh, *Metall. Trans.* **1971**, *2*, 2135.
[54] X. Y. Qi, L. X. Du, J. Hu, R. Misra, *Mater. Sci. Eng., A* **2018**, *718*, 477.

[55] E. R. Parker, V. F. Zackay, *Eng. Fract. Mech.* **1973**, *5*, 147.
[56] K. Hussain, *Eng. Fract. Mech.* **1997**, *58*, 327.
[57] U. Krupp, *Fatigue Crack Propagation in Metals and Alloys: Microstructural Aspects and Modelling Concepts*, John Wiley distributor; Wiley-VCH, Chichester; Weinheim **2007**.
[58] Y. Yu, J. L. Gu, L. Xu, F. L. Shou, B. Z. Bai, Y. B. Liu, *Mater. Des.* **2010**, *31*, 3067.
[59] A. Kozłowska, A. Grajcar, A. Janik, K. Radwański, U. Krupp, K. Matus, M. Morawiec, *Archiv. Civ. Mech. Eng.* **2021**, *21*, 133.
[60] I. Nikitin, M. Besel, *Int. J. Fatigue* **2008**, *30*, 2044.

6. Publication III

Impact Toughness and Fatigue Crack Propagation in Carbide-Free Bainite: The Adverse Role of Retained Austenite and Martensite-Austenite Islands

O. Gulbay, A. Gramlich, U. Krupp:

Fatigue & Fracture of Engineering Materials & Structures (2025)

DOI: 10.1111/ffe.70025

Chapter 6 highlights the deformation behaviour of CBB and CFB under various loading conditions. To achieve this, uniaxial tensile, fatigue crack propagation, and instrumented Charpy impact tests are conducted along with detailed microstructural and fractographic investigations, including SEM, EBSD, and XRD. The main findings are summarized below:

- The optimization of CFB microstructure, particularly γ_R, is essential for achieving optimal mechanical performance. The presence of MA islands and unstable γ_R regions along PAGBs negatively impacts fracture behavior, especially under localized deformation modes such as in Charpy impact and fatigue crack propagation tests.
- Under quasi-static tensile loading, CFB outperforms CBB, primarily due to the gradual transformation of γ_R to martensite, which enhances both strength and tensile ductility during uniformly distributed deformation at lower strain rates.
- In contrast, CBB demonstrates significantly higher impact toughness, characterized by clear ductile regions, while CFB tends to fail in a brittle manner. The existence of brittle MA islands and abrupt transformation of γ_R at higher strain rates, combined with a localized deformation, promotes a brittle network along the PAGBs, causing intergranular fracture or rapid debonding of PAGs through MA islands, causing cleavage fracture.
- Although CFB exhibits a considerably higher fatigue limit, it shows a faster fatigue crack propagation rate and a lower ΔK_{th} compared to CBB. In CBB, PAGBs effectively deflect fatigue cracks, while in CFB, the presence of MA islands and unstable γ_R weakens these boundaries, facilitating either intergranular crack growth through a brittle network along PAGBs or straight paths across PAGBs without deflection. When a crack propagates through a PAG, a ductile fracture behavior is observed rather than a cleavage fracture, highlighting the influence of the lower deformation rate relative to Charpy impact tests.

Fatigue & Fracture of Engineering Materials & Structures

WILEY

FFEMS Fatigue & Fracture of Engineering Materials & Structures

ORIGINAL ARTICLE OPEN ACCESS

Impact Toughness and Fatigue Crack Propagation in Carbide-Free Bainite: The Adverse Role of Retained Austenite and Martensite-Austenite Islands

Oguz Gulbay | Alexander Gramlich | Ulrich Krupp

Steel Institute, RWTH Aachen University, Aachen, Germany

Correspondence: Oguz Gulbay (oguz.guelbay@iehk.rwth-aachen.de)

Received: 28 February 2025 | **Revised:** 24 May 2025 | **Accepted:** 24 June 2025

Funding: The authors received no specific funding for this work.

Keywords: bainite | crack propagation | fracture | MA island | retained austenite | steel

ABSTRACT

The deformation behavior of carbide-bearing bainite (CBB) and carbide-free bainite (CFB) under various loading conditions is investigated. Retained austenite (RA) in CFB enhances strength and ductility only under uniaxial tension through gradual strain-induced martensitic transformation, yet deteriorates impact toughness and fatigue crack resistance. CBB, however, shows superior impact toughness and stronger resistance to crack propagation with effective fatigue crack deflection at prior austenite grain boundaries (PAGB). Martensite-austenite (MA) islands and unstable austenitic constituents induce intergranular fracture in CFB by forming a brittle network along the PAGBs when combined with localized deformation. Furthermore, weakened PAGBs fail to provide an effective barrier against transgranular fracture. In this case, rapid PAG debonding through MA islands leads to cleavage fracture in Charpy tests, whereas ductile fracture occurs in crack propagation tests. These results highlight the need to carefully design CFB microstructures, particularly RA, to achieve optimal mechanical performance for specific applications.

1 | Introduction

Improving the mechanical properties of steel alloys is important for enhancing the longevity and reliability of engineering components. Beyond engineering performance, this also contributes to environmental sustainability by promoting the circularity of the steel industry [1, 2]. Over the decades, different types of bainitic microstructures have drawn considerable research attention due to their promising properties and their low-cost alloying concepts [3, 4]. Modifications in chemical composition and process parameters significantly influence the microstructure of bainitic steels, which, in turn, substantially influence the performance of the steel. It is well known that the addition of ~1 wt% of Si suppresses the carbide precipitation, making the surplus carbon available for enrichment in surrounding austenite [5–7]. In this way, retained austenite is introduced to the microstructure as a secondary phase to form carbide-free bainite (CFB) as opposed to cementite in carbide-bearing bainite (CBB).

In CFB microstructures, RA exists primarily in two morphologies: nanoscale films that form between bainitic ferrite (BF) plates and blocky type that forms preferably on prior austenite grain boundaries (PAGB). Film-like RA is generally more stable due to its size and higher carbon content, which enhances its resistance to transformation under thermal or mechanical stress [5]. On the other hand, blocky RA tends to form in larger sizes with lower carbon contents, making it more susceptible to transformation, leading to martensite-austenite (MA) islands formation during cooling or under mechanical stress [8]. Therefore, they are often considered undesirable because they may negatively influence the mechanical properties.

Summary

- Performance of carbide-free bainite is contradictory under various loading conditions.
- This discrepancy originates from austenite's response to changed deformation mechanisms.
- Stability, morphology, and distribution of austenite influence fracture behavior greatly.
- The crack/PAG-boundary angle alters the crack path near unstable austenitic constituents.

The primary advantage of RA in CFB is the martensitic transformation due to the transformation-induced plasticity (TRIP) effect under mechanical loading. This mechanism results in exceptional quasistatic tensile properties due to pronounced strain hardening, leading to a well-balanced ultimate tensile strength (UTS) and elongation [9, 10]. Consequently, CFB alloys outperform conventional CBB alloys in quasistatic tensile properties [11, 12] and achieve comparable results to high-strength steels, such as tempered-martensite based steels, without a substantial loss in strength [5]. However, under fatigue loading, the influence of RA is rather complicated. It has been reported that RA can be beneficial by transforming into martensite at the crack tip, thereby absorbing the energy for crack propagation and decelerating the progression of fatigue cracks. Conversely, the existence of unstable blocky RA and MA islands can be detrimental. Gao et al. [13] showed that film-like RA between BF plates arrests the fatigue crack via martensitic transformation, whereas MA island and blocky RA on PAGBs cause intergranular fracture, deteriorating the fatigue properties. Similarly, although the existence of RA can improve the impact toughness through the TRIP effect, it has also been stated that the existence of MA islands and unstable blocky RA can lead to brittle fracture [14–16]. Therefore, the stability, fraction, size, morphology, and location of these microstructural constituents in bainitic applications strongly influence the mechanical performance; thus, the microstructure optimization for the intended application becomes crucial.

Although tensile tests are widely used to assess the performance of bainitic steels, a broader understanding of their mechanical performance requires testing under various loading conditions, especially for complex microstructures like CFB. This study builds upon previous work [12] in which the uniaxial tensile behavior and fatigue limit of the same material conditions were studied. In contrast to earlier investigations, the present work expands the scope by incorporating Charpy impact testing and bending fatigue crack propagation experiments to assess mechanical response at different loading conditions. Moreover, the experimental findings are supported by thorough microstructural and fractographic examinations. By including these additional investigations, a more comprehensive understanding of how retained austenite and MA islands influence the fracture behavior is provided. In this way, it is aimed to establish a broader range of service-relevant conditions by enabling a more detailed understanding of the microstructure-performance relationships in CFB microstructures.

2 | Materials and Methods

Two steel ingots (80 kg each) with nominal compositions of Fe-0.2C-2.5Mn and Fe-0.2C-2.5Mn-1.5Si (wt%) were produced using a laboratory-scale vacuum induction furnace. The $140\times140\,mm^2$ ingots were homogenized at 1200°C and forged down to $60\times60\,mm^2$ billets. Following this, a second homogenization at 1200°C for 5 h was carried out, followed by furnace cooling. The chemical compositions of the alloys, as measured by optical emission spectroscopy (OES), are presented in Table 1, with carbon content determined via combustion analysis. The addition of 1.5 wt% Si to the second alloy was intended to inhibit cementite precipitation during the bainitic transformation. Hence, the first alloy was designed to produce carbide-bearing bainite (CBB), whereas the second alloy was designed to produce carbide-free bainite (CFB). Accordingly, the first alloy was denoted as CBB, whereas the second was denoted as CFB. In order to generate bainitic microstructures, an isothermal heat treatment was conducted in a salt bath at 400°C for 45 min after austenitization for both alloys. The isothermal heat treatments were conducted above the martensite start temperature (M_s), which was determined as 384°C and 374°C for CBB and CFB, respectively. The graphical representation of heat treatment is shown in Figure 1a. Initial investigations on microstructure and mechanical properties have been published in previous works, which were conducted with the same materials and the same chemical compositions [12, 17].

Uniaxial tensile tests were conducted using B5×25 cylindrical tensile specimens with a gauge diameter of 5 mm and a gauge length of 25 mm. The tests were performed at room temperature on a ZWICKROELL Z100 universal electromechanical testing machine (ZwickRoell GmbH & Co. KG, Germany) at a strain rate of $10^{-3}\,s^{-1}$. Three tensile specimens were tested for each condition. Charpy impact tests were carried out on a 300-J instrumented Charpy impact test machine using standard V-notched $10\times10\times55\,mm^3$ specimens. For each material state, three tests were performed at room temperature.

Crack propagation tests were performed on a RUMUL CRACKTRONIC (Russenberger Prüfmachinen AG, Switzerland) resonance testing machine at a stress ratio of $R=-1$. For the tests, single-edge notched bend (SENB) specimens were used. The specimen geometry is shown in Figure 1b. Before performing each test, a precrack was introduced into the specimen with a length of

TABLE 1 | Chemical composition of the studied alloys in wt%.

Alloy	C	Mn	Si	Al	P	S	Cr	Mo
CBB	0.18	2.48	0.01	0.002	0.003	0.002	0.04	0.01
CFB	0.19	2.38	1.48	0.003	0.003	0.003	0.04	0.01

approximately 1.3 mm by cyclic loading with stepwise reduction of the bending moment to ensure a small plastic zone at the crack tip. The threshold value of the stress intensity factor (SIF) range (ΔK_{th}) for technical crack propagation was determined using the load-shedding procedure. Following ISO 12108 [18], the SIF range (ΔK) was gradually reduced until no technically relevant crack growth was observed (multiple data points with a linear regression between da/dN < 10^{-11} m/cycle and da/dN < 10^{-10} m/cycle). Lastly, the stable crack propagation was monitored at a constant bending moment to observe crack propagation behavior in the Paris regime of the log da/dN versus log ΔK curve [18].

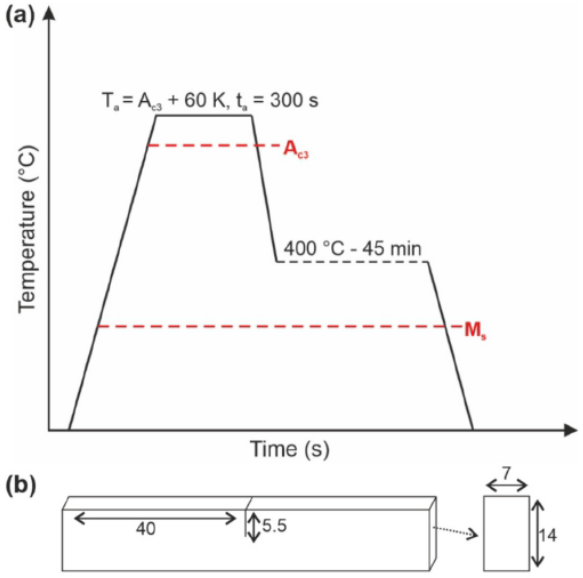

FIGURE 1 | (a) Graphical representation of heat treatment. (b) Specimen geometry of the single edge notch bend (SENB) specimen. Dimensions are given in mm. [Colour figure can be viewed at wileyonlinelibrary.com]

Microstructural and fractographic analyses were conducted using a field-emission gun ZEISS SIGMA SEM (Carl Zeiss Microscopy GmbH, Germany) with a secondary electron (SE) detector. Specimen preparation for microstructural examinations involved mechanical grinding with SiC abrasive paper up to 1200 grit, followed by polishing using diamond paste with particle sizes of 6 and 1 µm, respectively. The polished specimens were then etched with 3% HNO_3 (Nital) to reveal the microstructure. For electron backscatter diffraction (EBSD) analysis, the specimens underwent a final surface polishing with oxide polishing suspension (OPS) for 20 min after the final mechanical polishing step. The EBSD measurements were conducted using a NORDLYS NANO detector (Oxford Instruments, Great Britain) with a 75-µm aperture, an accelerating voltage of 20 kV, a working distance of 17 mm, and a step size of 75 nm. Quantitative X-ray diffraction (XRD) was used to determine the retained austenite (RA) fractions in the CFB alloys. Measurements were performed using a Stresstech Xstress G3 diffractometer with a Cr source, operating at 30 kV and 8 mA.

3 | Results

The achieved SEM images of CBB and CFB alloys after isothermal heat treatment are shown in Figure 2. The microstructure of CBB alloy is composed of bainitic ferrite (BF) as the primary phase and cementite as the secondary phase (cf. Figure 2a). In the case of CFB, it was observed that cementite precipitation was suppressed by Si alloying, as intended. The microstructure mainly consisted of plate-like BF and retained austenite (RA) films between BF plates. RA formation was not only detected between the BF plates but also on prior austenite grain (PAG) boundaries with different morphological features, such as blocky and elongated. Moreover, big blocky martensite-austenite (MA) island formations were detected in

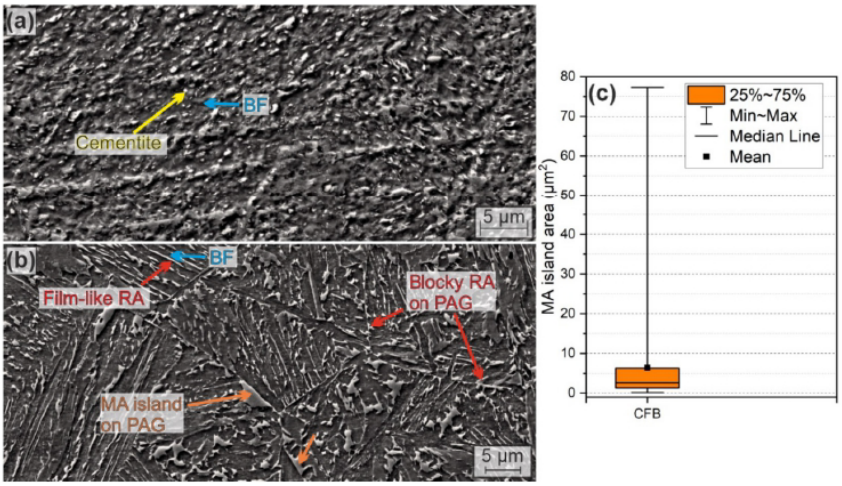

FIGURE 2 | SEM images of (a) CBB and (b) CFB alloys. Images were acquired from an undeformed state. (c) Statistical evaluation of MA islands, showing the minimum and maximum values, mean, median, and interquartile range (25th–75th percentile). [Colour figure can be viewed at wileyonlinelibrary.com]

addition to RA as a secondary phase (Figure 2b). The statistical evaluation of the MA island size in CFB steel, based on 250 individual measurements, is displayed in Figure 2c. The average MA island area was determined as 6.4 μm², whereas minima and maxima exhibited a significant difference between 0.1 and 77.3 μm², indicating an inhomogeneous size distribution of MA islands in the microstructure. Furthermore, the area fraction of the MA islands was determined to be 10.3% (cf. Table 2). The majority of the MA islands were located on or near the PAG boundaries, as highlighted in Figure 2b, although some were observed within the PAG interiors. Additionally, it is important to note that the PAG sizes of CBB and CFB were measured to be approximately 54 and 60 μm, respectively, indicating that both alloys exhibit comparable PAG sizes.

Engineering stress–strain curves of the studied alloys are displayed in Figure 3a. Both alloys show continuous yielding behavior and uniform plastic deformation; however, the CFB alloy exhibited superior tensile properties to the CBB alloy, with a relative increase from 738 to 765 and from 866 to 1134 MPa for yield strength (YS) and ultimate tensile strength (UTS), respectively. Uniform elongation (UE) as well as total elongation increased from 4.2% to 11.6% and 13.4% to 19.4% (cf. Table 3). Additionally, EBSD measurements were accomplished before and after tensile testing to examine the RA behavior during deformation. Figure 3b,c displays the band contrast maps superimposed with the RA phase before and after the tensile test, respectively. It is displayed that only a trace amount of RA was detected after deformation, unlike the undeformed state. The RA fractions obtained via XRD supported these findings, exhibiting 6.1% before deformation and 0.5% after deformation (cf. Table 2).

Contrary to the improved ductility during tensile tests, the impact toughness of CFB was significantly lower than that of CBB, with an impact energy of 52.5 and 10.3 J for CBB and CFB, respectively (cf. Table 3). The fracture surfaces reveal that the CBB alloy exhibited a significant amount of ductile fracture features, mainly at the subnotch area and edges of the specimen (cf. Figure 4a,b), where small dimple areas are visible. When the subnotch area was surpassed, the fracture mode changed to transgranular cleavage surrounded by ductile dimpled regions at the edges of the facets (cf. Figure 5a). In alignment, the maximum force of ~15.5 kN was reached gradually (cf. Figure 5c), indicating plastic deformation rather than sudden brittle fracture. In contrast, the fracture surface of CFB was dominated by brittle fracture characteristics with intergranular and cleavage fracture

TABLE 2 | Area fraction and average size of the MA islands and volume fraction of retained austenite before and after tensile deformation (via XRD) in CFB steel.

MA islands (area fraction)	MA islands (average area)	Retained austenite (before deformation)	Retained austenite (after deformation)
10.3%	6.4 μm²	6.1%	0.5%

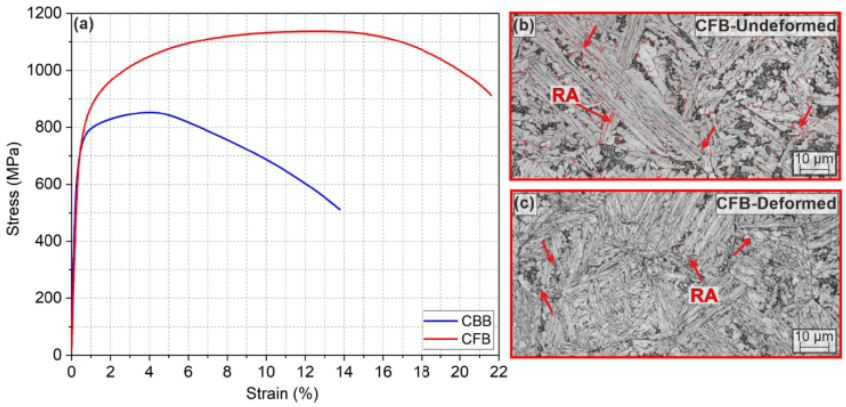

FIGURE 3 | (a) Engineering stress–strain curves of the studied alloys. The EBSD band contrast map, superimposed with the retained austenite phase of CFB alloy (b) before deformation and (c) after deformation. [Colour figure can be viewed at wileyonlinelibrary.com]

TABLE 3 | Quasistatic tensile properties, impact toughness, fatigue limit, ΔK_{th}, m, and C of CBB and CFB alloys.

Material state	YS (MPa)	UTS (MPa)	UE (%)	TE (%)	Impact en. (J)	Fatigue lim. (MPa)	ΔK_{th} (MPa√m)	m	C [10^{-12}]
CBB	738∓13	866∓12	4.2∓0.7	13.4∓0.6	52.5∓4.5	343	14.80	2.84	0.24
CFB	765∓5	1134∓4	11.6∓0.6	19.4∓0.2	10.3∓0.5	495	12.55	2.98	0.81

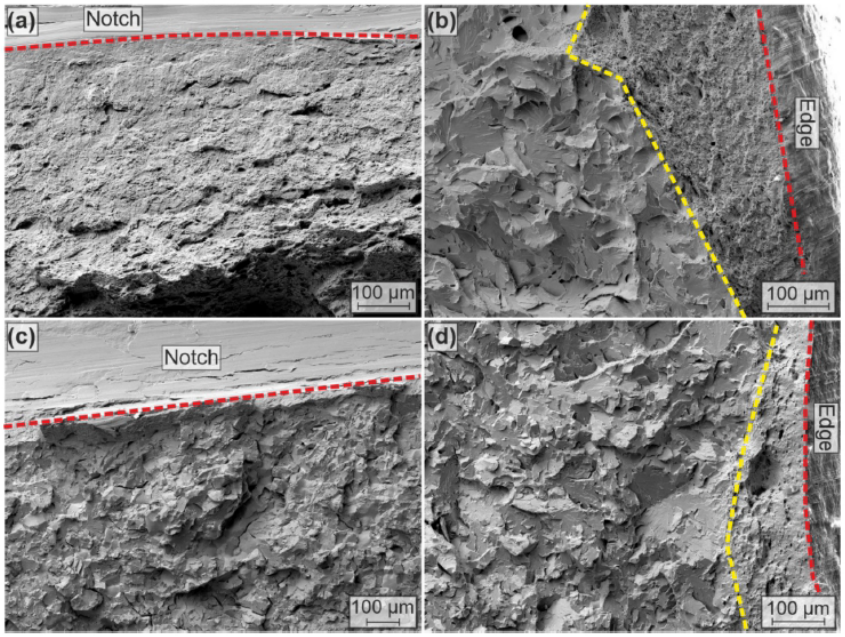

FIGURE 4 | Fracture surface images of (a, b) CBB and (c, d) CFB acquired from Charpy impact test specimens. (a, c) Images taken from the sub-notch area and (b, d) images taken from the edge of the specimens. [Colour figure can be viewed at wileyonlinelibrary.com]

(cf. Figure 4c,d and Figure 5b). Small amounts of ductile fracture dimples at the edges of the specimen were also observed (cf. Figure 4d). The magnified fractography of CFB in Figure 5b shows the grains that were revealed after an intergranular fracture. These results are also reflected in the force-displacement curve of the CFB alloy by brittle failure after the maximum load of 14 kN. Additionally, the integral of the force-displacement curves in Figure 5c shows the clear difference in the values obtained for impact toughness.

The fatigue limit of these alloys has already been determined in a previous study [12] by the staircase testing method using the Dixon and Mood [19] equation. It was revealed that the fatigue limit of CFB is ~150 MPa higher than that of CBB, which is also shown in Table 3. To amend the uniaxial fatigue testing, crack propagation tests were carried out in this study to investigate the crack propagation behavior via resonance bending fatigue experiments. The results of the crack propagation tests are displayed in Figure 6a. Contrary to the fatigue limits, CFB showed a slightly lower threshold SIF range by $\Delta K_{th} = 12.55\,\mathrm{MPa}\sqrt{\mathrm{m}}$, whereas CBB showed $\Delta K_{th} = 14.80\,\mathrm{MPa}\sqrt{\mathrm{m}}$. Moreover, CFB exhibited a faster crack propagation rate in the stable crack growth region. This was reflected in the parameters of the Paris line of CFB as a slightly higher slope m of 2.98 and a higher constant C of 0.81×10^{-12}, whereas the slope m was 2.84, and the constant C was 0.24×10^{-12} in CBB (cf. Table 3). It is worth mentioning that more data scattering occurred during stable crack growth of CFB. Furthermore, the determined fatigue limit and ΔK_{th} values of the studied alloys were used to draw the Kitagawa–Takahashi diagram [20], with El-Haddad modification [21], as presented in Figure 6b. Thereby, the curves represent the region of nonpropagating cracks. Accordingly, the combined results reveal a larger safe zone for CFB alloy, although it has poorer crack propagation characteristics.

The fracture surfaces, acquired from different phases of the crack propagation curve, are shown in Figure 7. As highlighted in Figure 6a, the crack propagation curves are divided into three phases to highlight the fracture surface characteristics in more detail. In the case of CBB, it mostly exhibited ductile fracture characteristics during the whole experiment. In Phases 1 and 2, only ductile fracture behavior with clear fatigue striations was detected, as shown, respectively, in Figure 7a,b. In Phase 3, close to the end of the crack propagation test, some brittle fracture characteristics were formed in addition to ductile behavior, as highlighted in Figure 7c. In this phase, the data scattering was also increased, as shown in Figure 6a. In the case of CFB, the fracture surface exhibited characteristics of brittle and ductile behavior in combination. In Phases 1 and 3, brittle fracture behavior surfaced as a distinct intergranular fracture through the PAGBs (highlighted in Figure 7d,f), whereas ductile fracture characteristics were observed by ductile tearing bainitic blocks containing the morphology of parallel BF plates (cf. Figure 7d,f). In these regions, fatigue striations were also detected, which is a unique feature of ductile fatigue crack propagation behavior. In Phase 2, where the transition occurred before the stable crack propagation region, a plateau formed, as highlighted in Figure 6a. During this phase, only ductile fracture behavior with similar characteristics as the ductile regions in Phases 1 and 2 was monitored (cf. Figure 7e).

In Figure 8, the SEM images and inverse pole figure (IPF) maps of CBB and CFB alloys acquired from the cracked surface perpendicular to the fracture surface are shown. It can be seen that the fatigue crack was effectively deflected by the PAGBs in CBB (cf. Figure 8a). This is also shown in the inverse pole figure (IPF) map of the CBB alloy in Figure 8c more clearly, where the crack was successfully deflected when there was a change in orientation, such as PAG and/or block boundaries.

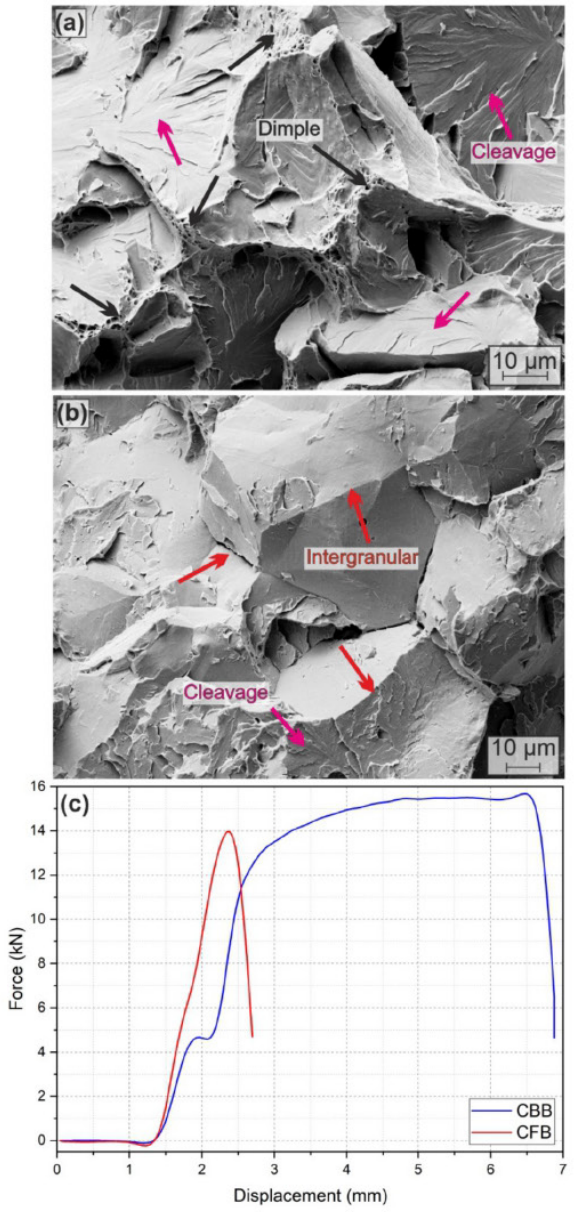

FIGURE 5 | Fracture surface images of (a) CBB and (b) CFB acquired from Charpy impact test specimens. (c) Force-displacement curves of the studied alloys from the Charpy impact test. [Colour figure can be viewed at wileyonlinelibrary.com]

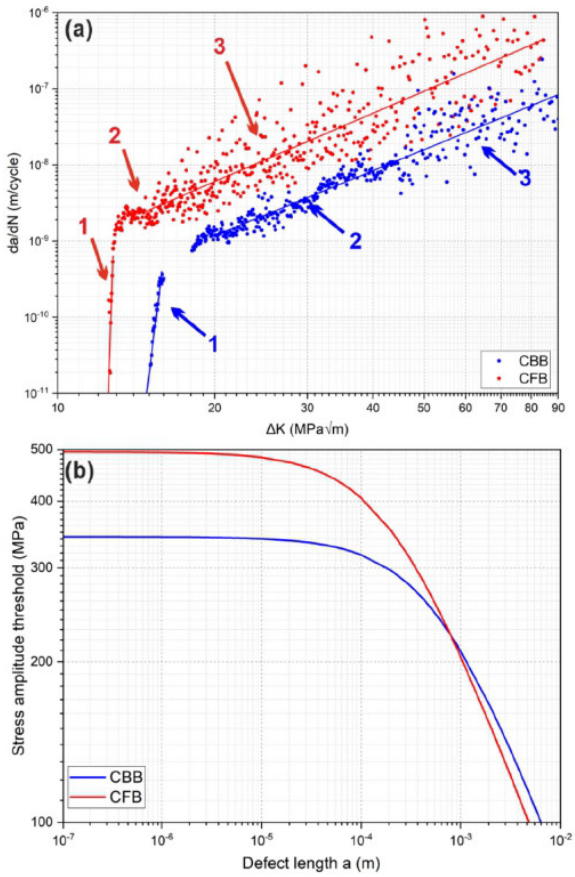

FIGURE 6 | (a) Crack propagation curves and (b) Kitagawa–Takahashi diagram within 10^7 cycles (with El-Haddad modification) of CBB and CFB alloys. Crack propagation curves are divided into three phases to explain the fracture surfaces obtained from the specimens. [Colour figure can be viewed at wileyonlinelibrary.com]

In addition to that, Figure 8b shows the crack deflection possibly on cementite particles, whereas it is also possible that crack deflection might have occurred on a packet/block boundary. However, in the case of CFB, the PAGBs were not effective in deflecting or decelerating the fatigue crack; instead, intergranular and transgranular cracking were observed as in Charpy impact specimens. In Figure 8d, the PAGBs are highlighted along with the MA islands and RA constituents on the boundaries. It can be seen that the propagating crack (in the PAG) coincides with an MA island on a PAGB (Point 1) and continues propagating, causing intergranular fracture until it changes its path (Point 2). Nevertheless, this does not mean that every interaction between the crack and the MA islands causes intergranular fracture during crack propagation tests. As displayed in Figure 8d, the crack leaves the PAGB and enters the adjacent PAG through an MA island (Point 2) with no deflection, causing transgranular fracture. This is shown more clearly in Figure 8e where multiple PAGBs were surpassed with no interference. The IPF map of FCB in Figure 8f supports these findings as well by showing no deflection at the PAGB. Rivetingly, when a PAGB is surpassed transgranularly, instead of a brittle cleavage fracture as in Charpy impact tests, a ductile fracture mechanism was induced.

To explore the crack-PAGB interaction in CFB, the angles between crack paths and PAGBs were further examined. As shown in Figure 8d, the crack propagated along an intergranular path when the angle between the crack and PAGB was relatively large. In contrast, in Figure 8e, the crack cut through the PAGB and propagated on a transgranular path at a smaller angle. Based on these observations, a semiquantitative analysis was conducted to better understand the influence of crack-PAGB geometry on the cracking mechanism in CFB. To this end, the angle between

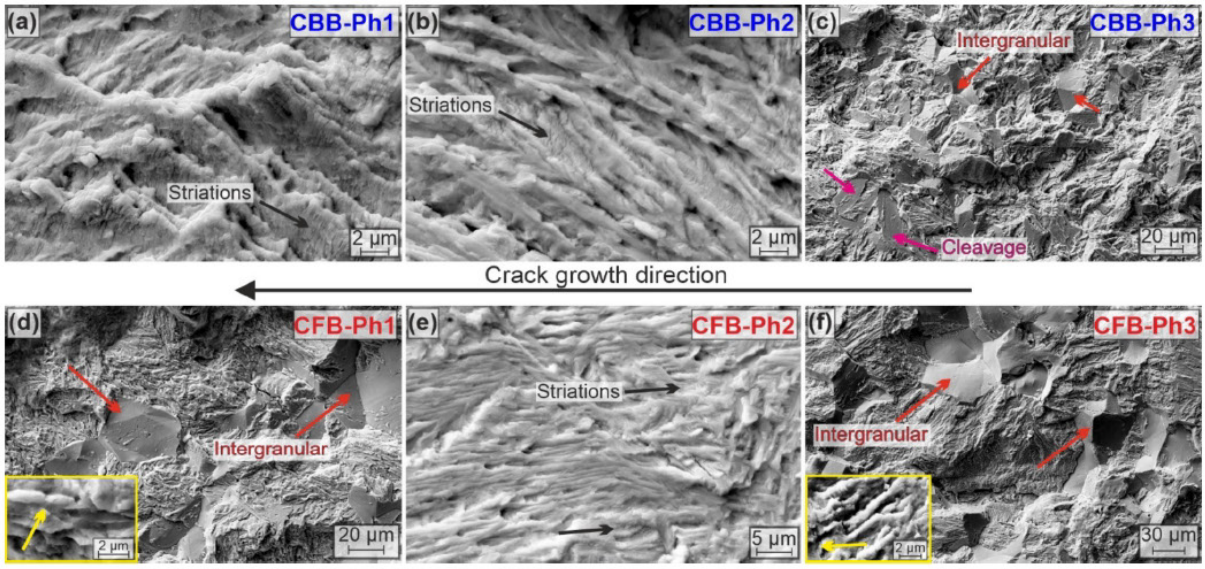

FIGURE 7 | Fracture surface images of (a–c) CBB and (d–f) CFB acquired from crack propagation test specimens. The numbers indicate phases in crack propagation curves. [Colour figure can be viewed at wileyonlinelibrary.com]

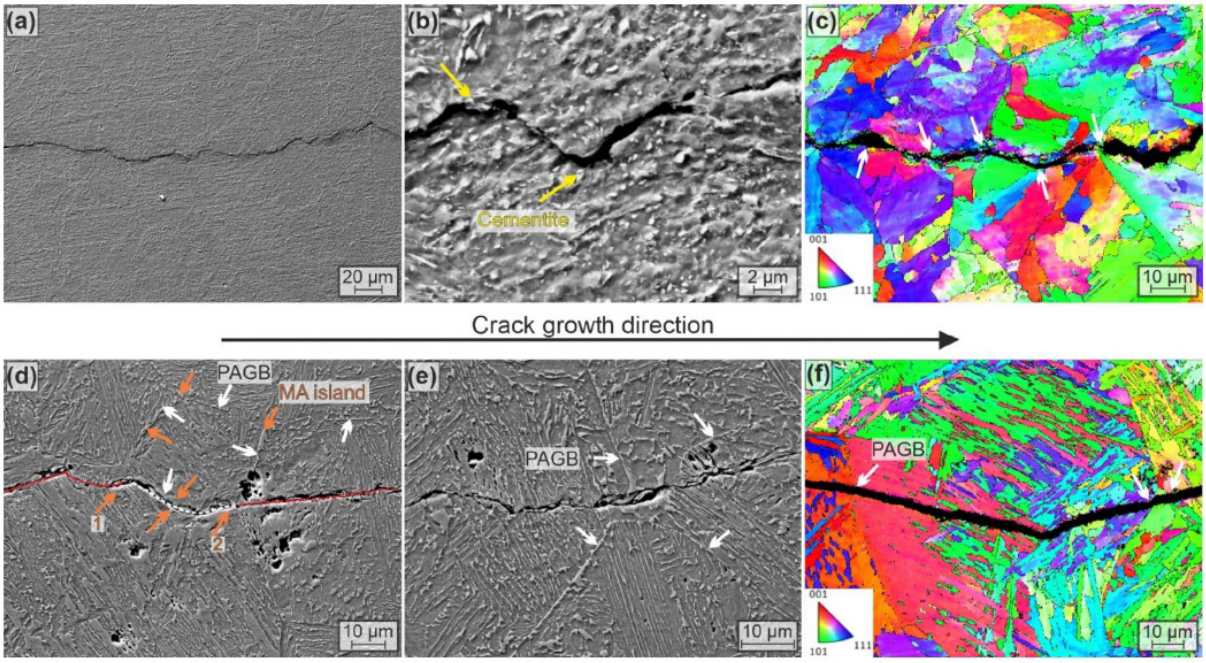

FIGURE 8 | SEM images and inverse pole figure (IPF) maps of (a–c) CBB and (d–f) CFB alloys acquired from the cracked surface perpendicular to the fracture surface. The images were taken from the stable crack growth region. [Colour figure can be viewed at wileyonlinelibrary.com]

the crack and PAGBs was measured at multiple crack-boundary interaction sites. Figure 9 presents the statistical distribution of the measured angles, categorized by crack path. The average angle for intergranular crack propagation was relatively higher, averaging 132°, whereas transgranular cracks occurred at a lower angle of 103°. To provide a standardized interpretation of these results, it can be summarized that intergranular cracks predominantly formed when the angle between the propagating crack and PAGB was above 120°, whereas transgranular cracks were more frequently observed at angles below this threshold.

4 | Discussion

The comparison of the investigated bainitic alloys showed that the deformation behavior of the bainitic steels significantly

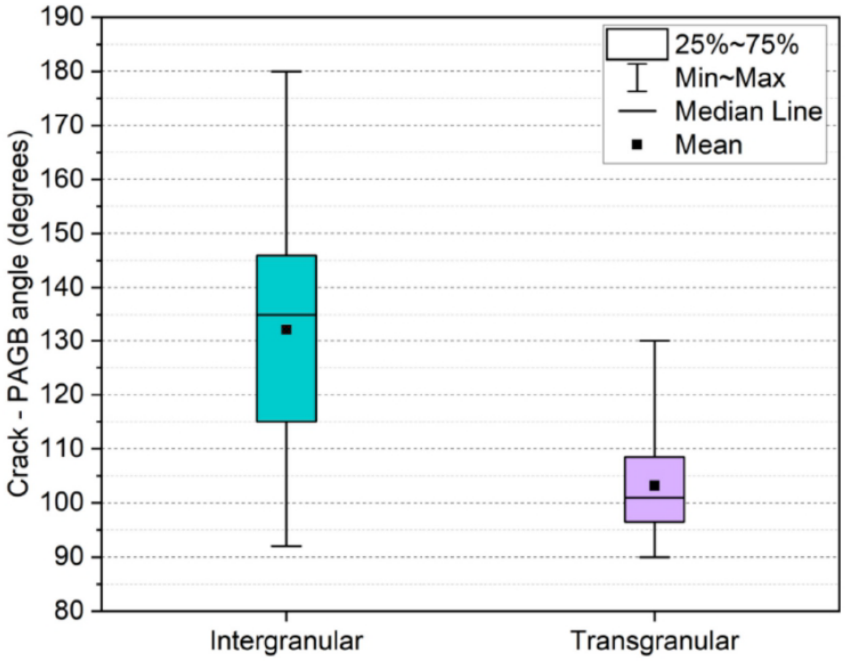

FIGURE 9 | Statistical distribution of the angles between the propagating crack and PAGBs for intergranular and transgranular crack paths in CFB. The plot shows the minimum and maximum values, mean, median, and interquartile range (25th–75th percentile). [Colour figure can be viewed at wileyonlinelibrary.com]

depends on the deformation mechanism, which in turn is controlled by the microstructural constituents. Many studies have shown that the existence of RA as the secondary phase instead of cementite improves the quasistatic tensile properties of bainitic steels [9, 10], which was confirmed by our investigations (cf. Figure 3a and Table 3). The lattice resistance of the face-centered cubic (FCC) RA phase is lower than that of the body-centered cubic (BCC) BF phase, which can additionally facilitate more dislocation motion. Hence, plasticity is improved [11]. Contrariwise, the CFB alloy achieved very low impact toughness values, showing a combination of transgranular and intergranular fracture (cf. Figures 4c,d and 5b), whereas the CBB alloy reached substantially higher impact toughness values with a considerable amount of ductile areas in the fracture surface (cf. Figures 4a,b and 5a). It was shown in multiple studies that the MA islands, which formed on PAGBs, could result in a loss of impact toughness [14, 22–26]. When austenite transforms to martensite during cooling (forming MA islands), a certain volume expansion occurs due to the nature of this transformation. As a result of this, the stress concentration in the surrounding bainitic matrix can increase, assisting the cleavage fracture [22]. In addition to that, the hardness of the MA islands is significantly higher than the surrounding bainite, causing a stress concentration in the adjacent matrix. During loading, a large stress could be generated at the interface of MA islands and matrix, which results in the debonding of MA constituents from PAGB boundaries, leading to cleavage fracture. Moreover, the MA islands are naturally brittle, and this increases the stress concentration at the PAGB. As a result, PAGBs may weaken and act as initiation sites for cracks and/or promote crack propagation [25]. Another reason behind the change in the fracture mode could be the change in the transformation rate of RA to martensite in different tests. In uniaxial tensile tests, due to lower strain rate and uniform deformation, the RA austenite gradually transforms to martensite, leading to enhanced elongation and high UTS values [27]. With an increased strain rate, localized deformation, and multiaxial stress state in the Charpy impact test, the RA transforms to martensite faster at the crack tip. The MA islands and RA along the PAGB boundaries continuously transform to martensite at the crack tip, forming a brittle network. This could cause a path for brittle crack propagation through PAGB, leading to intergranular debonding [27]. On the other hand, CBB exhibited a significant amount of ductile regions with no indication of intergranular fracture. Therefore, it can be concluded that cementite precipitation did not compromise PAGBs, which may have led to additional brittleness as in CFB. Furthermore, cementite particles may have prevented the continuous crack paths by deflecting the crack. In literature, it was also mentioned that cementite particles may promote microvoid formation and coalescence, leading to ductile fracture modes [28].

The fatigue limit of CFB is significantly higher than that of CBB (cf. Table 3), which is in good agreement with the quasistatic tensile properties, confirming the well-known relationship between the UTS of metallic materials and their fatigue limit [29, 30]. The fatigue limit of the materials is more related to the crack initiation phase, which can take a long time, especially under high-cycle fatigue regimes. To generate this, the fatigue tests to determine the fatigue limit were conducted in the absence of a notch, in a polished "crack-free" condition. The materials with higher UTS require higher stresses to nucleate and grow persistent slip bands to form a crack. Therefore, the higher

fatigue limit of CFB can be attributed to its significantly higher UTS compared to CBB.

On the other hand, based on previous investigations [12] and literature data [11, 31], it can be said that unexpected results were obtained from crack propagation tests of CFB by exhibiting poorer crack propagation characteristics than CBB (cf. Table 3). In normal circumstances, PAG and block boundaries are effective microstructural barriers to deflect the propagating fatigue crack due to their highly misoriented nature [32]. The crack path of CBB alloy revealed that the existence of brittle cementite did not compromise the effect of high-angle boundaries during crack propagation. As presented in Figure 8, the crack was effectively deflected at these boundaries, indicating that the fatigue crack growth is mainly controlled by PAG, packet, and block boundaries in CBB. Additionally, it was mentioned that cementite plates can be strong barriers to fatigue cracks under cyclic loading and slow down fatigue crack growth [33, 34]. The fracture surfaces in Figure 7a–c strengthen this statement by showing ductile characteristics with fatigue striations. Moreover, the SEM images acquired perpendicular to the fracture surface reveal the small deflections at cementite precipitates, as shown in Figure 8b.

On the other hand, these boundaries, particularly PAGBs, were not effective in the case of CFB and either caused an intergranular fracture or a transgranular cracking of PAGB without deflection (cf. Figure 8d–f). Gao et al. [13] stated that MA islands and blocky RA, which are located at the PAGBs, may induce intergranular fatigue cracking due to the slip impingement effect. The RA phase (FCC) has more slip systems compared to the BF phase (BCC). It was accordingly stated that on the slip impingement, where MA islands and/or unstable blocky RA exist in adjacent PAGs, the activation of the preferred slip plane becomes easier, leading to intergranular fatigue cracking [13]. As the threshold SIF range, ΔK_{th}, is primarily associated with the crack propagation resistance of the microstructure against existing cracks. Accordingly, to determine ΔK_{th}, the bending fatigue experiments were performed using SENB specimens with precracks deliberately introduced at the notch roots. The higher ΔK_{th} of CBB can be attributed to pure ductile fracturing behavior in phases 1 (cf. Figure 7a). However, CFB has more brittle behavior during Phase 1 with intergranular fracture due to the existence of MA islands and low-stable austenitic constituents on PAGBs (cf. Figure 7d), leading to deterioration of ΔK_{th}.

Furthermore, in the event of transgranular cracking through PAGBs with no deflection, a ductile fracture mechanism was induced, unlike in Charpy impact tests. This suggests that the deformation rate was not sufficient to debond the whole grain during crack propagation tests, although the PAGBs became brittle enough to be surpassed due to MA islands and low-stable austenitic constituents. Therefore, a ductile fracture was observed when the fatigue crack passed through the PAGBs. In addition to that, when the crack propagation curves are compared, there is more data scattering observed in the stable crack growth region of CFB (cf. Figure 6a). In the case of CBB, at higher ΔK values, the data started to scatter as well (Phase 3 of the stable crack propagation region, highlighted in Figure 6a). In this region, some cleavage and intergranular fractures also occurred in CBB (cf. Figure 7c). Therefore, the reason behind the data scattering could be the manifestation of both brittle and ductile fractures during the loading.

The results show that the PAGBs in CFB are weakened in the vicinity of the MA islands, and low-stable austenitic constituents, leading to brittleness and reducing the effectiveness of these boundaries against propagating cracks (cf. Figure 8a–c). Besides, it is also crucial to understand the mechanism governing the crack path during loading, especially for improved microstructure optimization. The analysis suggests that the angle between the propagating crack and PAGBs influences the crack path in the CFB microstructure (cf. Figure 9), with intergranular cracks forming at angles of 120° or greater, whereas transgranular cracks occurred primarily at angles below 120°. This possible scenario is illustrated in Figure 10, which shows the tendency of cracks to follow an intergranular path along PAGBs through a brittle necklace formed by MA islands and austenitic constituents with a large crack-boundary angle encounter.

In the literature, metastable RA is mostly known to improve fatigue properties of high-strength steels by transforming to martensite due to the TRIP effect caused by the plastic deformation at the crack tip [11, 35–38]. Due to the phase transformation and formation of compressive stresses, the energy of the crack is absorbed, and thus, the crack can be decelerated or deflected. However, the current study shows that this is not straightforward for RA-containing bainitic microstructures. Based on the results, it can be concluded that the reason for obtaining poor crack propagation characteristics in CFB alloy, despite the higher UTS and fatigue limit, is probably due to the weakened nature of PAGBs, easing the fatigue crack to propagate. This points out the detrimental nature of the MA island and unstable RA phases on PAGBs. In the meantime, observing ductile regions confirms the plasticity during deformation and the beneficial features of BF plates and RA films in the CFB microstructure. It is well known that film-like RA is mechanically more stable compared to blocky RA and MA islands [5]. This means that in the case of plastic deformation and, consequently, the occurrence of martensitic transformation in front of a crack tip, parallelly aligned RA films between BF plates in PAGs will

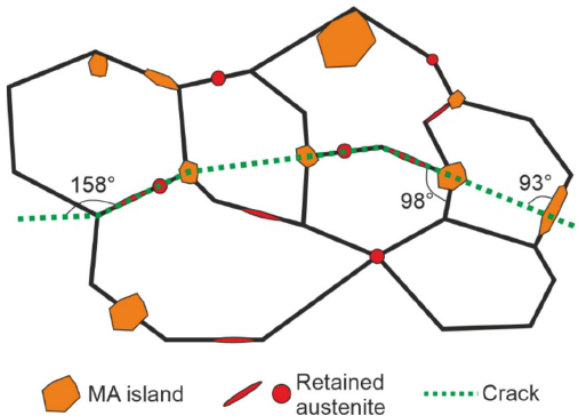

FIGURE 10 | Schematic illustration of the fracture mechanism in CFB alloy. [Colour figure can be viewed at wileyonlinelibrary.com]

consume more energy than significantly metastable MA islands or austenitic constituents on PAGBs. This points out that with microstructure optimization through adjustments in chemical composition and processing, the formation, size, and fraction of MA islands and unstable austenitic constituents (especially on PAGBs) can be reduced, the stability of austenite can be optimized, and the brittle behavior during crack propagation can be minimized.

5 | Conclusion

The deformation behavior of carbide-bearing (CBB) and carbide-free bainite (CFB) was investigated under different loading conditions. To achieve this, uniaxial tensile, fatigue crack propagation, and instrumented Charpy impact tests, along with thorough microstructural and fractographic investigations, were employed. The following conclusions can be drawn.

1. The optimization of microstructure, especially retained austenite (RA), in CFB is critical to achieve optimum mechanical performance under varying loading conditions. The formation of martensite-austenite (MA) islands and unstable austenitic constituents at prior austenite grain boundaries (PAGB) has a detrimental effect on fracture behavior when deformation progression is localized, as in Charpy impact and fatigue crack propagation tests.
2. CFB outperforms CBB in quasistatic tensile properties mainly due to the gradual transformation of RA to martensite, which improves ductility and strength during uniformly distributed deformation at lower strain rates.
3. CBB shows significantly higher impact toughness, with notable ductile regions in the fracture surface, whereas CFB exhibits brittle behavior. The existence of brittle MA islands and sudden transformation of RA at higher strain rates, combined with a localized deformation mechanism, promotes a brittle network along the PAGBs, causing intergranular fracture or rapid debonding of PAGs through MA islands, causing cleavage fracture.
4. Despite the higher fatigue limit, CFB shows a higher fatigue crack propagation rate and lower threshold of stress intensity factor range ΔK_{th} than CBB. Although PAGBs in CBB successfully deflect the fatigue cracks, MA islands and unstable austenitic constituents in CFB weaken these boundaries, resulting in intergranular fractures through the brittle network or cracks that cut PAGBs without deflection. However, ductile fracture behavior is observed when the crack goes through a PAG instead of cleavage fracture, highlighting the influence of a lower deformation rate compared to Charpy impact tests.

In summary, the comparison of the investigated bainitic steel concepts reveals that the most desirable microstructure for bainite is not trivial to define. Although the majority of the studies refer to the benefits of austenite-containing bainitic steels, the drawbacks concerning Charpy impact toughness and fatigue crack propagation characteristics need to be considered in dependence on the intended application.

Acknowledgments

The authors would like to thank Dr. Marion Kreins for the fruitful discussions. Open Access funding enabled and organized by Projekt DEAL.

Conflicts of Interest

The authors declare no conflicts of interest.

Data Availability Statement

The data that support the findings of this study are available from the corresponding author upon reasonable request.

References

1. A. Gramlich, W. Hagedorn, K. Greiff, and U. Krupp, "Air Cooling Martensites—The Future of Carbon Neutral Steel Forgings?," *Advanced Engineering Materials* 25 (2023): 2201931.

2. W. Hagedorn, A. Gramlich, K. Greiff, and U. Krupp, "Alloy and Process Design of Forging Steels for Better Environmental Performance," *Sustainable Materials and Technologies* 34 (2022): e00509.

3. C. Hofer, F. Winkelhofer, H. Clemens, and S. Primig, "Morphology Change of Retained Austenite During Austempering of Carbide-Free Bainitic Steel," *Materials Science and Engineering A* 664 (2016): 236–246.

4. K. Wang, Z. Tan, G. Gao, et al., "Microstructure-Property Relationship in Bainitic Steel: The Effect of Austempering," *Materials Science and Engineering A* 675 (2016): 120–127.

5. H. K. D. H. Bhadeshia and D. V. Edmonds, "Bainite in Silicon Steels: New Composition–Property Approach Part 1," *Metal Science* 17 (1983): 411–419.

6. F. G. Caballero, H. Roelofs, S. Hasler, et al., "Influence of Bainite Morphology on Impact Toughness of Continuously Cooled Cementite Free Bainitic Steels," *Materials Science and Technology* 28 (2012): 95–102.

7. E. Kozeschnik and H. K. D. H. Bhadeshia, "Influence of Silicon on Cementite Precipitation in Steels," *Materials Science and Technology* 24 (2008): 343–347.

8. F. G. Caballero, C. GarcíA-Mateo, J. Chao, M. J. Santofimia, C. Capdevila, and C. G. de Andrés, "Effects of Morphology and Stability of Retained Austenite on the Ductility of TRIP-Aided Bainitic Steels," *ISIJ International* 48 (2008): 1256–1262.

9. C. Hofer, S. Primig, H. Clemens, F. Winkelhofer, and R. Schnitzer, "Influence of Heat Treatment on Microstructure Stability and Mechanical Properties of a Carbide-Free Bainitic Steel," *Advanced Engineering Materials* 19 (2017): 1600658.

10. C. Garcia-Mateo and F. G. Caballero, "The Role of Retained Austenite on Tensile Properties of Steels With Bainitic Microstructures," *Materials Transactions* 46 (2005): 1839–1846.

11. X. Long, F. Zhang, Z. Yang, and B. Lv, "Study on Microstructures and Properties of Carbide-Free and Carbide-Bearing Bainitic Steels," *Materials Science and Engineering A* 715 (2018): 10–16.

12. O. Gulbay, M. Ackermann, A. Gramlich, A. R. Durmaz, I. Steinbach, and U. Krupp, "Influence of Transformation Temperature on the High-Cycle Fatigue Performance of Carbide-Bearing and Carbide-Free Bainite," *Steel Research International* 94 (2023): 2300238.

13. G. Gao, R. Liu, K. Wang, X. Gui, R. Misra, and B. Bai, "Role of Retained Austenite With Different Morphologies on Sub-Surface Fatigue Crack Initiation in Advanced Bainitic Steels," *Scripta Materialia* 184 (2020): 12–18.

14. F. Zhao, L. Morales-Rivas, Q. Yu, G. Wang, F. G. Caballero, and D. San-Martin, "Unforeseen Influence of the Prior Austenite Grain Size on

the Mechanical Properties of a Carbide-Free Bainitic Steel," *Materials Science and Engineering A* 881 (2023): 145388.

15. N. Huda, A. R. H. Midawi, J. Gianetto, R. Lazor, and A. P. Gerlich, "Influence of Martensite-Austenite (MA) on Impact Toughness of X80 Line Pipe Steels," *Materials Science and Engineering A* 662 (2016): 481–491.

16. C. Xie, Z. Liu, X. He, X. Wang, and S. Qiao, "Effect of Martensite–Austenite Constituents on Impact Toughness of Pre-Tempered MnNiMo Bainitic Steel," *Materials Characterization* 161 (2020): 110139.

17. O. Gulbay, A. Gramlich, and U. Krupp, "Effects of Silicon and Aluminum Alloying on Phase Transformation and Microstructure Evolution in Fe–0.2C–2.5Mn Steel: Insights From Continuous–Cooling–Transformation and Time–Temperature–Transformation Diagrams," *Steel Research International* 95 (2024): 2400159.

18. International Organization for Standardization, *Metallic Materials: Fatigue Testing: Fatigue Crack Growth Method*. ISO 12108, (ISO, 2002).

19. W. J. Dixon and A. M. Mood, "A Method for Obtaining and Analyzing Sensitivity Data," *Journal of the American Statistical Association* 43 (1948): 109–126.

20. H. Kitagawa and S. Takahashi, "Applicability of Fracture Mechanics to Very Small Cracks or the Cracks in the Early Stage," in *Proceedings of the 2nd International Conference on Mechanical Behaviour of Materials* (1976): 627–631. American Society for Metals (now ASM International).

21. M. H. el Haddad, T. H. Topper, and K. N. Smith, "Prediction of Non Propagating Cracks," *Engineering Fracture Mechanics* 11 (1979): 573–584.

22. P. Mohseni, J. K. Solberg, M. Karlsen, O. M. Akselsen, and E. Østby, "Investigation of Mechanism of Cleavage Fracture Initiation in Intercritically Coarse Grained Heat Affected Zone of HSLA Steel," *Materials Science and Technology* 28 (2012): 1261–1268.

23. P. Mohseni, J. K. Solberg, M. Karlsen, O. M. Akselsen, and E. Østby, "Cleavage Fracture Initiation at M–A Constituents in Intercritically Coarse-Grained Heat-Affected Zone of a HSLA Steel," *Metallurgical and Materials Transactions A* 45 (2014): 384–394.

24. Y. Li and T. N. Baker, "Effect of Morphology of Martensite–Austenite Phase on Fracture of Weld Heat Affected Zone in Vanadium and Niobium Microalloyed Steels," *Materials Science and Technology* 26 (2010): 1029–1040.

25. A. Lambert-Perlade, A. F. Gourgues, J. Besson, T. Sturel, and A. Pineau, "Mechanisms and Modeling of Cleavage Fracture in Simulated Heat-Affected Zone Microstructures of a High-Strength Low Alloy Steel," *Metallurgical and Materials Transactions A* 35 (2004): 1039–1053.

26. Z. Li, L. Tian, B. Jia, and S. Li, "A New Method to Study the Effect of M–A Constituent on Impact Toughness of IC HAZ in Q690 Steel," *Journal of Materials Research* 30 (2015): 1973–1978.

27. Z. Xiong, P. J. Jacques, A. Perlade, and T. Pardoen, "Ductile and Intergranular Brittle Fracture in a Two-Step Quenching and Partitioning Steel," *Scripta Materialia* 157 (2018): 6–9.

28. T. Tokunaga, K. Yamamoto, Y. Minamino, T. Takayama, T. Sugimoto, and K. Hagihara, "Effects of Cementite Particles on Impact Properties in High-Hardness Hypereutectoid Steels," *ISIJ International* 64 (2024): 389–400.

29. J. C. Pang, S. X. Li, Z. G. Wang, and Z. F. Zhang, "General Relation Between Tensile Strength and Fatigue Strength of Metallic Materials," *Materials Science and Engineering A* 564 (2013): 331–341.

30. J. C. Pang, S. X. Li, Z. G. Wang, and Z. F. Zhang, "Relations Between Fatigue Strength and Other Mechanical Properties of Metallic Materials," *Fatigue & Fracture of Engineering Materials & Structures* 37 (2014): 958–976.

31. R. Branco, F. Berto, F. Zhang, X. Long, and J. D. Costa, "Comparative Study of the Uniaxial Cyclic Behaviour of Carbide-Bearing and Carbide-Free Bainitic Steels," *Metals* 8 (2018): 422.

32. X. Y. Qi, L. X. Du, J. Hu, and R. Misra, "High-Cycle Fatigue Behavior of Low-C Medium-Mn High Strength Steel With Austenite-Martensite Submicron-Sized Lath-Like Structure," *Materials Science and Engineering A* 718 (2018): 477–482.

33. K. Hussain, "Short Fatigue Crack Behaviour and Analytical Models: A Review," *Engineering Fracture Mechanics* 58 (1997): 327–354.

34. U. Krupp, *Fatigue Crack Propagation in Metals and Alloys: Microstructural Aspects and Modelling Concepts* (Chichester, Weinheim: John Wiley distributor; Wiley-VCH, 2007).

35. C. Y. Huo and H. L. Gao, "Strain-Induced Martensitic Transformation in Fatigue Crack Tip Zone for a High Strength Steel," *Materials Characterization* 55 (2005): 12–18.

36. T. B. Hilditch, I. B. Timokhina, L. T. Robertson, E. V. Pereloma, and P. D. Hodgson, "Cyclic Deformation of Advanced High-Strength Steels: Mechanical Behavior and Microstructural Analysis," *Metallurgical and Materials Transactions A* 40 (2009): 342–353.

37. M. Abareshi and E. Emadoddin, "Effect of Retained Austenite Characteristics on Fatigue Behavior and Tensile Properties of Transformation Induced Plasticity Steel," *Materials & Design* 32 (2011): 5099–5105.

38. I. de Diego-Calderón, P. Rodriguez-Calvillo, A. Lara, et al., "Effect of Microstructure on Fatigue Behavior of Advanced High Strength Steels Produced by Quenching and Partitioning and the Role of Retained Austenite," *Materials Science and Engineering A* 641 (2015): 215–224.

7. Comprehensive discussion

The mechanical response of bainitic steels arises from the combined and complex effects of alloy design and thermal processing routes, which control the type, distribution, morphology, and stability of microstructural constituents. The complex nature of bainitic microstructures makes it difficult to draw straightforward links to mechanical properties, particularly in the context of fatigue. This work offers a comprehensive exploration of the microstructure and mechanical performance of bainitic microstructures in a Fe–0.2C–2.5Mn base-alloy, which was deliberately selected as a simplified alloy system to enable the clear identification of effects of Si and Al alloying. Across the studies, the effects of Si and Al on phase transformation and microstructure evolution of bainitic steels were systematically evaluated, as they are the enabling alloying elements to generate CFB [15,33,107–109]. Building upon this foundational information, the quasi-static tensile properties and HCF performance of CFB and CBB microstructures are investigated, supported by advanced characterization methods. The insights gained were further extended to assess the deformation behavior under various loading modes, highlighting the complexity between microstructural constituents, particularly retained austenite and martensite-austenite islands, in dictating fatigue crack resistance, impact toughness, and fracture mechanisms.

7.1. Controlling bainitic microstructures through processing and alloying

The investigations highlight that the bainitic microstructures can be controlled and modified through processing and alloying, which is ultimately reflected in mechanical performance. In the CBB microstructure, since there is no kinetic hindrance, the carbon rejected from α_B precipitates as cementite as a secondary phase [12,21]. By alloying Si or Al, the cementite precipitation is suppressed, allowing excessive carbon to enrich and stabilize the surrounding austenite, generating austenite containing CFB microstructures [15,33,107–109]. The γ_R forms primarily in film-like morphology between α_B plates, following the T_0 concept (**Figure 10**a). However, the MA islands and blocky austenite formation, particularly on PAGBs, are found to be a natural outcome of the existence of γ_R in CFB steels. Yet, the experimental results clearly demonstrate that the T_0 curve, correspondingly the γ_R characteristics, can be manipulated through processing and alloying.

In both bainite groups, microstructure refinement is achieved with a decrease in isothermal transformation temperature. The microstructure evolution in CBB is shown to be straightforward. The lower the transformation temperature, the finer the cementite precipitates due to limited carbon diffusivity at lower temperatures [26]. Similarly, yet with more

complexity, refinement is also achieved in CFB microstructures by decreasing the isothermal transformation temperature. Following the T_0 concept, the fraction and size of the remaining blocky austenitic regions, shown in **Figure 11**, are minimized with increased α_B fraction, and the stability of the austenite improves due to a smaller size and increased carbon distribution at lower temperatures. The influence of lower transformation temperature on the T_0 curve is displayed in **Figure 10**a. As the threshold carbon concentration of austenite increases with decreasing transformation temperature, according to the T_0 concept, more carbon is partitioned into the surrounding austenite before the transformation ceases. Therefore, the fraction and size of MA islands are minimized as more α_B forms, and the formation of film-like γ_R morphology is promoted with finer morphology. A schematic representation of this microstructural evolution is shown in **Figure 11**. When the γ_R fractions of CFB microstructures obtained at different temperatures are considered, low-temperature CFB consists of more γ_R. The synchrotron X-Ray diffraction (SYXRD) revealed that the CFB microstructure generated at 400 °C exhibited 14.3% γ_R , while it decreased to 8.7% γ_R at 450 °C. However, regarding the T_0 concept before cooling after bainitic transformation, there must be more austenite phase remaining at higher temperatures. This points out that some of the austenite transforms to martensite during subsequent cooling after bainitic transformation, indicating low thermal stability of austenite at higher transformation temperatures. Thus, the γ_R fraction decreases in the final microstructure.

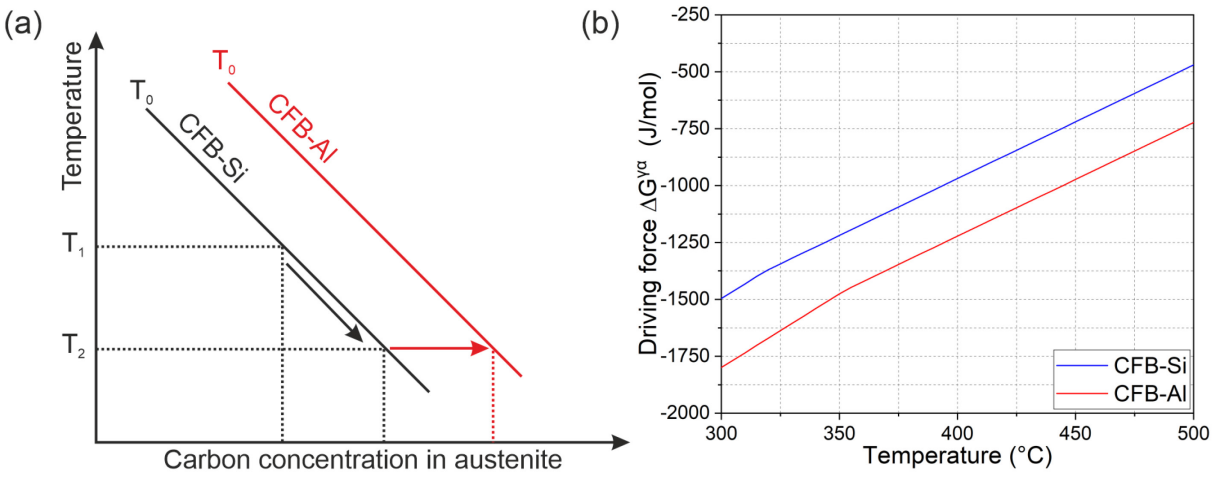

Figure 10. (a) The influence of transformation temperature and Al alloying on the T_0 curve. (b) Driving force of CFB alloys for the diffusionless transformation.

Notably, a similar effect is obtained by substituting Si completely with Al. Although Al increases the bainite transformation temperatures significantly, a finer CFB microstructure with pronounced film-like γ_R morphology is achieved. In addition to that, the size of the MA islands

and unstable blocky regions is drastically reduced (**Figure 11**). It is well known that Al increases the free energy change during bainitic transformation [29,31,110]. This is also confirmed by the thermodynamic calculations using Bhadeshia's model [111], as shown in **Figure 10**b. Therefore, with Al alloying, more α_B can be formed at the same transformation temperature, and superior carbon partitioning can be achieved compared to Si-alloyed CFB. In other words, Al alloying shifts the T_0 curve to the right, as displayed in **Figure 10**a. This results in enhanced carbon partitioning, resulting in greater austenite stabilization, leading to the reduction of MA islands and promotion of refined film-like morphology (**Figure 11**). Furthermore, since Al is a very strong ferrite stabilizer [110] and increases the driving force for diffusionless transformation of bainite (**Figure 10**b), it decreases incubation time and increases bainite transformation kinetics [29,31].

Although Al has beneficial effects on isothermally obtained CFB microstructure, some drawbacks become apparent, particularly during continuous cooling. Not only martensite and bainite formation temperatures but also critical transformation temperatures, A_{c1} and A_{c3}, increase significantly due to the strong ferrite stabilizing effect of Al, leading to higher austenitization temperatures and increased processing costs. In addition to that, despite shorter incubation times for bainitic transformation, the formation of diffusive phases is also promoted. Moreover, a transformation window emerges during the continuous cooling of Al-alloyed steel, where Widmanstätten structures form. This is attributed to the increased PAG size resulting from higher austenitization temperatures and rapid cooling rates.

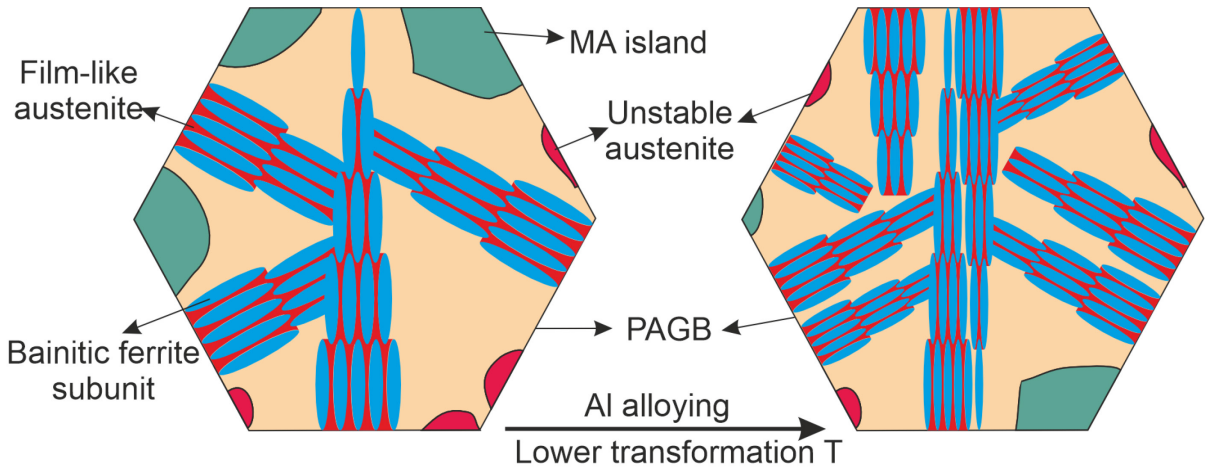

Figure 11. The representation of Al alloying and lower transformation temperature on CFB microstructure.

To facilitate a better and clearer understanding of the effects of alloying on bainite transformation characteristics and microstructure evolution, a summary of key findings is presented in **Table 3**.

Table 3. Summary of the influence of alloying elements on phase transformation and microstructure of the 0.2C-2.5Mn based steel. The first part shows the influence of alloying elements compared to the reference alloy (CBB) with no Si or Al alloying. The second part reveals the differences of Si and Al alloying on the CFB alloy.

Category		Si Alloying (CFB-Si)	Al Alloying (CFB-Al)	Remarks
B_s temperature	**Compared to the reference alloy (CBB) with no Si or Al**	No significant influence	↑↑↑	Al raises the free energy difference between α_B and austenite
M_s temperature		↓	↑↑↑	Al increases the driving force for martensitic transformation
Ac_3 temperature		↑↑	↑↑↑	Al is a stronger ferrite stabilizer than Si
PAG size (after austenitization)		Smaller than CFB-Al (~< 60 µm)	Large PAGs (~> 100 µm)	Due to the higher Ac_3 temperature in the Al alloy
Critical cooling rate to obtain martensite (Cont.)		↓	↑	Si slows kinetics; Al increases transformation rates
Bainite transformation kinetics (Iso.)		Slower (delayed start, prolonged completion)	Faster initiation; moderate completion time	Si causes stronger chemical and mechanical austenite stabilization
Promotion of diffusive phases		↑	↑↑	Al is a stronger ferrite stabilizer
Carbide formation	**Comparison between Si and Al alloying**	Suppressed	Suppressed	Low solubility of Si and Al in cementite
Carbon partitioning during bainitic transformation (Iso.)		Less carbon partitioning compared to Al-alloyed	More carbon partitioning compared to Si-alloyed	Al shifts the T_0 curve to the right
Microstructure refinement		Coarser α_B and γ_R films	Finer α_B and γ_R films	Al results in more refined bainite and γ_R
Retained austenite (γ_R)		Coarser γ_R, more unstable; MA islands form after quenching	Finer, film-like γ_R; more stable	Al promotes finer CFB with higher α_B formation and enhanced γ_R carbon enrichment
Post-quench behavior after iso. treatment		Clear martensitic transformation observed	No or negligible martensitic transformation	Indicates better γ_R stability in the Al variant

In summary, the investigations in this thesis reveal that while CBB microstructures evolve in a relatively straightforward manner, largely governed by carbon diffusion and cementite precipitation, the development of CFB microstructures is shown to be more complex. The suppression of cementite by Si or Al and the introduction of γ_R, governed by the T_0 concept,

introduce multiple microstructural variables, including MA formation, γ_R morphology, and phase stability. These features are highly sensitive to both processing parameters and alloy composition. The ability to tailor the characteristics of γ_R and MA islands through precise control of isothermal transformation temperature and alloying highlights both the potential and the intricacy of CFB design. Ultimately, this underscores that CFB microstructures, despite their enhanced mechanical potential [35], require a more nuanced understanding of thermodynamic and kinetic factors compared to their CBB counterparts.

7.2. Linking bainitic microstructures to static mechanical properties

The mechanical performance of bainitic steels is fundamentally controlled by the microstructural architecture. The quasi-static tensile properties of the isothermally produced bainitic steels are significantly improved by adding 1.5 wt.-% Si. With this simple change in the alloying concept, γ_R is introduced as a secondary phase, replacing cementite in CBB. The presence of the FCC γ_R phase in CFB enhances the dislocation motion and plasticity during uniform tensile deformation [35]. Additionally, the γ_R undergoes martensitic transformation during gradual tensile loading, contributing to improved tensile elongation. This is experimentally evidenced by the absence of γ_R in the EBSD phase map of low-temperature CFB after deformation in **Figure 12**b-c. Notably, the transformation-induced plasticity (TRIP) effect of γ_R under uniaxial tension, the UTS of the bainite is increased by more than 250 MPa, with an increase of tensile elongation of an extra 6% at higher hardness values (**Figure 12**a).

In both bainite groups, low-temperature bainitic microstructures result in improved quasi-static mechanical properties. In CBB alloys, finer carbide distribution achieved at lower transformation temperatures enhances the hardness, YS, and UTS of CBB alloys without a significant loss of ductility, due to more effective precipitation hardening. In contrast, the microstructure-property relationship in CFB is fairly more complex, influenced by multiple microstructural factors such as the features of α_B, γ_R, and MA islands. Overall results indicate that the increased YS and hardness primarily arise from the increased fraction and finer distribution of α_B, as it has higher resistance against deformation compared to γ_R. However, the contribution of martensitic constituents cannot be ruled out. Improved tensile elongation, on the other hand, is closely linked to the γ_R features obtained at lower transformation temperatures. The improved stability of γ_R at higher volume fractions promotes a prolonged TRIP effect. When this is combined with refined microstructure and reduced MA islands, enhanced elongation is achieved. It was suggested that the optimum mechanical properties are

obtained when the γ_R is in the form of films between α_B plates instead of a big blocky morphology [77].

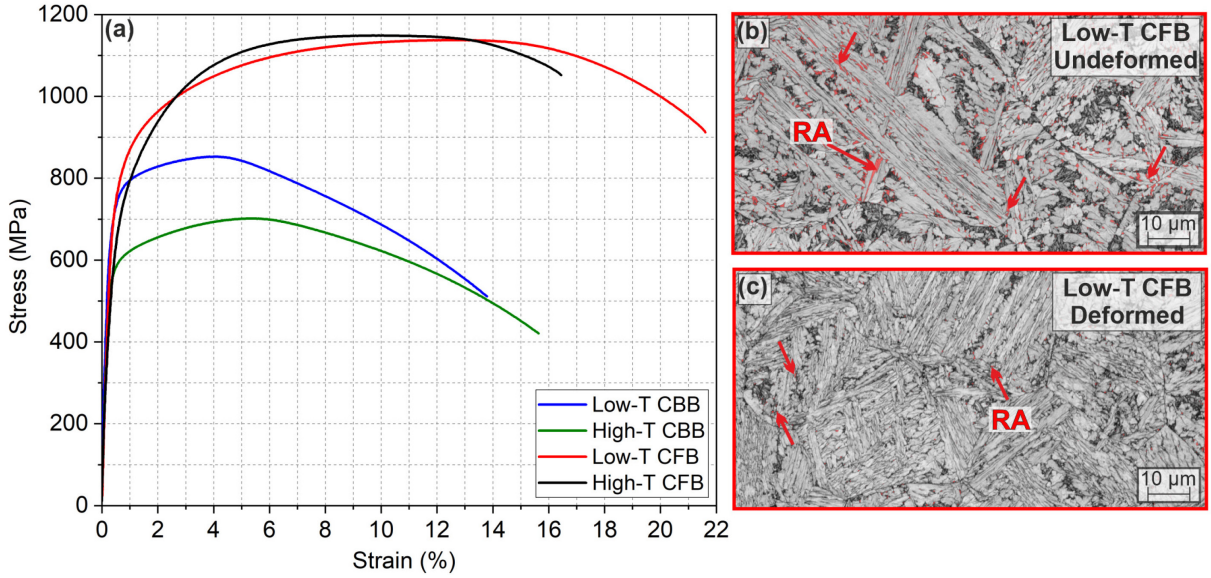

Figure 12. (a) Engineering stress-strain curves of CBB and CFB alloys, obtained at different temperatures [2]. (b, c) EBSD band contrast map superimposed with retained austenite phase of low-T CFB alloy before and after deformation, respectively.

7.3. Linking bainitic microstructures to dynamic and cyclic mechanical properties

In addition to the static mechanical properties, the fatigue limit of the bainite improves approximately 150 MPa in CFB in comparison to CBB. It is well known that there is a relationship between the hardness and UTS of materials and their fatigue limit [112,113]. As the UTS and hardness of the materials increase, the required stresses to nucleate and grow the persistent slip bands to form a crack increase similarly [88]. This simple relationship becomes even more applicable for materials similar in chemical composition and microstructure, as demonstrated during the investigations discussed. In both bainite groups, the fatigue limit is enhanced with a reduction in transformation temperature. In low-temperature CBB, finer carbide distribution and an increased proportion of high-angle boundaries act as more effective barriers against fatigue crack propagation. In addition, increased UTS in low-temperature CBB also enhances the resistance to crack initiation within the crack-free matrix. For CFB, a lower transformation temperature also leads to a higher fraction of high-angle boundaries, which further improves crack resistance. Moreover, the size and fraction of MA islands and unstable blocky austenitic regions are reduced. At the same time, the fraction and stability of γ_R increase, along with pronounced film-like morphology. This refined and more stable γ_R films between finer α_B plates provide a superior crack resistance to fatigue crack propagation compared to the more detrimental MA islands and blocky austenitic regions [44].

Interestingly, the bending fatigue experiments on the notched specimens reveal that the crack propagation resistance of the studied bainitic microstructures against an existing crack is not straightforward, as in quasi-static tensile properties and fatigue limit. The experimental crack propagation curves show that CBB has better crack propagation resistance than CFB by exhibiting a higher threshold of SIF range (ΔK_{th}) and lower crack propagation rate. The highly misoriented inter-variant boundaries (such as PAG-, packet-, and block-boundaries), which form as a result of the displacive transformation mechanism of α_B, effectively deflect the propagating crack in CBB, indicating that the fatigue crack propagation is primarily controlled by these boundaries. Correspondingly, the results evidence that cementite precipitation in the microstructure does not compromise the effectiveness of these boundaries against the fatigue crack propagation. However, in the case of CFB, the effectiveness of these boundaries, particularly of PAGBs, is outweighed by the formation of MA islands and low-stability austenitic constituents on PAGBs. The semi-quantitative analysis revealed that the crack follows an intergranular path through PAGBs when the angle between the crack and boundary is above 120°, forming a brittle necklace in the vicinity of these microstructural constituents. If the angle is lower, the crack cuts through the PAGB with minimal deflection, once again reducing the effectiveness of the PAGB. An illustration of the crack propagation in the CFB microstructure is shown in **Figure 13**.

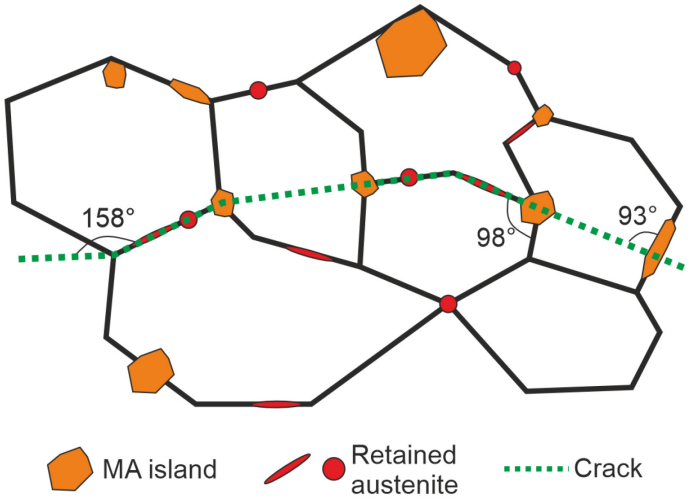

Figure 13. Schematic illustration of crack propagation in the CFB microstructure, displaying intergranular and transgranular fracture.

On the other hand, in the event of transgranular cracking in CFB, ductile fracture characteristics were observed. When considering the microstructure of CFB, the majority of the MA islands and blocky unstable austenitic constituents form on or near PAGBs, while the inner part mainly consists of multiple sheaves of α_B plates surrounded by more stable γ_R films, in different

orientations. Based on the comparative results, film-like γ_R morphology promotes plasticity in front of the crack tip and more effectively slows down the crack growth, as the fracture surface exhibits plasticity with clear fatigue striations. However, the MA islands and unstable austenitic constituents accelerate crack propagation.

The instrumented Charpy impact tests also confirm and support the findings from fatigue crack propagation tests. Although the tensile elongation of CFB was superior in all conditions compared to CBB, impact toughness values were as low as 10 J, while CBB exhibited impact toughness above 50 J. The fracture surface of CFB was dominated by brittle fracture characteristics, containing intergranular and cleavage fractures, which reinforce prior findings shown in **Figure 13**. Yet in this case, almost no plasticity was observed when a PAGB was transgranularly surpassed, leading to cleavage facets in the fracture surface. On the other hand, CBB, which contains no austenite and MA islands, exhibited substantial ductile regions also at the edges of the cleavage facets. From these results, it can be concluded that at higher deformation rates, PAGs completely debond through MA islands with minimal plasticity, outweighing the beneficial effects of α_B plates and film-like γ_R within the grains, which otherwise have been shown in literature to enhance toughness [46,47]. Therefore, it can be concluded that at high deformation rates, the presence of MA islands and austenitic constituents along PAGBs becomes even more detrimental against impact resistance, as the beneficial influence of α_B plates and film-like γ_R is eliminated.

The systematic investigations reveal that the MA islands and austenitic constituents, particularly those located on PAGBs, minimize the advantages typically associated with austenite-containing bainitic microstructures. It is evident that these constituents must be minimized, and instead, film-like γ_R must be promoted to obtain optimum dynamic and cyclic mechanical performance. Therefore, an effort must be made to control the fraction, stability, size, morphology, distribution, and position of γ_R to be able to get the maximum benefit. In the literature, metastable γ_R is widely recognized for enhancing the fatigue properties of high-strength steels through its transformation to martensite via the TRIP effect at the crack tip [52, 53, 59–61]. Due to the phase transformation and formation of compressive stresses, the energy at the crack tip can be absorbed, and the crack can be potentially decelerated. However, the investigations in this thesis reveal that the crack resistance during dynamic and cyclic loading is not straightforward in austenite-containing bainitic microstructures. Despite enhanced quasi-static mechanical properties and fatigue limit of CFB, poor crack propagation characteristics are highly likely because of the weakened nature of PAGBs, which facilitates brittle crack

advancement. This highlights the detrimental nature of the MA islands and unstable γ_R. Nevertheless, the presence of ductile regions on the fracture surface of bending specimens confirms the plasticity when the crack passes through the PAG, revealing the beneficial contributions of γ_R films between α_B plates. It is well-known that film-like γ_R is mechanically more stable than blocky γ_R and MA islands [8]. As a result, during plastic deformation, particularly in the event of martensitic transformation ahead of the crack, parallelly aligned γ_R films between α_B plates within the PAGs are more effective at dissipating energy compared to substantially metastable MA islands and austenitic constituents on PAGBs.

8. Conclusions

In order to find design strategies to optimize the mechanical performance of bainitic steels, the influence of Si and Al is systematically investigated in different cooling conditions to understand the effect of each alloying element in carbide-free bainitic (CFB) microstructure as opposed to carbide-bearing bainite (CBB). In addition to that, the mechanical performance of CBB and CFB microstructures is evaluated comparatively under various loading conditions to understand the role of individual microstructural constituents, particularly the complex structure of CFB, in governing deformation mechanisms for the intended applications. The following conclusions can be drawn:

Influence of Si and Al alloying on CFB

- Al promotes ferritic microstructures more strongly than Si in the investigated steel. Notably, increased prior austenite grain size, due to higher necessary austenitization temperatures, leads to the formation of Widmanstätten structures during continuous cooling at higher cooling rates.
- Si slows bainite transformation kinetics via austenite stabilization against phase transformation as a result of carbon partitioning and solid solution strengthening. Although Al has the same effects, it accelerates bainite transformation during isothermal holding by increasing the thermodynamic driving force, effectively overcoming the retardation.
- Under isothermal conditions, Al promotes the formation of finer CFB microstructure with film-like retained austenite through increased bainitic ferrite (α_B) formation and enhanced carbon enrichment. This leads to enhanced austenite stability and a significant reduction in MA island formation, compared to Si alloyed CFB.

Static mechanical properties

- The static mechanical properties of bainitic steels are strongly governed by their microstructural architecture. An alloying modification of 1.5 wt.-% Si addition significantly enhances the quasi-static tensile properties of bainite by promoting the formation of retained austenite (γ_R), replacing cementite as a secondary phase.
- CFB outperforms CBB in quasi-static tensile properties mainly due to the gradual transformation of γ_R to martensite through transformation-induced plasticity (TRIP) effect, which improves ductility and strength during uniformly distributed deformation at lower strain rates. This is evidenced by the disappearance of γ_R after deformation, confirming its transformation to martensite.

- The TRIP effect in CFB increases the UTS by more than 250 MPa and enhances elongation by approximately 6%, even at higher hardness levels compared to carbide-bearing bainite (CBB).
- In both CBB and CFB, lower transformation temperatures improve quasi-static mechanical performance. In CBB, this is mainly due to finer carbide distribution and enhanced precipitation hardening, leading to increased hardness, YS, and UTS without a notable reduction in ductility.
- In CFB, the mechanical response is influenced by a complex interplay of microstructural constituents, including α_B, γ_R, and martensite–austenite (MA) islands. Higher YS and hardness stem from increased α_B content, while improved elongation is closely associated with higher fractions and enhanced stability of γ_R at low transformation temperatures.
- The highest combination of strength and tensile ductility in CFB is achieved when γ_R is present as thin films between α_B plates, rather than in blocky morphologies, minimizing MA island formation and maximizing TRIP effectiveness.

Dynamic and cyclic mechanical properties

- The fatigue limit of the CFB microstructure improves by approximately 150 MPa compared to CBB, correlating well with its increased UTS and hardness. This reflects the well-established relationship between hardness and fatigue limit in comparable materials.
- The optimization of microstructure, especially γ_R, in CFB is critical to achieve optimum mechanical performance under varying loading conditions. The formation of MA islands and unstable austenitic constituents at PAGBs has an adverse role on fracture behavior when deformation progression is localized, as in Charpy impact and fatigue crack propagation tests.
- CBB shows significantly higher impact toughness, with notable ductile regions in the fracture surface, whereas CFB exhibits brittle behavior. The existence of brittle MA islands and sudden transformation of γ_R at higher strain rates, combined with a localized deformation mechanism, promotes a brittle network along the PAGBs, causing intergranular fracture or rapid debonding of PAGs through MA islands, causing cleavage fracture.
- Despite the higher fatigue limit, CFB shows a higher fatigue crack propagation rate and lower threshold of SIF range ΔK_{th} than CBB. While PAGBs in CBB successfully deflect the fatigue cracks, MA islands, and unstable austenitic constituents in CFB weaken these

boundaries, resulting in intergranular fractures through the brittle network or cracks that cut PAGBs without deflection. However, ductile fracture behavior is observed when the crack goes through a PAG instead of cleavage fracture, highlighting the influence of a lower deformation rate compared to Charpy impact tests.

In summary, the comparison of the investigated bainitic steel concepts reveals that the most desirable microstructure for bainite is not straightforward. While the majority of the studies refer to the benefits of austenite-containing bainitic steels based on static mechanical properties, the drawbacks concerning Charpy impact toughness and fatigue crack propagation characteristics need to be considered in dependence on the intended application. Yet the findings in this thesis strongly suggest that, through appropriate microstructural design via alloying and processing adjustments, the CFB microstructure can be designed to enhance the dynamic and cyclic mechanical properties by minimizing the formation, size, and fraction of MA islands and unstable austenitic constituents, especially those formed on PAGBs. In this way, the effective role of PAGBs in deflecting local cracks can be restored, and crack propagation behavior can be improved further when combined with the advantageous film-like γ_R morphology within the PAGs.

9. References

[1] O. Gulbay, A. Gramlich, U. Krupp, Effects of silicon and aluminum alloying on phase transformation and microstructure evolution in Fe–0.2C–2.5Mn steel: Insights from continuous–cooling–transformation and time–temperature–transformation diagrams, *Steel Research International*. 95 (**2024**), 2400159. DOI: 10.1002/srin.202400159.

[2] O. Gulbay, M. Ackermann, A. Gramlich, A.R. Durmaz, I. Steinbach, U. Krupp, Influence of transformation temperature on the high-cycle fatigue performance of carbide-bearing and carbide-free bainite, *Steel Research International*. 94 (**2023**), 2300238. DOI: 10.1002/srin.202300238.

[3] O. Gulbay, A. Gramlich, U. Krupp, Impact toughness and fatigue crack propagation in carbide-free bainite: The adverse role of retained austenite and martensite-austenite islands, *Fatigue & Fracture of Engineering Materials and Structures*. 48 (**2025**), 4217–4227. DOI: 10.1111/ffe.70025.

[4] D.K. Nerella, M.A. Ali, H. Salama, O. Gulbay, M. Ackermann, O. Shchyglo, U. Krupp et al., Automated workflow for phase-field simulations: Unveiling the impact of heat-treatment parameters on bainitic microstructure in steel, *Advanced Engineering Materials*. 27 (**2025**), 2400905. DOI: 10.1002/adem.202400905.

[5] A. Gramlich, W. Hagedorn, K. Greiff, U. Krupp, Air cooling martensites—The future of carbon neutral steel forgings?, *Advanced Engineering Materials*. 25 (**2023**), 2201931. DOI: 10.1002/adem.202201931.

[6] C. Hofer, F. Winkelhofer, H. Clemens, S. Primig, Morphology change of retained austenite during austempering of carbide-free bainitic steel, *Materials Science and Engineering: A*. 664 (**2016**), 236–246. DOI: 10.1016/j.msea.2016.04.005.

[7] K. Wang, Z. Tan, G. Gao, B. Gao, X. Gui, R. Misra, B. Bai, Microstructure-property relationship in bainitic steel: The effect of austempering, *Materials Science and Engineering: A*. 675 (**2016**), 120–127. DOI: 10.1016/j.msea.2016.08.026.

[8] B.C. De Cooman, Structure–properties relationship in TRIP steels containing carbide-free bainite, *Current Opinion in Solid State and Materials Science*. 8 (**2004**), 285–303. DOI: 10.1016/j.cossms.2004.10.002.

[9] J.-B. Seol, D. Raabe, P.-P. Choi, Y.-R. Im, C.-G. Park, Atomic scale effects of alloying, partitioning, solute drag and austempering on the mechanical properties of high-carbon bainitic–austenitic TRIP steels, *Acta Materialia*. 60 (**2012**), 6183–6199. DOI: 10.1016/j.actamat.2012.07.064.

[10] L.C.D. Fielding, The bainite controversy, *Materials Science and Technology*. 29 (**2013**), 383–399. DOI: 10.1179/1743284712Y.0000000157.

[11] E.S. Davenport, E.C. Bain, Transformation of austenite at constant subcritical temperatures, *Metallurgical Transactions*. 1 (**1970**), 3503–3530. DOI: 10.1007/BF03037892.

[12] H.K.D.H. Bhadeshia, Bainite in steels: Transformations, microstructure and properties, 2nd ed., IOM Communications, London, **2001**.

[13] R.F. Mehl, Hardenability of alloy steels, American Society for Metals, Cleveland, **1939**.

[14] H.K.D.H. Bhadeshia, The bainite transformation: unresolved issues, *Materials Science and Engineering: A*. 273-275 (**1999**), 58–66. DOI: 10.1016/S0921-5093(99)00289-0.

[15] H.K.D.H. Bhadeshia, D.V. Edmonds, Bainite in silicon steels: new composition–property approach Part 1, *Metal Science*. 17 (**1983**), 411–419. DOI: 10.1179/030634583790420600.

[16] H. Beladi, V. Tari, I.B. Timokhina, P. Cizek, G.S. Rohrer, A.D. Rollett, P.D. Hodgson, On the crystallographic characteristics of nanobainitic steel, *Acta Materialia*. 127 (**2017**), 426–437. DOI: 10.1016/j.actamat.2017.01.058.

[17] H.M. Flower, T.C. Lindley, Electron backscattering diffraction study of acicular ferrite, bainite, and martensite steel microstructures, *Materials Science and Technology*. 16 (**2000**), 26–40. DOI: 10.1179/026708300773002636.

[18] Hiromoto Kitahara, Rintaro Ueji, Nobuhiro Tsuji, Yoritoshi Minamino, Crystallographic features of lath martensite in low-carbon steel, *Acta Materialia*. 54 (**2006**), 1279–1288. DOI: 10.1016/j.actamat.2005.11.001.

[19] A. Kumar, A. Singh, Mechanical properties of nanostructured bainitic steels, *Materialia*. 15 (**2021**), 101034. DOI: 10.1016/j.mtla.2021.101034.

[20] H.K.D.H. Bhadeshia, D.V. Edmonds, Bainite in silicon steels: new composition–property approach Part 2, *Metal Science*. 17 (**1983**), 420–425. DOI: 10.1179/030634583790420646.

[21] X.Y. Long, F.C. Zhang, J. Kang, Z.N. Yang, D.D. Wu, K.M. Wu, G.H. Zhang, Study on carbide-bearing and carbide-free bainitic steels and their wear resistance, *Materials Science and Technology*. 33 (**2017**), 615–622. DOI: 10.1080/02670836.2016.1242205.

[22] A. Kumar, A. Singh, The role of microstructure on damage tolerance in nano-bainitic steels, *Procedia Structural Integrity*. 28 (**2020**), 93–100. DOI: 10.1016/j.prostr.2020.10.012.

[23] B.L. Bramfitt, J.G. Speer, A perspective on the morphology of bainite, *Metallurgical Transactions A*. 21 (**1990**), 817–829. DOI: 10.1007/BF02656565.

[24] S. Zajac, V. Schwinn, K.H. Tacke, Characterisation and quantification of complex bainitic microstructures in high and ultra-high strength linepipe steels, *Materials Science Forum*. 500-501 (**2005**), 387–394. DOI: 10.4028/www.scientific.net/MSF.500-501.387.

[25] F.L.H. Gerdemann, Bainite in medium carbon steels, Doctorate dissertation, RWTH Aachen University, Steel Institute, Aachen, **2010**.

[26] F.G. Caballero, M.K. Miller, C. Garcia-Mateo, Influence of transformation temperature on carbide precipitation sequence during lower bainite formation, *Materials Chemistry and Physics*. 146 (**2014**), 50–57. DOI: 10.1016/j.matchemphys.2014.02.041.

[27] M. Takahashi, H.K.D.H Bhadeshia, Model for transition from upper to lower bainite, *Materials Science and Technology*. 6 (**1990**), 592–603.

[28] F.G. Caballero, M.J. Santofimia, C. Capdevila, C. GarcíA-Mateo, C. García de Andrés, Design of advanced bainitic steels by optimisation of TTT diagrams and T0 curves, *ISIJ International*. 46 (**2006**), 1479–1488. DOI: 10.2355/isijinternational.46.1479.

[29] C. Garcia-Mateo, F.G. Caballero, H.K.D.H. Bhadeshia, Acceleration of low-temperature bainite, *ISIJ International*. 43 (**2003**), 1821–1825. DOI: 10.2355/isijinternational.43.1821.

[30] M. Gomez, C.I. Garcia, D.M. Haezebrouck, A.J. Deardo, Design of composition in (Al/Si)-alloyed TRIP steels, *ISIJ International*. 49 (**2009**), 302–311. DOI: 10.2355/isijinternational.49.302.

[31] J. Tian, G. Xu, M. Zhou, H. Hu, Z. Xue, Effects of Al addition on bainite transformation and properties of high-strength carbide-free bainitic steels, *Journal of Iron and Steel Research International*. 26 (**2019**), 846–855. DOI: 10.1007/s42243-019-00253-7.

[32] M. Morawiec, A. Grajcar, W. Zalecki, C. Garcia-Mateo, M. Opiela, Dilatometric study of phase transformations in 5 Mn steel subjected to different heat treatments, *Materials (Basel, Switzerland)*. 13 (**2020**). DOI: 10.3390/ma13040958.

[33] E. Kozeschnik, H.K.D.H. Bhadeshia, Influence of silicon on cementite precipitation in steels, *Materials Science and Technology*. 24 (**2008**), 343–347. DOI: 10.1179/174328408X275973.

[34] B.P.J. Sandvik, The bainite reaction in Fe-Si-C Alloys: The primary stage, *Metallurgical and Materials Transactions A*. 13 (**1982**), 777–787. DOI: 10.1007/BF02642391.

[35] X. Long, F. Zhang, Z. Yang, B. Lv, Study on microstructures and properties of carbide-free and carbide-bearing bainitic steels, *Materials Science and Engineering: A*. 715 (**2018**), 10–16. DOI: 10.1016/j.msea.2017.12.108.

[36] R. Branco, F. Berto, F. Zhang, X. Long, J. D. Costa, Comparative study of the uniaxial cyclic behaviour of carbide-bearing and carbide-free bainitic steels.

[37] F.G. Caballero, S. Allain, J. Cornide, J.D.P. Velásquez, C. Garcia-Mateo, M.K. Miller, Design of cold rolled and continuous annealed carbide-free bainitic steels for automotive application, *Materials & Design*. 49 (**2013**), 667–680. DOI: 10.1016/j.matdes.2013.02.046.

[38] R. Branco, F. Berto, F. Zhang, X. Long, J.D. Costa, Comparative study of the uniaxial cyclic behaviour of carbide-bearing and carbide-free bainitic steels, *Metals*. 8 (**2018**), 422. DOI: 10.3390/met8060422.

[39] F.G. Caballero, H. Roelofs, S. Hasler, C. Capdevila, J. Chao, J. Cornide, C. Garcia-Mateo, Influence of bainite morphology on impact toughness of continuously cooled cementite free bainitic steels, *Materials Science and Technology*. 28 (**2012**), 95–102. DOI: 10.1179/1743284710Y.0000000047.

[40] H.K.D.H. Bhadeshia, D.V. Edmonds, The mechanism of bainite formation in steels, *Acta Metallurgica*. 28 (**1980**), 1265–1273. DOI: 10.1016/0001-6160(80)90082-6.

[41] P. Retzl, S. Zamberger, E. Kozeschnik, Computational analysis of austenite film thickness and C-redistribution in carbide-free bainite, *Materials Research Express*. 8 (**2021**), 76502. DOI: 10.1088/2053-1591/ac0d6f.

[42] L.C. Chang, H.K.D.H. Bhadeshia, Austenite films in bainitic microstructures, *Materials Science and Technology*. 11 (**1995**), 874–882. DOI: 10.1179/mst.1995.11.9.874.

[43] F.G. Caballero, J. Chao, J. Cornide, C. García-Mateo, M.J. Santofimia, C. Capdevila, Toughness deterioration in advanced high strength bainitic steels, *Materials Science and Engineering: A*. 525 (**2009**), 87–95. DOI: 10.1016/j.msea.2009.06.034.

[44] G. Gao, R. Liu, K. Wang, X. Gui, R. Misra, B. Bai, Role of retained austenite with different morphologies on sub-surface fatigue crack initiation in advanced bainitic steels, *Scripta Materialia*. 184 (**2020**), 12–18. DOI: 10.1016/j.scriptamat.2020.03.036.

[45] F. Zhao, L. Morales-Rivas, Q. Yu, G. Wang, F.G. Caballero, D. San-Martin, Unforeseen influence of the prior austenite grain size on the mechanical properties of a carbide-free bainitic steel, *Materials Science and Engineering: A*. 881 (**2023**), 145388. DOI: 10.1016/j.msea.2023.145388.

[46] F.G. Caballero, H.K.D.H. Bhadeshia, Very strong bainite, *Current Opinion in Solid State and Materials Science*. 8 (**2004**), 251–257. DOI: 10.1016/j.cossms.2004.09.005.

[47] F. G. Caballero, H. K. D. H. Bhadeshia, K. J. A. Mawella, D. G. Jones, P. Brown, Very strong low temperature bainite, *Materials Science and Technology*. 18 (**2002**), 279–284. DOI: 10.1179/026708301225000725.

[48] C. Garcia-Mateo, F. G. Caballero, H. K. D. H. Bhadeshia, Development of Hard Bainite, *ISIJ International*. 43 (**2003**), 1238–1243. DOI: 10.2355/isijinternational.43.1238.

[49] T. Sourmail, C. Garcia-Mateo, F.G. Caballero, L. Morales-Rivas, R. Rementeria, M. Kuntz, Tensile ductility of nanostructured bainitic steels: Influence of retained austenite stability, *Metals*. 7 (**2017**). DOI: 10.3390/met7010031.

[50] S.M.C. van Bohemen, Bainite and martensite start temperature calculated with exponential carbon dependence, *Materials Science and Technology*. 28 (**2012**), 487–495. DOI: 10.1179/1743284711Y.0000000097.

[51] J. Wang, P.J. van der Wolk, S. van der Zwaag, On the influence of alloying elements on the bainite reaction in low alloy steels during continuous cooling, *Journal of Materials Science*. 35 (**2000**), 4393–4404. DOI: 10.1023/A:1004865209116.

[52] E. Swallow, H.K.D.H. Bhadeshia, High resolution observations of displacements caused by bainitic transformation, *Materials Science and Technology*. 12 (**1996**), 121–125. DOI: 10.1179/mst.1996.12.2.121.

[53] M. Song, B. Song, Z. Yang, S. Zhang, C. Hu, Effects of Mn and Al on the intragranular acicular ferrite formation in rare earth treated C–Mn Steel, *High Temperature Materials and Processes*. 36 (**2017**), 683–691. DOI: 10.1515/htmp-2016-0003.

[54] A.R.M. Gramlich, Properties and heat treatments of air-hardening ductile forging steels, Doctorate dissertation, RWTH Aachen University, Steel Institute, 2022.

[55] Z. Changle, F. Hanguang, M. Shengqiang, Y. Dawei, L. Jian, X. Zhenguo, L. Yongping, Effect of Mn content on microstructure and properties of wear-resistant bainitic steel, *Materials Research Express*. 6 (**2019**), 86581. DOI: 10.1088/2053-1591/ab1c8d.

[56] A. Grajcar, W. Zalecki, W. Burian, A. Kozłowska, Phase equilibrium and austenite decomposition in advanced high-strength medium-Mn bainitic steels, *Metals*. 6 (**2016**), 248. DOI: 10.3390/met6100248.

[57] S.K. Liu, L. Yang, D.G. Zhu, J. Zhang, The influence of the alloying elements upon the transformation kinetics and morphologies of ferrite plates in alloy steels, *Metallurgical and Materials Transactions A*. 25 (**1994**), 1991–2000. DOI: 10.1007/BF02649047.

[58] C. Hofer, S. Primig, H. Clemens, F. Winkelhofer, R. Schnitzer, Influence of heat treatment on microstructure stability and mechanical properties of a carbide-free bainitic steel, *Advanced Engineering Materials*. 19 (**2017**), 1600658. DOI: 10.1002/adem.201600658.

[59] C. Garcia-Mateo, F.G. Caballero, The role of retained austenite on tensile properties of steels with bainitic microstructures, *Materials Transactions*. 46 (**2005**), 1839–1846. DOI: 10.2320/matertrans.46.1839.

[60] G. Gaiser, P. Presoly, C. Bernhard, K. Baumgartner, S. Grosseiber, Influence of silicon and tramp elements on the high-temperature oxidation of steel in direct casting and rolling processes, *ISIJ International*. 64 (**2024**), 1439–1449. DOI: 10.2355/isijinternational.ISIJINT-2024-072.

[61] G. Gaiser, R. Krobath, P. Presoly, C. Bernhard, The influence of intergranular oxidation on surface crack formation in continuous casting of steel, *Journal of Materials Research and Technology*. 26 (**2023**), 9276–9288. DOI: 10.1016/j.jmrt.2023.09.214.

[62] A. Gramlich, C. van der Linde, M. Ackermann, W. Bleck, Effect of molybdenum, aluminium and boron on the phase transformation in 4 wt.–% manganese steels, *Results in Materials*. 8 (**2020**), 100147. DOI: 10.1016/j.rinma.2020.100147.

[63] T. Allam, W. Bleck, C. Klinkenberg, B. Kintscher, U. Krupp, J. Rudnizki, The continuous casting behavior of medium manganese steels, *Journal of Materials Research and Technology*. 15 (**2021**), 292–305. DOI: 10.1016/j.jmrt.2021.08.019.

[64] M.A. Ackermann, Bainitic TRIP steels for controlled cooled wire rod, Doctorate dissertation, RWTH Aachen University, Steel Institute, 2020.

[65] H. Goldenstein, H.I. Aaronson, Overall reaction kinetics and morphology of austenite decomposition between the upper nose and the Ms of a hypoeutectoid Fe-C-Cr alloy, *Metallurgical Transactions A*. 21 (**1990**), 1465–1478. DOI: 10.1007/BF02672562.

[66] C.A. Keul, Einstellung, Charakterisierung und Eigenschaften von bainitischen Mikrostrukturen in Schmiedestählen mit mittlerem Kohlenstoffgehalt, Dissertation, RWTH Aachen University, Steel Institute, Aachen, 2012.

[67] W.T. Reynolds, F.Z. Li, C.K. Shui, H.I. Aaronson, The incomplete transformation phenomenon in Fe-C-Mo alloys, *Metallurgical Transactions A*. 21 (**1990**), 1433–1463. DOI: 10.1007/BF02672561.

[68] P. Haslberger, C. Turk, K. Babinsky, D. Caliskanoglu, H. Clemens, S. Primig, Boron grain boundary Segregation in a heat treatable steel, *BHM Berg- und Hüttenmännische Monatshefte*. 160 (**2015**), 204–208. DOI: 10.1007/s00501-015-0358-1.

[69] B. Białobrzeska, Effect of boron accompanied by chromium, vanadium and titanium on kinetics of austenite grain growth, *Ironmaking & Steelmaking*. 48 (**2021**), 649–676. DOI: 10.1080/03019233.2021.1889894.

[70] K. Zhu, C. Oberbillig, C. Musik, D. Loison, T. Iung, Effect of B and B+Nb on the bainitic transformation in low carbon steels, *Materials Science and Engineering: A*. 528 (**2011**), 4222–4231. DOI: 10.1016/j.msea.2011.02.022.

[71] W. Hagedorn, A. Gramlich, K. Greiff, U. Krupp, Alloy and process design of forging steels for better environmental performance, *Sustainable Materials and Technologies*. 34 (**2022**), e00509. DOI: 10.1016/j.susmat.2022.e00509.

[72] C. Hofer, H. Leitner, F. Winkelhofer, H. Clemens, S. Primig, Structural characterization of "carbide-free" bainite in a Fe–0.2C–1.5Si–2.5Mn steel, *Materials Characterization*. 102 (**2015**), 85–91. DOI: 10.1016/j.matchar.2015.02.020.

[73] F.G. Caballero, C. GarcíA-Mateo, J. Chao, M.J. Santofimia, C. Capdevila, C.G. de Andrés, Effects of Morphology and Stability of Retained Austenite on the Ductility of TRIP-aided Bainitic Steels, *ISIJ International*. 48 (**2008**), 1256–1262. DOI: 10.2355/isijinternational.48.1256.

[74] H. Guo, X. Feng, A. Zhao, Q. Li, M. Chai, Effects of ausforming temperature on bainite transformation kinetics, microstructures and mechanical properties in ultra-fine bainitic steel, *Journal of Materials Research and Technology*. 9 (**2020**), 1593–1605. DOI: 10.1016/j.jmrt.2019.11.085.

[75] S. Sharma, S. Sangal, K. Mondal, Development of new high-strength carbide-free bainitic steels, *Metallurgical and Materials Transactions A*. 42 (**2011**), 3921–3933. DOI: 10.1007/s11661-011-0797-6.

[76] J. Meng, Y. Feng, Q. Zhou, L. Zhao, F. Zhang, L. Qian, Effects of austempering temperature on strength, ductility and toughness of low-C high-Al/Si carbide-free bainitic steel, *Journal of Materials Engineering and Performance*. 24 (**2015**), 3068–3076. DOI: 10.1007/s11665-015-1567-1.

[77] B.P.J. Sandvik, H.P. Nevalainen, Structure-property relationships in commercial low-alloy bainitic-austenitic steel with high strength, ductility, and toughness, *Metals Technology*. 8 (**1981**), 213–220. DOI: 10.1179/030716981803275992.

[78] C. Wang, M. Wang, J. Shi, W. Hui, H. Dong, Effect of microstructural refinement on the toughness of low carbon martensitic steel, *Scripta Materialia*. 58 (**2008**), 492–495. DOI: 10.1016/j.scriptamat.2007.10.053.

[79] V.I. Zurnadzhy, V.G. Efremenko, I. Petryshynets, K. Shimizu, M.N. Brykov, Kushchenko IV, V.V. Kudin, Mechanical properties of carbide-free lower bainite in complex-alloyed constructional steel: Effect of bainitizing treatment parameters, *Metallic Materials/Kovové Materiály*. 48 (**2020**).

[80] P. Mohseni, J.K. Solberg, M. Karlsen, O.M. Akselsen, E. Østby, Investigation of mechanism of cleavage fracture initiation in intercritically coarse grained heat affected zone of HSLA steel, *Materials Science and Technology*. 28 (**2012**), 1261–1268. DOI: 10.1179/1743284712Y.0000000056.

[81] P. Mohseni, J.K. Solberg, M. Karlsen, O.M. Akselsen, E. Østby, Cleavage fracture initiation at M–A constituents in intercritically coarse-grained heat-fffected zone of a HSLA steel, *Metallurgical and Materials Transactions A*. 45 (**2014**), 384–394. DOI: 10.1007/s11661-013-2110-3.

[82] N. Huda, A.R.H. Midawi, J. Gianetto, R. Lazor, A.P. Gerlich, Influence of martensite-austenite (MA) on impact toughness of X80 line pipe steels, *Materials Science and Engineering: A*. 662 (**2016**), 481–491. DOI: 10.1016/j.msea.2016.03.095.

[83] X.L. Wang, Z.Q. Wang, Z.J. Xie, X.P. Ma, S. Subramanian, C. Shang, X.C. Li et al., Combined effect of M/A constituent and grain boundary on the impact toughness of CGHAZ and ICCGHAZ of E550 grade offshore engineering steel, *Mathematical biosciences and engineering MBE*. 16 (**2019**), 7494–7509. DOI: 10.3934/mbe.2019376.

[84] Y. Dai, S. Wang, Q. He, C. Liu, X. Wang, X. Li, L. Li et al., Effect of microstructure on slip-induced crack initiation and early propagation of martensitic steel during high cycle fatigue, *International Journal of Fatigue*. 167 (**2023**), 107275. DOI: 10.1016/j.ijfatigue.2022.107275.

[85] M.N. Batista, S. Hereñú, I. Alvarez-Armas, The Role of microstructure in fatigue crack initiation and propagation in 9-12Cr ferritic-martensitic steels, *Procedia Engineering*. 74 (**2014**), 228–231. DOI: 10.1016/j.proeng.2014.06.253.

[86] K. Koschella, U. Krupp, Investigations of fatigue damage in tempered martensitic steel in the HCF regime, *International Journal of Fatigue*. 124 (**2019**), 113–122. DOI: 10.1016/j.ijfatigue.2019.02.050.

[87] L. Morsdorf, O. Jeannin, D. Barbier, M. Mitsuhara, D. Raabe, C.C. Tasan, Multiple mechanisms of lath martensite plasticity, *Acta Materialia*. 121 (**2016**), 202–214. DOI: 10.1016/j.actamat.2016.09.006.

[88] J.C. Stinville, M.A. Charpagne, A. Cervellon, S. Hemery, F. Wang, P.G. Callahan, V. Valle et al., On the origins of fatigue strength in crystalline metallic materials, *Science (New York, N.Y.)*. 377 (**2022**), 1065–1071. DOI: 10.1126/science.abn0392.

[89] P. Lukáš, L. Kunz ‡, Role of persistent slip bands in fatigue, *Philosophical Magazine*. 84 (**2004**), 317–330. DOI: 10.1080/14786430310001610339.

[90] B. Mi, Y. Fu, S. Liu, Y. Wang, Z. Yang, C. Zhang, Initiation of internal fatigue crack in a carbide-free bainitic steel during high cycle fatigue, *Journal of Materials Research and Technology*. 30 (**2024**), 1786–1794. DOI: 10.1016/j.jmrt.2024.03.196.

[91] G. Gao, R. Liu, Y. Fan, G. Qian, X. Gui, R. Misra, B. Bai, Mechanism of subsurface microstructural fatigue crack initiation during high and very-high cycle fatigue of advanced bainitic steels, *Journal of Materials Science & Technology*. 108 (**2022**), 142–157. DOI: 10.1016/j.jmst.2021.08.060.

[92] U. Krupp, K. Koschella, A. Giertler, The significance of grain size, segregations and inclusions for the very high cycle fatigue (VHCF) behavior of tempered martensitic steels, *Procedia Structural Integrity*. 23 (**2019**), 517–522. DOI: 10.1016/j.prostr.2020.01.138.

[93] U. Krupp, M. Solovev, F. Honecker, B. Adams, J.-C. Florian, The potential of self-tempered martensite and bainite in improving the fatigue strength of thermomechanically processed steels, *MATEC Web of Conferences*. 165 (**2018**), 20006. DOI: 10.1051/matecconf/201816520006.

[94] M.-S. Baek, K.-S. Kim, T.-W. Park, J. Ham, K.-A. Lee, Quantitative phase analysis of martensite-bainite steel using EBSD and its microstructure, tensile and high-cycle fatigue behaviors, *Materials Science and Engineering: A*. 785 (**2020**), 139375. DOI: 10.1016/j.msea.2020.139375.

[95] P. Zhao, G. Gao, R. Misra, B. Bai, Effect of microstructure on the very high cycle fatigue behavior of a bainite/martensite multiphase steel, *Materials Science and Engineering: A*. 630 (**2015**), 1–7. DOI: 10.1016/j.msea.2015.02.015.

[96] J.-Z. Chen, B. Zhang, L.-R. Zeng, Z.-M. Song, Y.-Y. She, G.-P. Zhang, Optimal bainite contents for maximizing fatigue cracking resistance of bainite/martensite dual-phase EA4T steels, *Steel Research International*. 89 (**2018**), 1700562. DOI: 10.1002/srin.201700562.

[97] R. Rementeria, L. Morales-Rivas, M. Kuntz, C. Garcia-Mateo, E. Kerscher, T. Sourmail, F.G. Caballero, On the role of microstructure in governing the fatigue behaviour of nanostructured bainitic steels, *Materials Science and Engineering: A*. 630 (**2015**), 71–77. DOI: 10.1016/j.msea.2015.02.016.

[98] X. Li, T. Ye, Y. Du, M. Zhan, X. Wang, Y. Dai, Y. Liu et al., Effect of microstructure on small fatigue crack initiation and early propagation behavior in super martensite stainless steel, *International Journal of Fatigue*. 190 (**2025**), 108604. DOI: 10.1016/j.ijfatigue.2024.108604.

[99] I. Mueller, R. Rementeria, F.G. Caballero, M. Kuntz, T. Sourmail, E. Kerscher, A constitutive relationship between fatigue limit and microstructure in nanostructured bainitic steels, *Materials*. 9 (**2016**). DOI: 10.3390/ma9100831.

[100] C.Y. Huo, H.L. Gao, Strain-induced martensitic transformation in fatigue crack tip zone for a high strength steel, *Materials Characterization*. 55 (**2005**), 12–18. DOI: 10.1016/j.matchar.2005.02.004.

[101] B. Dönges, A. Giertler, U. Krupp, C.-P. Fritzen, H.-J. Christ, Significance of crystallographic misorientation at phase boundaries for fatigue crack initiation in a duplex stainless steel during high and very high cycle fatigue loading, *Materials Science and Engineering: A*. 589 (**2014**), 146–152. DOI: 10.1016/j.msea.2013.09.098.

[102] J. Yang, T.S. Wang, B. Zhang, F.C. Zhang, High-cycle bending fatigue behaviour of nanostructured bainitic steel, *Scripta Materialia*. 66 (**2012**), 363–366. DOI: 10.1016/j.scriptamat.2011.11.033.

[103] L.I. Wenyan, Q.U. Jingsin, S. Hesheng, Fatigue crack growth behaviour of a Si–Mn steel with carbide-free lathy bainite, *Journal of Materials Science*. 32 (**1997**), 427–430. DOI: 10.1023/A:1018565702991.

[104] A. Kumar, A. Singh, Microstructural effects on the sub-critical fatigue crack growth in nano-bainite, *Materials Science and Engineering: A*. 743 (**2019**), 464–471. DOI: 10.1016/j.msea.2018.11.114.

[105] F. Niessen, T. Nyyssönen, A.A. Gazder, R. Hielscher, Parent grain reconstruction from partially or fully transformed microstructures in MTEX, *Journal of applied crystallography*. 55 (**2022**), 180–194. DOI: 10.1107/S1600576721011560.

[106] W.J. Dixon, A.M. Mood, A method for obtaining and analyzing sensitivity data, *Journal of the American Statistical Association*. 43 (**1948**), 109–126. DOI: 10.1080/01621459.1948.10483254.

[107] L.C. Chang, Bainite transformation temperatures in high-silicon steels, *Metallurgical and Materials Transactions A*. 30 (**1999**), 909–916. DOI: 10.1007/s11661-999-0144-3.

[108] X. Long, F. Zhang, Z. Yang, M. Zhang, Study on bainitic transformation by dilatometer and in situ LSCM, *Materials (Basel, Switzerland)*. 12 (**2019**). DOI: 10.3390/ma12091534.

[109] X.Y. Long, J. Kang, B. Lv, F.C. Zhang, Carbide-free bainite in medium carbon steel, *Materials & Design*. 64 (**2014**), 237–245. DOI: 10.1016/j.matdes.2014.07.055.

[110] A. Mertens, P.J. Jacques, J. Sietsma, F. Delannay, Relative influences of aluminium and silicon on the kinetics of bainite formation from intercritical Austenite, *Steel Research International*. 79 (**2008**), 954–959. DOI: 10.1002/srin.200806226.

[111] M. Peet, H.K.D.H. Bhadeshia, Program MAP_STEEL_MUCG83.

[112] J.C. Pang, S.X. Li, Z.G. Wang, Z.F. Zhang, General relation between tensile strength and fatigue strength of metallic materials, *Materials Science and Engineering: A*. 564 (**2013**), 331–341. DOI: 10.1016/j.msea.2012.11.103.

[113] J.C. Pang, S.X. Li, Z.G. Wang, Z.F. Zhang, Relations between fatigue strength and other mechanical properties of metallic materials, *Fatigue & Fracture of Engineering Materials & Structures*. 37 (**2014**), 958–976. DOI: 10.1111/ffe.12158.

RESEARCH ARTICLE

ADVANCED ENGINEERING MATERIALS
www.aem-journal.com

Automated Workflow for Phase-Field Simulations: Unveiling the Impact of Heat-Treatment Parameters on Bainitic Microstructure in Steel

Dhanunjaya K. Nerella, Muhammad Adil Ali, Hesham Salama, Oguz Gulbay, Marc Ackermann, Oleg Shchyglo, Ulrich Krupp, and Ingo Steinbach*

Bainitic steels are extensively utilized across various sectors, such as the automotive and railway industries, owing to their impressive mechanical properties, including strength, hardness, and fatigue resistance. However, the pursuit of achieving the desired optimal mechanical properties presents considerable challenges due to the intricate bainitic microstructures consisting of multiple phases. To tackle these challenges, an automated workflow is used for extracting 2D and 3D microstructural features. The proposed method allows for a detailed examination of the correlations between microstructure characteristics and the processing parameters, specifically the holding temperature during transformation. In these findings, it is revealed that as the holding temperature decreases, there is a notable reduction in microstructural element size and carbon partitioning. Some of the observations are microstructural features such as area, perimeter, and thickness of the bainitic ferrite grains under two different holding temperatures. Phase-field simulations results show that the microstructures at lower holding temperatures have finer grains. The distributions of grain areas and perimeters are uniform, with smaller grains dominating at low and high isothermal holding temperatures. While the grain thickness measurements from simulations and experiments at high temperature are qualitatively aligned, data from low temperatures show discrepancies.

1. Introduction

Bainitic steels have many engineering applications due to their good mechanical properties. Because of their enhanced fatigue and wear resistance properties, they are widely used in the railway industry and in automotive applications such as gears and bearings.[1] Bainitic microstructures, which are responsible for obtaining good mechanical properties, are dependent on chemical composition and processing parameters, e.g., heat treatment. Thus, there is a strong relationship between the process–structure–property for bainitic steels. In the context of bainitic microstructures, it still remains controversial whether it is formed in a diffusion-controlled or deformation-controlled manner.[2] Bainitic microstructures are complex in nature consisting of a wide range of morphologies like laths of bainitic ferrite (BF), martensite–austenite (MA) islands observed in low-carbon alloys with Si, Mn, and Cr, retained austenite (RA) films and carbide precipitates observed in Fe—C alloys with Mn and Cr.[3] Identification and segmentation of MA islands using deep-learning methods were implemented in ref. [4], where the morphological features of the MA islands are studied. Widths of BF and RA were studied in refs. [3,5], BF plate misorientation analysis was carried out in ref. [6]. Length of the BF laths was studied in ref. [7].

Since most of the experimental studies are carried out in 2D, the microstructure analysis is typically limited to 2D. Morphological analysis of BF is limited in existing studies where the morphological feature extraction of BF is limited to not more than two. Complete feature extraction of BF is complex because of its morphology and 3D morphological feature extraction of BF is extremely difficult to perform experimentally. In contrast, phase-field (PF) simulations can deliver realistic microstructures comparable to experimental results.[8] Subsequently the 3D microstructural features from PF simulations can be used to study the process–structure–property relationships. Analysis of microstructures from the PF method using n-point statistics was described in refs. [9,10].

Computational materials science in general and theoretical PF simulations in particular are witnessing a remarkable surge in

D. K. Nerella, M. A. Ali, H. Salama, O. Shchyglo, I. Steinbach
Interdisciplinary Centre for Advanced Materials Simulation
Ruhr-Universität Bochum
Universität Str. 150, 44801 Bochum, Germany
E-mail: dhanunjaya.nerella@rub.de

O. Gulbay, M. Ackermann, U. Krupp
Steel Institute
RWTH Aachen University
52072 Aachen, Germany

The ORCID identification number(s) for the author(s) of this article can be found under https://doi.org/10.1002/adem.202400905.

DOI: 10.1002/adem.202400905

ADVANCED SCIENCE NEWS
www.advancedsciencenews.com

ADVANCED ENGINEERING MATERIALS
www.aem-journal.com

predictive capabilities owing to continual advancements in theoretical frameworks, computing technologies, and software development. As researchers aim to construct comprehensive databases of materials properties, they encounter the formidable task of executing numerous computations, potentially reaching into the thousands. The complexities involved in generating input files and troubleshooting errors encountered during these computational efforts pose increasingly challenging obstacles. Moreover, the absence of well-documented procedures complicates the process of mastering diverse analysis techniques, leading to inefficiencies in tool utilization. Often, certain calculations entail labor-intensive steps vulnerable to human errors. To overcome these challenges, implementing automated workflows emerges as a crucial strategy with numerous advantages. By simplifying the execution of calculations, these workflows free researchers from the tedious details of computational tasks, enabling them to focus on the core scientific aspects of their work. Furthermore, by introducing standardized protocols for simulations, these workflows promote reproducibility and facilitate thorough testing of hypotheses. Additionally, they empower researchers to undertake extensive explorations of high-dimensional materials parameter spaces, a task that would otherwise be excessively time-consuming.[11,12]

Successful implementations of automated workflows are both diverse and promising. For instance, Nikolaev et al.[13] have made significant strides in realizing automated rapid serial experimentation, marking a substantial leap toward autonomous closed-loop learning systems. Similarly, Dimitrov et al.[14] have developed an autonomous system for molecular synthesis and characterization. Additionally, Matthew et al.[12] have elucidated a comprehensive framework for conducting atomistic simulations of materials, underscoring the versatility of automated workflows across different domains. There are readily available commercial[15] and open-source workflow managers[16] for theoretical simulations and data analysis which greatly simplify computational science efforts in industry and academia.

In the present study, we introduce an automated workflow tailored to establish a nuanced relationship between heat-treatment parameters and microstructural features, leveraging PF simulation results. Through the seamless integration of computational methodologies, our approach promises to unravel intricate correlations between heat-treatment parameters and microstructural features (**Figure 1**).

2. Theoretical Background and Methodology

2.1. Workflow Implementation

The workflow in this study integrates a variety of computational tools and libraries, all coordinated through the Python programming language.[17] The approach begins with the generation of microstructures, simulated by the OpenPhase software tool[18–20] which is a software library implementing the PF method. It offers a robust platform for simulating microstructural evolution under predefined conditions. It requires an input file that defines various parameters such as alloy composition, mechanical properties, heat-treatment conditions, and numerical discretization parameters. Upon successful completion of the simulation, OpenPhase outputs the data in a *.vtk* file format which is then converted to *.csv* to streamline post-processing analysis. Subsequently, Python libraries such as PIL[21] and OpenCV,[22] widely recognized for their ability in image analysis, are employed for 2D microstructure analysis. The typical microstructural features which can be extracted from the simulations are listed in **Table 1**. A single BF variant with a unique index (from simulation) is considered as a "grain" for morphological feature analysis. Furthermore, 3D information, including the volume of grains, is subsequently calculated.

2.2. Bainitic Microstructure

To simulate the bainite microstructure, 3D simulations were carried out for a binary Fe—C steel with 0.2 wt% carbon. The simulations were performed in a simulation box with regular grid consisting of $128 \times 128 \times 128$ grid cells with the grid spacing

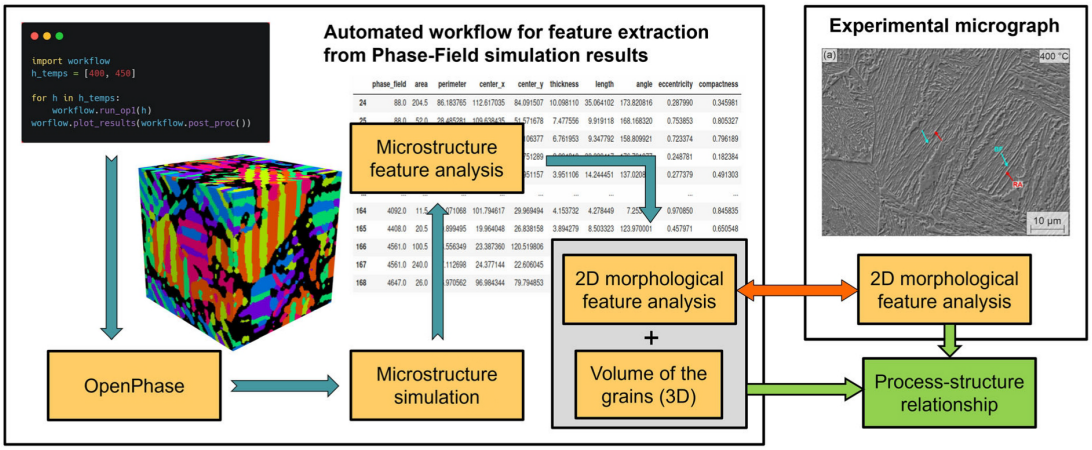

Figure 1. Automated workflow implementation to investigate the process–structure relationship for bainitic microstructure using phase-field simulation results.

ADVANCED SCIENCE NEWS
www.advancedsciencenews.com

ADVANCED ENGINEERING MATERIALS
www.aem-journal.com

Table 1. List of extracted 2D morphological features.

Parameter	Description
Area	The area of the bainitic ferrite grain.
Perimeter	The perimeter of the bainitic ferrite grain.
Length	The length of the bainitic ferrite grain.
Thickness	The thickness of the bainitic ferrite grain.
Direction	Angle of the fitted ellipse around the grain.
Aspect ratio	Ratio of thickness of the bainitic ferrite grain to the length of the bainitic ferrite grain. It is one of the shape factors.
Compactness	Compactness ranges between 0 and 1. Perfect circle have a compactness of 1 and 0 indicates the lack of compactness. It is one of the shape factors.
Equivalent radius	Radius of the circle with an equal aggregate sectional area.

of 0.05 μm and periodic boundary conditions. The simulations begin at a high temperature of 627 °C, where austenite is a stable phase. Upon cooling, BF nucleates and grows from the austenite subject to driving forces depending on mechanical, chemical, and thermal conditions. The PF simulations are performed using the approach presented in ref. [20]. Within this approach, the temperature evolution in the simulations follows Newton's law of cooling, which gives realistic thermal behavior depending on the temperature difference between the sample and the cooling bath

$$\dot{T}(t) = -\beta(T(t) - T_s) + \frac{Q\dot{\phi}}{\rho C_p} \tag{1}$$

where $T(t)$ is the temperature within the sample which is considered uniform across the sample, T_s represents the temperature of the cooling bath, Q is the latent heat of transformation, ρ is the mass density, and $\dot{\phi}$ is the average rate of phase change throughout the volume of the sample. The heat extraction coefficient β, which quantifies the heat removal from the sample, is given by

$$\beta = \frac{A\alpha}{V\rho c_p} \tag{2}$$

and accounts for the type of cooling medium used, e.g., air, oil, or water. In the current study, the value for the heat extraction coefficient $\beta = 0.25\ s^{-1}$ (approximate cooling rate at the beginning of the bainite formation is (100 K s^{-1}) used for two different isothermal holding temperatures $T_{iso} = 400$ and 450 °C.

It is known that the rapid quenching rates and lower holding temperatures can lead to the formation of lower bainite, which results in a structure closely resembling tempered martensite. In contrast to the martensite formation where no carbon partitioning is observed during the transformation and which only occurs during the subsequent tempering, during the bainite formation, the carbon partitioning and diffusion occur alongside the deformation induced transformation. Conversely, low quenching rates and higher holding temperatures can lead to the formation of upper bainite, where deformation and carbon redistribution occur concurrently.

In the current study, we limit our consideration to the formation of lower bainite. To do so, 24 different Kurdjumov–Sachs variants of BF are nucleated and grown from a single austenite grain. In this study, we do not consider cementite precipitation due to the lack of simulation resolution required by the size of the fine cementite precipitates size. The resulting microstructures considering two different values of isothermal holding temperatures (T_{iso}) are displayed in **Figure 2**a,b. Variations in the isothermal holding temperatures alter the transformation kinetics, thereby affecting the morphology of the bainitic microstructure which will be analyzed in the following sections. Figure 2c,d illustrates the carbon distribution within the sample after a simulation duration of 75 s, with isothermal holding temperatures of $T_{iso} = 400$ °C and $T_{iso} = 450$ °C, respectively. Significantly lower-carbon partitioning is observed for the isothermal holding temperature of 400 °C compared to 450 °C. And in-depth carbon composition analysis is beyond the scope of this article and will be published elsewhere.

2.3. 2D Microstructural Investigation from PF Simulation Results

To analyze the 2D morphological features of the 3D microstructures obtained from the PF simulations, a slicing operation is performed, as illustrated in **Figure 3**. The slices are taken along the (0,0,1) direction.

Traditionally, morphological features such as the area and perimeter of grains have been extracted from experimental microstructures. However, these features alone may not suffice to fully characterize the morphology, especially in the case of non-equiaxed grains where shape factors, like the aspect ratio, play a crucial role. For instance, microstructures with similar grain areas but different grain shapes can exhibit significantly different morphologies. To address this issue, additional morphological features, including shape factors, are extracted to analyze complex morphological characteristics.

Technically, 2D morphological features are obtained for each grain by masking out all other grains. The OpenCV library[22] is utilized to extract some of these morphological features. A comprehensive list of the extracted 2D morphological features is provided in Table 1.

An example of extracted morphological features can be seen in **Figure 4**. The mentioned set of features is extracted as they are commonly analyzed for experimental microstructures.[4]

2.4. 3D Microstructural Features

Most experimental studies on microstructures have traditionally been conducted in 2D, with morphological features extracted from 2D micrographs, as discussed in Section 2.3. However, the extrapolation of 2D morphological features to 3D often results in significant information loss, failing to accurately represent the true 3D characteristics of the material.[8] Key properties such as the volume of the grain and its aspect ratio are inherently 3D and cannot be fully captured through 2D analysis alone. Estimating the aspect ratio from 2D observations is particularly prone to error, given the absence of information on the third dimension.

ADVANCED SCIENCE NEWS
www.advancedsciencenews.com
ADVANCED ENGINEERING MATERIALS
www.aem-journal.com

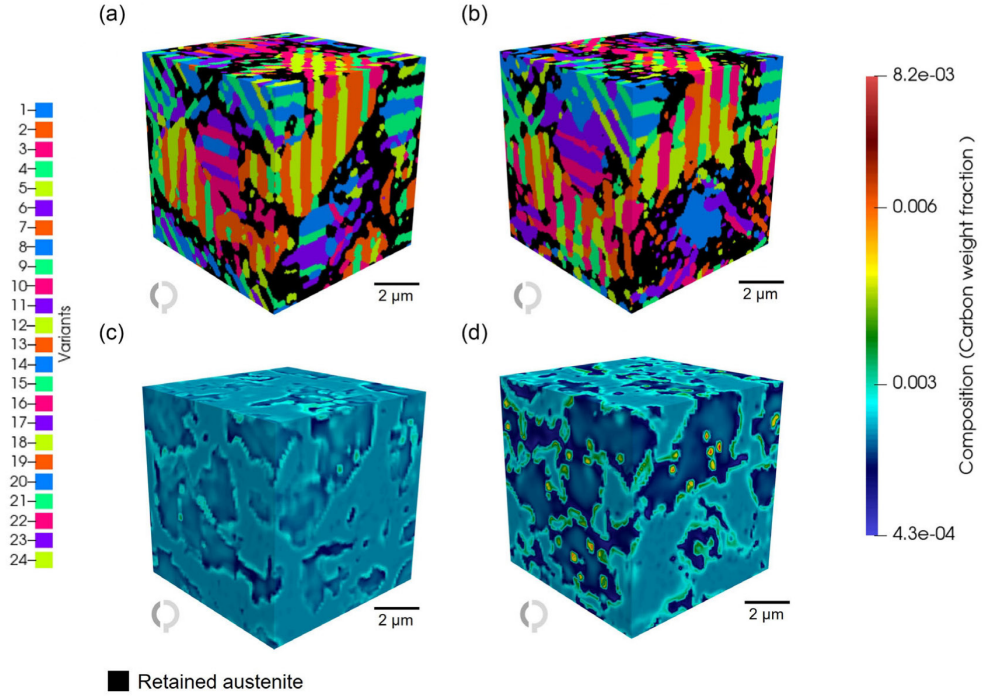

Figure 2. Bainitic microstructures simulated for two different isothermal holding temperatures: a) $T_{iso} = 400\,°C$ and b) $T_{iso} = 450\,°C$; c,d) corresponding carbon concentrations.

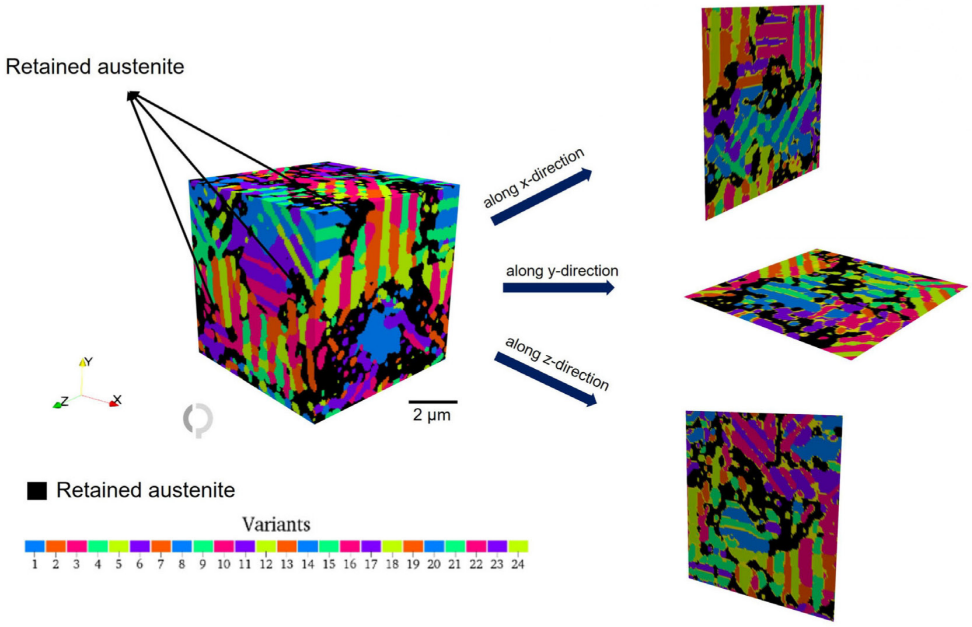

Figure 3. Automated 2D slicing as a solution to generate large datasets for effective application of ML methods.

ADVANCED SCIENCE NEWS
www.advancedsciencenews.com

ADVANCED ENGINEERING MATERIALS
www.aem-journal.com

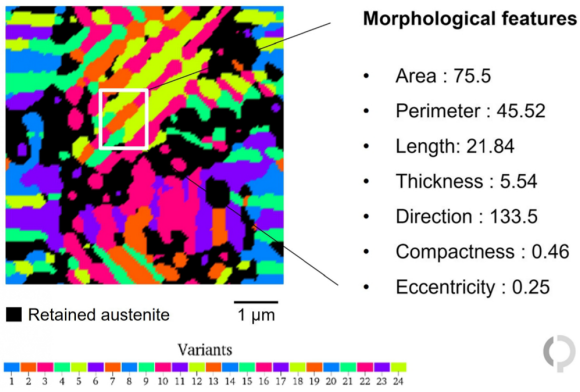

Figure 4. Extracted 2D morphological features for a grain in the white box.

The adoption of 3D morphological analysis enables a more precise differentiation between various bainite morphologies, such as lath-like bainite, which is prevalent within bainitic structures. Moreover, utilizing 3D data allows accurate identification of neighboring grains, a critical aspect to understand microstructural interactions.[23]

3. Results and Discussion

Two different carbide-free bainitic microstructures were achieved via isothermal holding for 45 min at 400 and 450 °C for Si-alloyed bainitic steel with a chemical composition shown in **Table 2**.[3] More details regarding alloy production and processes can be found in ref. [3]. Scanning electron microscope (SEM) images of two different isothermal heat treatments (quenching to a) 400 °C and b) 450 °C with 45 min of isothermal holding) are shown in **Figure 5**. SEM investigations were carried out using a field-emission gun Zeiss Sigma SEM (Carl Zeiss Microscopy GmbH, Germany). The images were acquired using a secondary electron detector with a 30 μm aperture, an accelerating voltage of 15 kV, and a working distance of 9 mm. Both the SEM microstructures exhibited platelike BF and RA films between the BF plates. An example of the areas that consisted of these morphologies is highlighted with orange-dashed lines in the microstructures. From the SEM images, it can be observed that the number of similar regions was increased in low-temperature bainite. In addition to this, it becomes clear that with decreasing the isothermal transformation temperature, a finer microstructure was obtained. Compared to the isothermal holding temperature at 450 °C, the average thickness of BF plates and RA films decreased at 400 °C. In the prior study of Gulbay et al.[3] a statistical analysis was conducted to reveal the differences in the average thickness of BF plates and RA films of these two microstructure states. In this study, the number of analyzed BF plates and RA films was extended to achieve more accurate results. For the measurements, only the platelike BF and filmlike RA morphologies were used as highlighted in the orange regions in Figure 5. Other morphologies were not included in the measurements for comparability reasons. ImageJ software was used for the thickness measurements and more than 400 measurements were accomplished using multiple SEM images for each phase of each alloy state. With decreasing isothermal holding temperature, the average thickness of BF plates decreased from 0.26 to 0.15 μm, while the width of RA films decreased from 0.25 to 0.15 μm. The summary of the statistical analysis for the thickness measurements can be found in **Table 3**.

Table 2. Chemical compositions of the material used for the experimental study. Optical emission spectroscopy (OES) was used for determining chemical composition and combustion analysis was used to estimate carbon.

Elements	C	Si	Mn	P	S	Cr	Mo	Al	Cu
wt%	0.19	1.48	2.38	0.003	0.003	0.04	0.01	0.003	0.02

Table 3. Measured average thickness of BF plates and RA films.

Heat-treatment state	Bainitic ferrite [μm]	Retained austenite [μm]
400 °C	0.15 ± 0.05	0.15 ± 0.05
450 °C	0.26 ± 0.08	0.25 ± 0.09

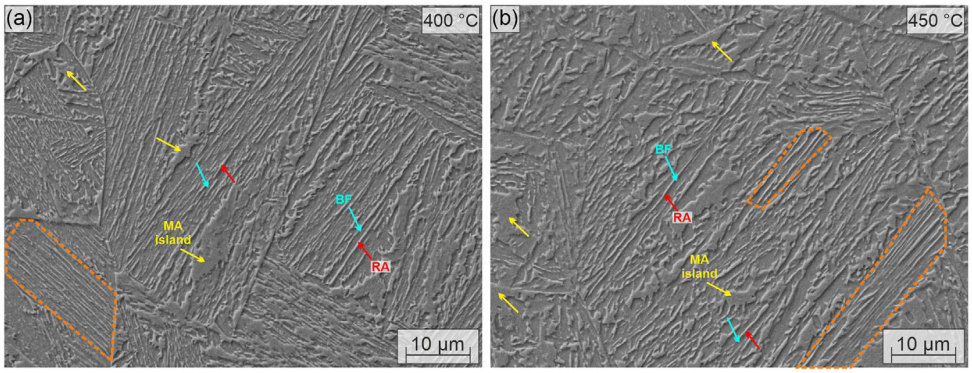

Figure 5. SEM images of microstructures isothermal obtained at a) 400 °C and b) 450 °C.

ADVANCED SCIENCE NEWS
www.advancedsciencenews.com

ADVANCED ENGINEERING MATERIALS
www.aem-journal.com

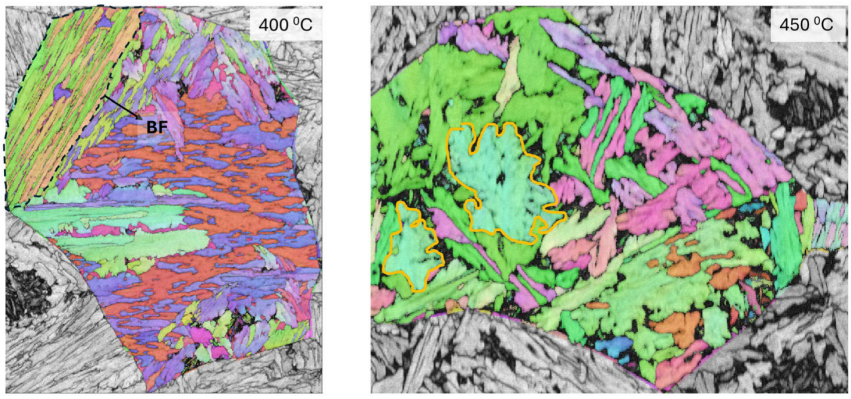

Figure 6. Inverse pole figure maps of single prior austenite grain (PAG) from holding temperatures 400 and 450 °C, respectively.

3.1. 2D Microstructural Investigations from Experimental Observations

The inverse pole figure (IPF) maps are obtained for a single prior austenite grain (PAG) for both isothermal states which are shown in **Figure 6**. The EBSD measurements were accomplished using a NordlysNano (Oxford Instruments, Great Britain) detector. For the EBSD measurements, aperture size of 75 µm, an accelerating voltage of 20 kV, a working distance of 17 mm, and a step size of 50 nm are used. EBSD post-processing is done using AZtecCrystal Software from Oxford Instruments. A single PAG is selected for comparison with simulation results. IPF map of the sample with an isothermal holding temperature of 400 °C shows thin lath-like morphologies of BF, highlighted in the black-dashed region. In contrast, the sample from the isothermal holding temperature of 450 °C shows coarser morphology of BF highlighted in the orange color. Most of the microstructure from 450 °C exhibit coarser morphology unlike in 400 °C and morphological measurements support this observation. Results reveal the similarities between experiments and simulation as they exhibit morphologies and are discussed in the following sections.

In carbide-free bainitic steels, it is well-known that excessive carbon is enriched in surrounding austenite when a BF plate is formed during the bainitic transformation.[24,25] Therefore,

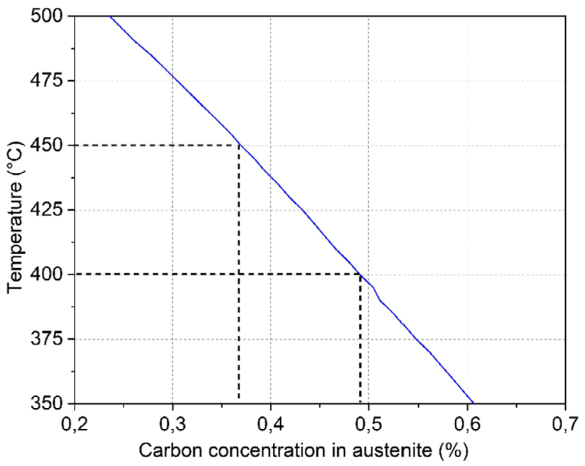

Figure 7. The T_0 curve of the studied alloy between 350 and 500 °C. 400 J mol^{-1} was included in the calculations as the strain energy of bainitic ferrite.

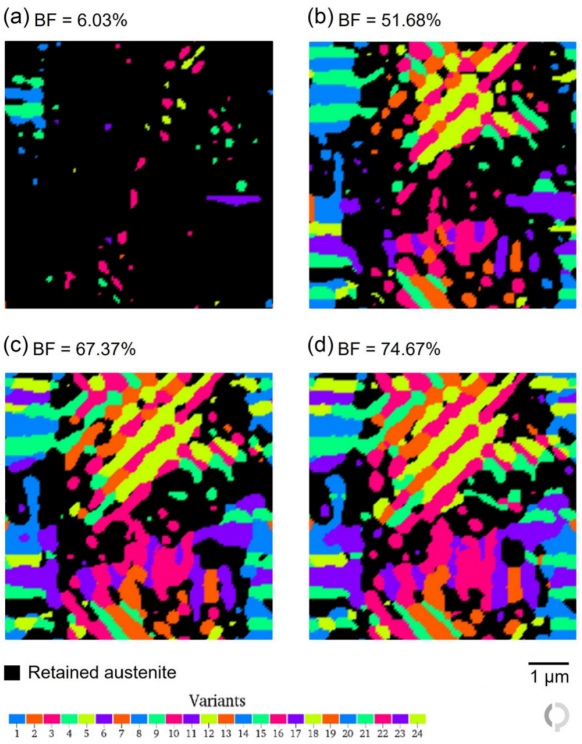

Figure 8. Evolution of bainitic ferrite (BF) microstructures for isothermal holding temperature T_{iso} = 400 °C: a) BF: 6.03%, b) BF: 51.68%, c) BF: 67.37%, and d) BF: 74.67%.

ADVANCED SCIENCE NEWS
www.advancedsciencenews.com

ADVANCED ENGINEERING MATERIALS
www.aem-journal.com

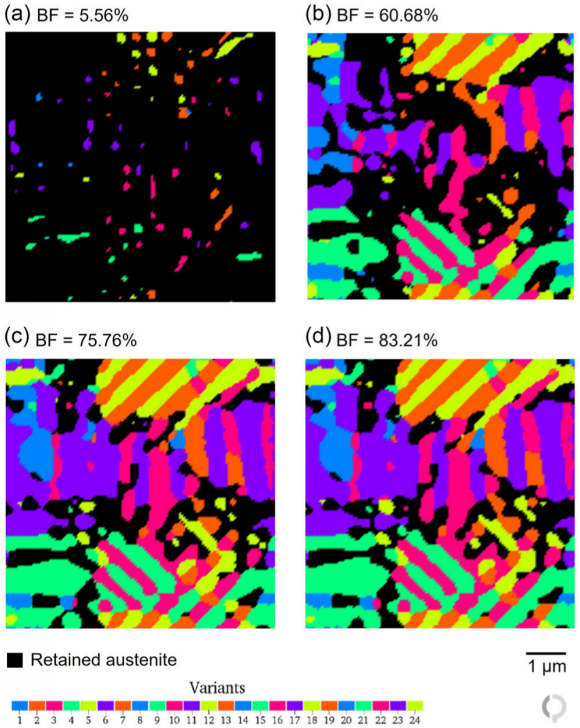

Figure 9. Evolution of bainitic ferrite (BF) microstructures for isothermal holding temperature $T_{iso} = 450\,°C$: a) BF: 5.56%, b) BF: 60.68%, c) BF: 75.76%, and d) BF: 83.21%.

carbon-enriched zones form adjacent to BF plates due to carbon partitioning and the carbon concentration in these zones decreases with an increasing distance from BF plates.[26] According to the incomplete-reaction phenomena (T0 concept), the spontaneous transformation of austenite to BF ceases when the carbon concentration in austenite reaches a threshold value. This means that a new BF plate can only form again when the carbon concentration is below a threshold value in austenite.[27] As displayed in **Figure 7**, the T_0 curve (temperature versus carbon concentration in austenite) is determined between 350 and 500 °C for this chemical composition via the thermodynamical calculations using Bhadeshia's model.[28] As highlighted in Figure 6, the carbon threshold that austenite can store increases with decreasing temperature. In other words, at 400 °C, the next BF plate starts forming at a higher carbon concentration (smaller distance) at the austenite interface compared to 450 °C, which results in finer RA films and finer microstructure. In addition to that, the mechanical strength of RA plays an important role in the thickness of the BF plates.[29] The yield strength of RA increases with decreasing transformation temperature. This enhances the resistance against growth of BF plate, which is inherited as finer BF plates in the microstructure.

Additionally, both microstructures exhibited MA islands mostly located at the PAG boundaries (PAGB), as highlighted in Figure 5. It is well accepted that there are two main types of RA in carbide-free bainitic microstructures. The first one is the nanoscale filmlike morphology, which forms between BF plates and exhibits enhanced thermal stability. The second one is relatively larger in scale and has a blocky morphology, which mostly forms at PAGB and is thermally unstable compared to the filmlike type.[30] Due to the low thermal stability of blocky RA, they are prone to transform to martensite during subsequent cooling after isothermal holding, hence the formation of MA islands.[3]

3.2. Evolution of Microstructure During Transformation in PF Simulations

Microstructure evolution of BF at two isothermal holding temperatures is presented in **Figure 8** and **9**. Unlike in experiments, we can easily track the microstructure evolution throughout the entire transformation. For the bainitic transformation with

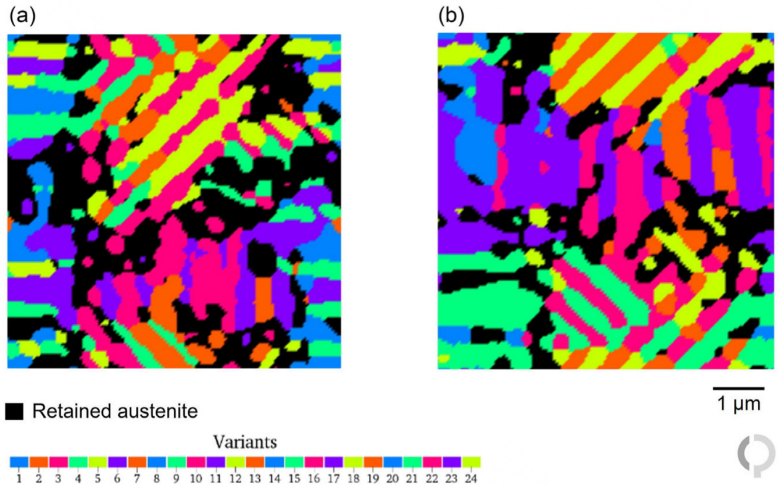

Figure 10. The 2D slice of interest for two isothermal holding temperatures: a) $T_{iso} = 400\,°C$ and b) $T_{iso} = 450\,°C$.

ADVANCED SCIENCE NEWS
www.advancedsciencenews.com

ADVANCED ENGINEERING MATERIALS
www.aem-journal.com

Table 4. Average values of 2D morphological features for two isothermal holding temperatures.

Parameter	$T_{iso} = 400\,°C$	$T_{iso} = 450\,°C$
Area [px]	62.11	89.84
Perimeter [px]	37.01	43.26
Length [px]	15.28	19.95
Thickness [px]	6.82	7.64
Aspect ratio	0.52	0.53
Compactness	0.58	0.58

$T_{iso} = 400\,°C$, austenite begins to break down into bainite, revealing small grains and small traces of lath-like structures of BF during the initial stages. As the bainitic transformation progresses, it becomes evident that different morphologies like lath structures and irregular polygonal structures are observed throughout the later stages.

Conversely, during the bainitic transformation with $T_{iso} = 450\,°C$, the breakdown of austenite initially favors the formation of smaller structures and irregular structures over lath-like structures. As the bainitic transformation continues, the development of irregular polygonal structures and lath-like structures is more pronounced compared to small grain-like structures. Further analysis of the microstructure morphology is presented in Section 3.3.

3.3. 2D Microstructural Investigation from PF Simulation Results

3.3.1. Morphological Feature Analysis

In the current study, BF microstructures resulting from two isothermal holding temperatures are examined as discussed in previous sections. To investigate the 2D morphology of these microstructures, a slice of interest (SOI) has been extracted from each of the two bainitic samples in the (0,0,1) direction, as illustrated in **Figure 10**. We have detailed information on the phase and the variants of BF for every pixel within the SOI from the PF simulation results using OpenPhase.[18] This information provides an additional advantage for more precise analysis of the microstructures. The morphological features of the microstructure, outlined in Table 1, are quantified for each grain. The total counts of grains in the slices are 123 and 143, respectively. The proportions of RA in the SOIs are 25.33% and 16.76%, respectively. Grains smaller than ten pixels have been excluded from consideration to minimize the effect of the numerical discretization limit of PF simulations. Average values of certain morphological features across all grains are summarized in **Table 4**. These measurements are provided in pixels, with a conversion factor of 1 µm equaling 20 pixels (px).

According to the data presented in Table 4, it is evident that the average grain size, measured in terms of area, is smaller for grains resulting from lower holding temperature compared to higher holding temperature. These findings align with previous

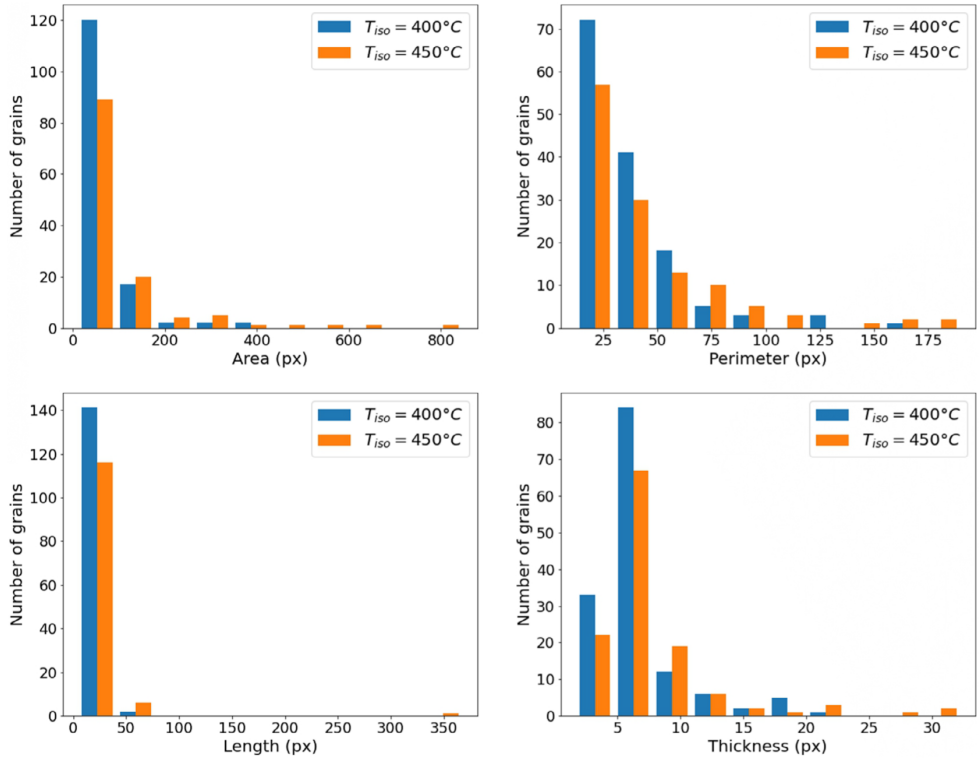

Figure 11. Distribution of different morphological parameters of all grains.

ADVANCED SCIENCE NEWS
www.advancedsciencenews.com

ADVANCED ENGINEERING MATERIALS
www.aem-journal.com

experimental studies in ref. [3]. Also, coarser BF is observed at high holding temperature from simulations and experiments which can be seen in Figure 6 and 10.

This observation is particularly significant as it provides insights into the influence of isothermal holding temperatures on microstructural characteristics. However, examining the average grain size alone may not fully capture the distribution of grain sizes within the microstructure. For a more comprehensive understanding, the distribution of grain sizes across the sample can be visualized, as depicted in **Figure 11**. This distribution allows for a more detailed analysis of the variations in grain sizes and their implications on the overall microstructure.

In the present work, we attribute the microstructures to lath bainite. The designations of these morphologies are taken from refs. [31,32].

The analysis of grain area distribution shows a sharp decrease in grain size at both holding temperatures. Specifically, at lower holding temperature, no grains exceed 400 pixels in area, while at higher holding temperature, only a few grains are larger than 400 pixels. A similar pattern is observed in the perimeter distribution, though it shows a smoother decreasing trend compared to the area distribution.

Regarding grain length distribution, most grains are under 50 pixels in length at both isothermal holding temperatures, with only a few grains around 50 pixels. In contrast, the thickness distribution does not exhibit a clear trend for either temperature setting. However, the data suggests that grains are thinner at the lower holding temperature compared to the higher one, indicating finer grains at the lower holding temperature—a finding that aligns with experimental observations.

The average thickness of the grains is measured at 0.341 and 0.382 μm for the low and high holding temperatures, respectively. However, the experimental data shows an average grain thicknesses of 0.15 ± 0.05 and 0.26 ± 0.08 μm for holding temperatures of 400 and 450 °C, respectively. This points to a discrepancy in the simulated results for the lower holding temperature which could be due to the simulation resolution limit, although the high holding temperature results are closely aligned with the experimental findings.

3.4. 3D Microstructure Analysis

Utilizing 3D microstructure analysis, one can achieve accurate quantification of the volume fractions of various phases, as well as ascertain the morphology of these phases. As illustrated in **Figure 12**, the grains display both lath-like and platelike structures. In this study, the volume of each grain is calculated, which is derived from PF simulations. Given the irregular shapes of the grains, this opens up opportunities for exploring different shape factors to better estimate the grain's morphology. Although we attempted to use an ellipsoidal fit to characterize these shapes, the method proved ineffective due to the grain's irregular geometries.

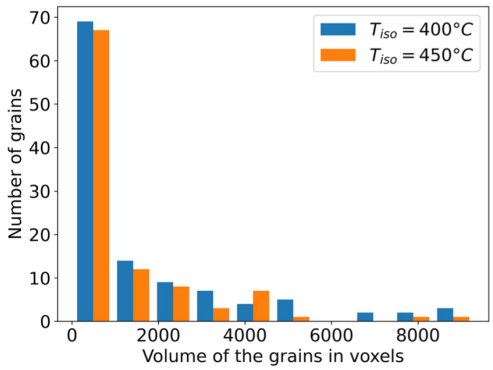

Figure 13. Distribution of volume of the grains in voxels for two isothermal holding temperatures.

The grain size distribution, in terms of the volume of the grains, is depicted in **Figure 13**. This distribution clearly shows that a lower holding temperature results in a higher number of very small grains (less than 2000 voxels). As the grain size surpasses 5000 voxels, the frequency of grains decreases significantly at higher holding temperature compared to low holding temperature, indicating a reduced number of grains in the specimens. This trend demonstrates a general decrease in grain size with lower holding temperature.

4. Conclusion

In this study, we successfully employed an automated workflow implementation to simulate low-carbon bainitic steels under different isothermal holding temperatures using the PF software library OpenPhase. We examined the effect of isothermal holding temperature on the microstructure morphology and

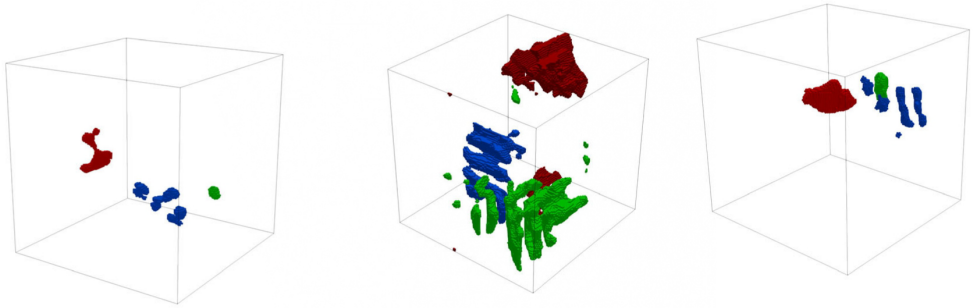

Figure 12. Different bainitic microstructures showing platelike morphology and complex morphology in 3D space.

ADVANCED SCIENCE NEWS
www.advancedsciencenews.com

ADVANCED ENGINEERING MATERIALS
www.aem-journal.com

conducted comparisons with experimental findings. Analysis of morphological features indicates that grains decrease in size at lower holding temperature compared to high holding temperature. This is also supported by the 3D grain size distribution. The key findings of this research can be summarized as follows. 1) Microstructural features like thickness of the BF are calculated from experiments and simulations for two different heat-treatment conditions. Average grain thickness at high temperatures from simulations and experiments is qualitatively aligned, whereas at low temperature, measurements from experiments and simulations show discrepancies. 2) The grain length distribution from the PF simulation results illustrates that microstructures with a low holding temperature exhibit finer grains, implying smaller grain sizes. Simultaneously, the thickness distribution plot demonstrates that grains are becoming thinner overall. 3) The grain area and perimeter distributions show a sharp decrease at low and high isothermal holding temperatures. And no grains have exceed 400 pixels in area at lower temperatures, with only a few larger grains at higher temperatures. 4) Most of the grains are under 50 pixels in length at both temperatures, with few reaching around 50 pixels. Grain thickness does not show a clear trend, but grains appear thinner at lower temperatures, indicating finer grains. 5) Further work is required to analyze 3D morphologies as they exhibit complex structures. And new shape factors should be employed to evaluate these structures further.

Acknowledgements

The authors acknowledge funding by the German Federal Ministry of Education and Research (BMBF)—project 13XP5118A (iBain).

Open Access funding enabled and organized by Projekt DEAL.

Conflict of Interest

The authors declare no conflict of interest.

Author Contributions

Dhanunjaya Nerella: Data curation: (lead); Formal analysis: (lead); Methodology: (equal); Software: (equal); Writing—original draft: (lead); **Muhammad Adil Ali**: Methodology: (supporting); Software: (supporting); Writing—original draft: (supporting); **Hesham Salama**: Formal analysis: (supporting); Methodology: (supporting); Software: (supporting); Writing—original draft: (supporting); **Oguz Gülbay**: Data curation: (equal); Formal analysis: (equal); Methodology: (supporting); Software: (supporting); Writing—original draft: (supporting); **Marc Ackermann**: Data curation: (equal); Formal analysis: (equal); Supervision: (equal); Writing—review and editing: (supporting); **Oleg Shchyglo**: Methodology: (equal); Project administration: (lead); Software: (supporting); Supervision: (equal); Writing—review and editing: (lead); **Ulrich Krupp**: Funding acquisition: (equal); Project administration: (equal); Supervision: (equal); Writing—review and editing: (supporting). **Ingo Steinbach**: Conceptualization: (lead); Funding acquisition: (lead); Project administration: (lead); Resources: (lead); Supervision: (equal); Writing—review and editing: (equal).

Data Availability Statement

The data that support the findings of this study are available from the corresponding author upon reasonable request.

Keywords

bainite, microstructure, morphological features, workflow

Received: April 15, 2024
Revised: August 26, 2024
Published online: September 19, 2024

[1] H. K. D. H. Bhadeshia, J. Christian, *Metall. Trans. A* **1990**, *21*, 767.
[2] L. Fielding, *Mater. Sci. Technol.* **2013**, *29*, 383.
[3] O. Gulbay, M. Ackermann, A. Gramlich, A. R. Durmaz, I. Steinbach, U. Krupp, *Steel Res. Int.* **2023**, *94*, 2300238.
[4] D. Iren, M. Ackermann, J. Gorfer, G. Pujar, S. Wesselmecking, U. Krupp, S. Bromuri, *Sci. Data* **2021**, *8*, 140.
[5] M. Ackermann, D. Iren, S. Wesselmecking, D. Shetty, U. Krupp, *Mater. Charact.* **2022**, *191*, 112091.
[6] X. Long, J. Kang, B. Lv, F. Zhang, *Mater. Des.* **2014**, *64*, 237.
[7] W. L. Costin, O. Lavigne, A. Kotousov, *Mater. Sci. Eng. A* **2016**, *663*, 193.
[8] Y. Jiang, M. A. Ali, I. Roslyakova, D. Bürger, G. Eggeler, I. Steinbach, *Modell. Simul. Mater. Sci. Eng.* **2023**, *31*, 035005.
[9] P. Steinmetz, Y. C. Yabansu, J. Hötzer, M. Jainta, B. Nestler, S. R. Kalidindi, *Acta Mater.* **2016**, *103*, 192.
[10] Y. C. Yabansu, P. Steinmetz, J. Hötzer, S. R. Kalidindi, B. Nestler, *Acta Mater.* **2017**, *124*, 182.
[11] H. S. Stein, J. M. Gregoire, *Chem. Sci.* **2019**, *10*, 9640.
[12] K. Mathew, J. H. Montoya, A. Faghaninia, S. Dwarakanath, M. Aykol, H. Tang, I.-h. Chu, T. Smidt, B. Bocklund, M. Horton, J. Dagdelen, B. Wood, Z.-K. Liu, J. Neaton, S. P. Ong, K. Persson, A. Jain, *Comput. Mater. Sci.* **2017**, *139*, 140.
[13] P. Nikolaev, D. Hooper, N. Perea-Lopez, M. Terrones, B. Maruyama, *ACS Nano* **2014**, *8*, 10214.
[14] T. Dimitrov, C. Kreisbeck, J. S. Becker, A. Aspuru-Guzik, S. K. Saikin, *ACS Appl. Mater. Interfaces* **2019**, *11*, 24825.
[15] C. R. Rêgo, J. Schaarschmidt, T. Schlöder, M. Penaloza-Amion, S. Bag, T. Neumann, T. Strunk, W. Wenzel, *Front. Mater.* **2022**, *9*, 877597.
[16] J. Janssen, S. Surendralal, Y. Lysogorskiy, M. Todorova, T. Hickel, R. Drautz, J. Neugebauer, *Comput. Mater. Sci.* **2019**, *163*, 24.
[17] G. Van Rossum, F. L. Drake, in *Python 3 Reference Manual*, CreateSpace, Scotts Valley, CA **2009**.
[18] OpenPhase, OpenPhase Software Library for Phase-Field Simulations, https://openphase.rub.de, (accessed: January **2024**).
[19] M. Tegeler, O. Shchyglo, R. D. Kamachali, A. Monas, I. Steinbach, G. Sutmann, *Comput. Phys. Commun.* **2017**, *215*, 173.
[20] I. Steinbach, M. Uddagiri, H. Salama, M. A. Ali, O. Shchyglo, *MRS Bull.* **2024**, *49*, 1.
[21] A. Clark, Pillow (Pil Fork) Documentation, https://buildmedia.readthedocs.org/media/pdf/pillow/latest/pillow.pdf, (accessed: January **2024**).
[22] G. Bradski, *Dr. Dobb's J.* (accessed: January **2024)**.
[23] M. Groeber, M. Uchic, D. Dimiduk, Y. Bhandari, S. Ghosh, *J. Comput.-Aided Mater. Des.* **2007**, *14*, 63.
[24] B. Sandvik, H. Nevalainen, *Met. Technol.* **1981**, *8*, 213.
[25] E. Kozeschnik, H. Bhadeshia, *Mater. Sci. Technol.* **2008**, *24*, 343.
[26] L. Chang, H. Bhadeshia, *Mater. Sci. Technol.* **1995**, *11*, 874.
[27] H. Bhadeshia, D. Edmonds, *Acta Metall.* **1980**, *28*, 1265.
[28] M. Peet, *Materials Algorithms Project Program Library*, **2007**.
[29] E. Swallow, H. Bhadeshia, *Mater. Sci. Technol.* **1996**, *12*, 121.
[30] H. Bhadeshia, D. Edmonds, *Met. Sci.* **1983**, *17*, 411.
[31] S. Zajac, V. Schwinn, K. Tacke, in *Materials Science Forum*, Vol. *500*, Trans Tech Publ., Stafa-Zurich, Switzerland **2005**, pp. 387–394.
[32] F. Caballero, H. Roelofs, S. Hasler, C. Capdevila, J. Chao, J. Cornide, C. Garcia-Mateo, *Mater. Sci. Technol.* **2012**, *28*, 95.

